No. 334
April 1997

FULLY NONLINEAR SHIP-WAVE COMPUTATIONS USING A MULTIPOLE ACCELERATED, DESINGULARIZED METHOD

by

Stephen M. Scorpio

Department of Naval Architecture
and Marine Engineering
College of Engineering
The University of Michigan
Ann Arbor, MI 48109-2145

FULLY NONLINEAR SHIP-WAVE COMPUTATIONS USING A MULTIPOLE ACCELERATED, DESINGULARIZED METHOD

by
Stephen Michael Scorpio

A dissertation submitted in partial fulfillment
of the requirements for the degree of
Doctor of Philosophy
(Naval Architecture and Marine Engineering)
in The University of Michigan
1997

Doctoral Committee:

Professor Robert F. Beck, Chairperson
Doctor F. Thomas Korsmeyer
Associate Professor William W. Schultz
Professor Armin W. Troesch

ABSTRACT

FULLY NONLINEAR SHIP-WAVE COMPUTATIONS USING A MULTIPOLE ACCELERATED, DESINGULARIZED METHOD

by
Stephen Michael Scorpio

Chairperson: Robert F. Beck

The inviscid ship-wave problem with fully nonlinear boundary conditions is solved using a multipole accelerated, Desingularized Euler-Lagrange Time-domain Approach or DELTA method. The desingularization greatly simplifies the evaluation of the boundary integrals while the multipole acceleration reduces the computational effort and storage from $O(N^2)$ down to $O(N)$. This allows problems with very large numbers of unknowns to be analyzed efficiently on modern workstations. These solution methods are applied to a variety of two- and three-dimensional problems including two-dimensional transom stern flow, shallow water waves incident on a vertical cylinder, wave pattern and wave resistance of a mathematical hull form, and exciting forces on the mathematical hull form in sinusoidal incident waves.

To my parents and to Diana

ACKNOWLEDGEMENTS

I wish to thank all those who helped me in completing this thesis. Special thanks go to Professor Beck whose insight and experience helped me to avoid many pitfalls along the way. Professor Beck is a good friend as well as an excellent advisor. I'm grateful to Dr. Korsmeyer for his helpful discussions, comments and suggestions. Thanks also go to Professors Troesch and Schultz for serving on my dissertation committee.

I owe my gratitude to my fiancée, Diana, whose love and support over the past four years has helped pull me through. Thanks to my brother, Angelo, and sisters, Lisa and Caroline, who have always offered their love, interest and support. But most of all, I am deeply indebted to my parents. They have always supported my endeavors, both academic and personal, throughout my life. Whenever I had need, I could always turn to my parents for guidance, emotional support, comfort, encouragement, sympathy, kindness, and love. This success for me is the product of their hard work in raising me, thank you.

This research was funded by the Office of Naval Research AASERT Grant N-00014-93-1-0629 and the University of Michigan/Sea Grant/Industry Consortium on Offshore Engineering. Computations were made in part using a Cray Grant, University Research and Development Program at the San Diego Supercomputer Center.

TABLE OF CONTENTS

CHAPTER

LIST OF FIGURES

Figure

LIST OF TABLES

LIST OF APPENDICES

Appendix

CHAPTER I

INTRODUCTION

The physical processes that describe the hydrodynamic characteristics of a floating body are extremely complex. In addition to understanding the gross fluid motion and corresponding interaction with the body, one must also understand and predict turbulence, spray, breaking waves, bubbly flows, acoustics, etc. These processes tend to be categorized and studied separately, yet they all interact with each other and contribute to the overall description of the body-wave problem. The only way to get the "right answer" is to make full scale measurements which, itself, is not a trivial task. Fortunately, many useful engineering results can be obtained through experimentation on scale models and through calculations based on simplified theories. This thesis focuses on finding efficient solutions for one of these simplified theories.

The choice of mathematical model is of paramount importance. A model must have enough simplification to render its solution tractable and enough physics to produce useful results. In recent years, the advent of numerical methods and computer science has made the solution of increasingly complex models tractable. One model that accurately describes the problem is the Navier-Stokes equations for the fluid motion coupled with the equations of rigid body dynamics for the body motion. Disparity in time and length scales due to the presence of turbulence suggests using the unsteady Reynolds Averaged Navier-Stokes (RANS) equations or Large-Eddy Simulation (LES) to model the fluid motion. These models show a lot of promise for predicting local flow characteristics near the body, a result that is very important for designing and evaluating appendages such as propellers, skegs, rudders, and bulbous bows. RANS and LES models are typically solved by discretizing a volume of fluid where flow characteristics are desired. To accurately predict the forces and subsequent motions of a floating body, a large volume of fluid must be accurately discretized, making the solution of the RANS and LES models computationally intensive. Typical marine hydrodynamics problems involve Reynolds numbers on the order of 10^9 so that viscous effects such as turbulence are confined to a thin boundary layer near the body and a viscous wake region trailing the body. The rest of the flow field can be considered irrotational. In fact, the major forces that effect the motion of a body in waves are generated by the irrotational part of the flow field. By assuming the fluid is inviscid, the flow can be modeled using potential theory and the effort involved in describing the motion of a large volume of fluid is drastically reduced. Although the inviscid model discards some very important physics in the near field flow, it does provide accurate and efficient predictions for the global loads and corresponding motions of a floating body. For these reasons, the inviscid flow model is adopted in this thesis and methods are studied to improve the efficiency of the numerical solution method.

There are two major computational difficulties associated with the potential problem for inviscid flow. One is that the free surface boundary conditions are nonlinear and the other is that the free surface boundary is unknown *a priori*. Historically, these problems have been circumvented by solving a problem where the free surface boundary conditions are expanded about a known configuration and then linearized. This problem has been solved using a variety of two- and three-dimensional methods. Some of the common problem formulations using linearized free surface boundary conditions are the so called slender-body theories in two dimensions and the Neumann-Kelvin, body exact, and Dawson methods in three dimensions.

Slender-body theories involve some assumptions about the body geometry that simplify the problem. One of the earliest applications of this idea was Michell's integral [30] for computing wave resistance developed in 1898. He assumed the beam was much smaller than the length while the draft was on the same order as the length. This idea was extended to the ship motions problem by Newman [35] in 1959. Assuming the beam and draft are small relative to the length leads to several different theories. One of these is the well known strip theory of ship motions in waves pioneered by Korvin-Kroukovsky [7] in 1955 who developed a theory based largely on heuristic and physical arguments. The theory was improved and formalized mathematically in the works of Gerritsma and Beukelman [20], Ogilvie and Tuck [37], Salvesen, Tuck, and Faltinsen [40] and others. By the late 1970's the slender-body theories were considered mature technologies and had been applied successfully to many marine hydrodynamics problems. Computations based on slender-body approximations have proven to be very robust. This desirable property has lured naval architects into applying these methods to ship forms that are not slender, producing inaccurate and often misleading results. To analyze general bodies, three-dimensional methods were brought to bear on the problem.

In the Neumann-Kelvin method, no assumptions are made about the body geometry. The free surface boundary conditions are linearized about the free stream at the mean water level and the body boundary condition about the mean body position. This linearization allows the use of Green function techniques that automatically meet the free surface boundary conditions and conditions at infinity. Leaving only the body boundary conditions to be satisfied by discretizing the body surface. The so called "panel methods" can be solved in either the frequency or time domain. The frequency and time domain solutions are Fourier transforms of each other and the specifics of the problem determine which formulation is appropriate.

The body-exact linearization is similar to the Neumann-Kelvin method except the body boundary condition is satisfied on the instantaneous body wetted surface rather than linearizing about the mean body position. This results in a time-varying linear system making the frequency and time-domain solutions no longer simply related. By including the exact body boundary condition, the hydrodynamic forces on a body undergoing sinusoidal excitation are no longer sinusoidal but may include mean shifts and higher-order terms. Typically this formulation is solved in the time domain. The computation of memory effects by evaluating convolution integrals significantly reduces the efficiency of this method for long time simulations. Examples of linear frequency and time-domain calculations using the Neumann-Kelvin or body-exact linearizations are in Inglis and Price [19], Wu and Eatock Taylor [47], Newman [35], Korsmeyer *et al.* [24], King *et al.* [23], and Beck and Magee [4].

In Dawson's method, the potential is decomposed into: $\Phi = \phi_D + \phi$ where ϕ_D is the double body potential. The free surface boundary conditions are then linearized about the double body flow. Since the double body flow and hence the free surface boundary conditions are geometry dependent, a free surface Green function approach is no longer possible. In this case, the free surface and body boundary conditions are typically satisfied by distributions of Rankine sources over the free surface and body. Examples using Dawson's linearization are in Bertram [6], Nakos and Sclavounos [33], Nakos *et al.* [32], and Kring and Sclavounos [26].

Results from these linearized calculations have produced excellent agreement with experiments for some problems but very poor agreement in others. Inconsistency in the results, believed to be caused by the exclusion of nonlinearities, led researchers to include higher-order terms in the boundary conditions. The higher-order theories are significantly more complex due to the presence of higher-order derivatives in the free surface boundary conditions. Higher-order theories produce reasonable results for some problems but the methods are difficult to apply to a wide variety of problems.

The shortcomings of perturbation expansion methods have led to the next logical step of solving the fully nonlinear problem. The use of time dependent, fully nonlinear free surface boundary conditions in numerical computations was introduced by Longuet-Higgins and Cokelet [29]. They used a mixed Euler-Lagrange method for the solution of two-dimensional waves near breaking. Part one of the Euler-Lagrange method is the Lagrange phase where individual particles on the free surface are tracked by integrating the nonlinear free surface boundary conditions with respect to time. Each step in the temporal evolution of the Lagrange phase requires the execution of part two, the Euler phase, where a linear boundary value problem is solved to obtain the fluid velocities needed to integrate the free surface boundary conditions. This method is very popular for fully nonlinear free surface problems and has been successfully applied by many researchers including Faltinsen [16], Vinje and Brevig [45], Baker *et al.* [1], Grosenbaugh and Yeung [18], and Cointe *et al.* [14] for two-dimensional problems and Lin *et al.* [28], Dommermuth and Yue

[15], Kang and Gong [22], Zhou and Gu [49], Cao [8], Cao *et al.* ([10], [11], [9]), Lee [27], Beck *et al.* ([2], [3]), Beck and Scorpio [5], Scorpio and Beck [41], and Scorpio *et al.* [42] for three-dimensional problems.

The key to the success of the Euler-Lagrange method is a stable and accurate time stepping technique. Longuet-Higgins and Cokelet [29] used an Adams-Bashforth-Moulton predictor corrector integration technique but encountered a sawtooth instability on the free surface that they suppressed by applying a smoothing function. They gave no explanation for the cause of the instability. Dommermuth and Yue [15] used a fourth-order Runge Kutta scheme to integrate the boundary conditions for nonlinear axisymmetric problems. They also encountered free surface instabilities that they believed to be caused in part by the "concentration of Lagrangian points in regions of high flow gradients." Rather than using an arbitrary smoothing function, they eliminated the instabilities by regridding the free surface after each time step. Park and Troesch [38] investigated the stability of time marching schemes for a variety of two- and three-dimensional problems. They concluded that the stability of the solution depends on the geometry of the problem, the application of far-field boundary conditions and the time integration method. They also noted that three-dimensional problems seemed to be more stable than two-dimensional problems.

Although the time-stepping scheme is very important for accurate and stable solutions, it is the solution of the linear mixed boundary value problem in the Euler phase that consumes most of the computational effort. Difficulties arising during this part of the computation include implementation of far-field radiation boundary conditions and treatment of the body/free surface intersection line. Many methods have been proposed for solving these boundary value problems. These methods that discretize the volume of fluid include finite difference, finite volume, and finite element techniques. The most common technique is to transform the differential equation in the fluid volume to a boundary integral equation on the fluid boundary using Green's theorem. This has a decided advantage over the volume techniques in that only the fluid boundary need be discretized. The disadvantage is that the resulting matrices are full as opposed to the sparse linear systems resulting from the volume methods.

In the boundary integral method used here, Green's theorem is applied to derive the indirect integral formulation of the problem. The integrals are discretized by distributing fundamental singularities over a surface referred to as the "integration surface". Boundary conditions are satisfied at discrete collocation points located on a "control surface". In conventional formulations, the integration and control surfaces coincide and define the boundary of the fluid domain. This results in integrals with singular kernels requiring special treatment by considering only their principal part. By moving the integration surface slightly off the control surface, the kernels are "desingularized." This technique, probably first introduced in panel methods by Webster [46], has several computational advantages over the singular formulation. Because of the nonsingular kernels, no special treatment is needed when evaluating the integrals so that simple numerical quadratures may be used. This removes the necessity of evaluating transcendental functions appearing in the singular formulation. In fact, the desingularized formulation becomes even simpler by replacing the singularity distribution with isolated singularities. These can be sources or higher-order singularities such as dipoles. When desingularized isolated singularities are used, the necessity to evaluate surface integrals is eliminated and is replaced by simple summations. This leads to fast, stable free surface computations. We denote the resulting method as the Desingularized Euler-Lagrange Time-domain Approach or DELTA method. Examples of desingularized, fully nonlinear free surface computations are given in Cao *et al.* [11], Beck *et al.* [2], Beck *et al.* [3], Beck and Scorpio [5], Scorpio and Beck [41], and Scorpio *et al.* [42]

The numerical approximation of the integral equations results in a linear system of equations. For the free surface problems considered here, the linear system consists of a matrix of coefficients (representing the influence of sources on collocation points in the desingularized method) multiplied by a vector of unknown source strengths. The matrix/vector product must equal the known boundary conditions. Solution of this linear system by an iterative method will require order N^2 ($O(N^2)$) work and storage for the tasks of filling the matrix once and applying the matrix to a vector at each iteration. With large numbers of unknowns ($O(10^4)$), as is required to discretize three-dimensional domains , solutions by iterative solvers are too expensive for practical computations on workstations. However, the efficiency of an iterative solver can be improved significantly when accelerated by a multipole algorithm.

Multipole expansions result when Laplace's equation is solved in spherical coordinates using the method of separation of variables. The multipole algorithm approximates the influence of groups of far-field sources with expansions, thereby replacing a large portion of the influence coefficient matrix. In a multipole accelerated iterative solver, the matrix/vector product required at each iteration (normally $O(N^2)$ cost) is replaced by a multipole approximation ($O(N)$ cost). Greengard [17] presents an efficient algorithm for the application of multipole expansions to potential problems. Nabors *et al.* [31] present a slightly different approach developed for electrostatics problems, and Korsmeyer *et al.* [25] extends that approach to Laplace problems in general, particularly the Green's theorem formulation of free surface problems.

The linear systems that result from the DELTA method are often poorly conditioned which can lead to convergence problems for iterative solvers. This problem can be avoided with a preconditioner that approximates the matrix inverse. Nabors *et al.* [31] suggest an approximation for the matrix inverse can be computed by solving overlapping subproblems. Each subproblem represents the influence of nearby source points on nearby collocation points. The inverse of the sub-matrices are computed and compiled together; thus forming the approximate inverse. The preconditioner is then applied within the iterative solution to accelerate convergence.

In this thesis, the efficiency of the DELTA method is improved by incorporating a preconditioned multipole acceleration algorithm. A new technique is introduced for the inclusion of fully nonlinear incident waves for head seas problems. The resulting code is applied to the problems of incident waves diffracted by a vertical cylinder, calm water steady forward speed resistance calculations, steady forward speed head seas calculations, and flow behind a two-dimensional transom stern.

CHAPTER II

PROBLEM FORMULATION AND SOLUTION TECHNIQUES

Consider the problem of a vessel floating on a free surface. Assuming inviscid, incompressible flow the fluid motion can be described using potential theory. By defining the fluid velocity by a scalar potential, $\vec{u}(\vec{x},t) = \nabla\Phi(\vec{x},t)$, the continuity equation reduces to Laplace's equation and the momentum equations reduce to Bernoulli's equation. The formulation shown here is for a three-dimensional problem. The formulation for the two-dimensional problem is similar.

2.1 Initial-Boundary Value Problem

2.1.1 Governing equations

For a real ship in a seaway, the fluid domain is effectively unbounded relative to the scale of the ship. For computational purposes, the fluid domain must be truncated. Figure 2.1 shows the geometry and coordinate system used in the computational domain. V represents the fluid volume bounded above by the free surface S_f and body surface S_h, below by the bottom surface S_b, and a truncation surface S_t. The coordinate system is right-handed with z pointing up, x out the stern of the ship, and y to starboard.

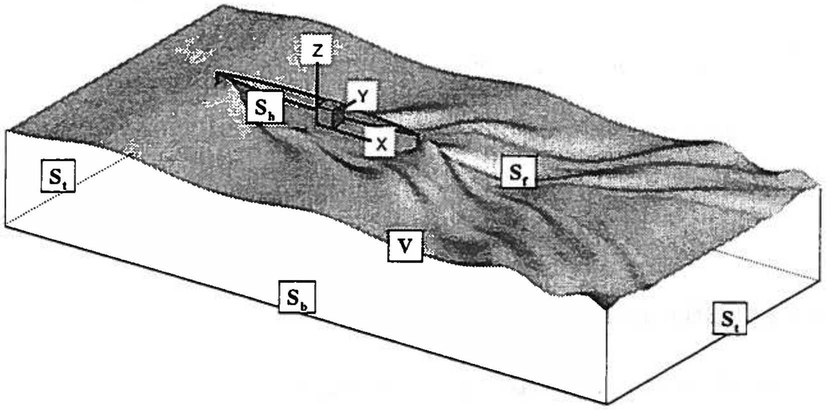

Figure 2.1: Problem setup

Everywhere in the fluid volume the velocity potential must satisfy continuity which reduces to Laplace's equation for potential flow,

$$\nabla^2\Phi = 0 \qquad \vec{x} \in V \tag{2.1}$$

and the momentum equations which reduce to Bernoulli's equation,

$$\frac{p}{\rho} + \frac{\partial\Phi}{\partial t} + gz + \frac{1}{2}|\nabla\Phi|^2 = C(t) \qquad \vec{x} \in V. \tag{2.2}$$

With this formulation, the potential Φ and pressure p are uncoupled. Typically a solution for Φ is found by satisfying (2.1) along with appropriate initial-boundary conditions. Then p is easily computed using (2.2).

2.1.2 Initial and boundary conditions

To set up a well posed initial-boundary value problem, initial conditions and boundary conditions on all enclosing surfaces are required. For forward speed problems the velocity potential is decomposed into the free stream part and the perturbation part,

$$\Phi(\vec{x},t) = \vec{U}(t)\cdot\vec{x} + \phi(\vec{x},t). \tag{2.3}$$

Here $\vec{U}(t)\cdot\vec{x}$ is the potential for the free stream velocity and $\phi(\vec{x},t)$ is the perturbation potential. The problem for ϕ is solved in a ship-fixed coordinate system moving with speed $-\vec{U}$.

Initial conditions

The problem is started from rest so that,

$$\phi(\vec{x},t) = 0 \qquad \vec{x}\in V, \;\; t=0$$

and

$$\eta(x,y,t) = \eta_o(x,y) \qquad (x,y)\in S_f, \;\; t=0 \tag{2.4}$$

where $\eta(x,y,t)$ is the free surface elevation and $\eta_o(x,y)$ is the known initial free surface elevation.

Boundary conditions

On solid boundary surfaces such as the body (S_h), bottom (S_b), and perhaps the truncation surface (S_t) if it is defined as a solid wall, a kinematic condition requiring no flow normal to the boundary is imposed. Since the flow is assumed inviscid, there is no condition on flow tangential to the boundary. The boundary condition for the body surface is,

$$\vec{n}\cdot\nabla\phi = -\vec{n}\cdot\vec{U} + \vec{n}\cdot\vec{V_h} \qquad \vec{x}\in S_h \tag{2.5}$$

where $\vec{V_h}$ is the local velocity of points on the body including rotational effects. On the bottom surface,

$$\vec{n}\cdot\nabla\phi = 0 \qquad \vec{x}\in S_b. \tag{2.6}$$

A proper condition on the truncation boundary that is valid for a wide variety of problems has yet to be found. Ideally, this boundary condition would allow waves to radiate out of the problem domain with no reflection. Because of nonlinearities in the free surface boundary conditions, this radiation condition is extremely difficult if not impossible to find. Several researchers have proposed approximate radiation boundary conditions based on results from linear theories. These conditions usually require some prior knowledge of the free surface waves such as their direction and frequency, quantities that may be difficult to define in a fully nonlinear problem. Examples of approximate radiation boundary conditions for nonlinear free surface flows are in Yang and Ertekin [48]. A second alternative is to absorb all the wave energy before it can reach the truncation boundary. This technique requires a much larger computational domain so that energy can be gradually absorbed as the waves propagate towards the truncation boundary. Examples of the successful application of this technique are in Baker et al. [1] and Cointe [13]. The third alternative is to reflect all of the wave energy. In this case, the condition on the truncation boundary is,

$$\vec{n} \cdot \nabla \phi = 0 \qquad \vec{x} \in S_t. \tag{2.7}$$

Of course, this has the undesireable effect of sending wave energy back to the ship limiting the simulation time.

Since the free surface elevations are undefined *a priori,* two boundary conditions are required. The kinematic condition requires that a point on the free surface remain on the free surface,

$$\frac{\partial \eta}{\partial t} + \left(\vec{U} + \nabla \phi\right) \cdot \nabla \eta - \frac{\partial \phi}{\partial z} = 0 \qquad \vec{x} \in S_f. \tag{2.8}$$

The dynamic boundary condition requires the free surface pressure equal the ambient pressure, p_a. In the translating coordinate system, the unsteady Bernoulli equation is,

$$\frac{p_a}{\rho} = -\frac{\partial \Phi}{\partial t} - \frac{\partial \vec{U}}{\partial t} \cdot \vec{x} - g\eta - \frac{1}{2}|\nabla \Phi|^2 \qquad \vec{x} \in S_f. \tag{2.9}$$

Making the substitution, $\Phi = \vec{U} \cdot \vec{x} + \phi$ results in the dynamic free surface boundary condition for the perturbation potential,

$$\frac{p_a}{\rho} = -\frac{\partial \phi}{\partial t} - g\eta - \frac{1}{2}|\nabla \phi|^2 - \vec{U} \cdot \nabla \phi \qquad \vec{x} \in S_f. \tag{2.10}$$

The problem outlined above has a linear field equation with nonlinear boundary conditions. Exact solutions are known for extremely simplified problems only. To find solutions to more general, physically interesting problems we resort to numerical solution methods. The numerical method used in this thesis is outlined in the following section.

2.2 Euler-Lagrange time stepping procedure

The method for finding solutions to the nonlinear initial-boundary value problem is the so called Euler-Lagrange time stepping technique introduced by Longuet-Higgins and Cokelet [29]. The solution is formed by repeating the following two steps,

1. A linear mixed boundary value problem is solved for the perturbation potential at a fixed instant in time.

2. The nonlinear free surface boundary conditions can then be stepped forward in time.

The boundary value problem at each time step is,

$$\nabla^2 \phi = 0 \qquad \vec{x} \in V$$

$$\begin{aligned} \phi = \phi_o \qquad & \vec{x} \in S_f \\ \vec{n} \cdot \nabla\phi = -\vec{n} \cdot \vec{U} + \vec{n} \cdot \vec{V_h} \qquad & \vec{x} \in S_h \\ \vec{n} \cdot \nabla\phi = 0 \qquad & \vec{x} \in S_b \end{aligned} \tag{2.11}$$

plus an appropriate truncation boundary condition. Here, ϕ_o is the known potential on the free surface at a given instant of time. With the solution to this boundary value problem the flow is known at the current instant of time. Details of the solution method for (2.11) are given in the next section. The free surface boundary conditions are then written in their Lagrangian form and stepped forward in time,

$$\frac{D\vec{x}}{Dt} = \vec{U} + \nabla\phi \tag{2.12}$$

$$\frac{D\phi}{Dt} = -\frac{p_a}{\rho} - g\eta + \frac{1}{2}|\nabla\phi|^2 \tag{2.13}$$

where $\frac{D}{Dt} = \frac{\partial}{\partial t} + \nabla\Phi \cdot \nabla$ is the material derivative. Allowing points on the free surface to move with the fluid velocity may cause numerical problems such as the piling up of nodes at stagnation points. To avoid these problems, Beck *et al.* [3] used a special form of the free surface boundary conditions that allows the horizontal plane motions to be prescribed,

$$\frac{\delta\eta}{\delta t} = \frac{\partial\phi}{\partial z} - (\nabla\phi - \vec{v}) \cdot \nabla\eta - \vec{U} \cdot \nabla\eta \tag{2.14}$$

$$\frac{\delta\phi}{\delta t} = -\frac{p_a}{\rho} - g\eta - \frac{1}{2}|\nabla\phi|^2 + \vec{v} \cdot \nabla\phi - \vec{U} \cdot \nabla\phi \tag{2.15}$$

where $\frac{\delta}{\delta t} = \frac{\partial}{\partial t} + \vec{v} \cdot \nabla$. The velocity of free surface nodes is, $\vec{v} = \left(u, v, \frac{\delta\eta}{\delta t}\right)$ where u and v are the prescribed horizontal plane velocities.

The choice of time integration technique is crucial for obtaining accurate and stable solutions. The fourth-order Runge Kutta scheme used here typically produces excellent results given a wise choice of time step size. Although the choice and careful implementation of a time integration technique is important, it is the solution of the linear mixed boundary value problem (2.11) that uses most of the computational effort and storage. For this reason, most of the research is concentrated on finding efficient solutions to this problem.

The pressure on the body can be computed at each time step using a form of Bernoulli's equation that accounts for the body motion,

$$\frac{p}{\rho} = -\frac{d\phi}{dt} - gz - \left(\frac{1}{2}\nabla\phi - \vec{V}_h\right) \cdot \nabla\phi \tag{2.16}$$
$$\text{where} \quad \frac{d\phi}{dt} = \frac{\partial\phi}{\partial t} + \vec{V}_h \cdot \nabla\phi$$

Forces and moments on the body can be computed by integrating pressure over the body surface,

$$\vec{F} = \iint_{S_h} -p\vec{n}_h ds \tag{2.17}$$
$$\vec{M} = \iint_{S_h} -p(\vec{r} \times \vec{n}_h) ds. \tag{2.18}$$

2.3 Linear mixed boundary value problem

The solution of the linear mixed boundary value problem (2.11) required at each time step in the Euler-Lagrange procedure requires most of the computational effort and storage. Details of methods to solve this problem efficiently and accurately follow.

2.3.1 Desingularized boundary integral method

A common technique for solving Laplace's equation is to use Green's theorem to reduce the order of the problem by one and solve the resulting integral equations. Rather than a direct application of Green's theorem we use an indirect approach (sometimes called the source formulation) where the potential in the fluid volume is defined by,

$$\phi(\vec{x}) = \iint_{\Omega} \sigma(\vec{\xi})G(\vec{x};\vec{\xi})d\Omega. \tag{2.19}$$

Ω is the integration surface on which the points $\vec{\xi} = (\xi, \eta, \zeta)$ reside and $\vec{x} = (x, y, z)$ is any point in the fluid domain. $G(\vec{x};\vec{\xi})$ is the Green's function that satisfies the Laplace equation and possibly some of the boundary conditions. $\sigma(\vec{\xi})$ is the unknown strength of G, specified by satisfying boundary conditions. The Rankine source Green's function is used herein,

$$G(\vec{x};\vec{\xi}) = \frac{1}{|\vec{x} - \vec{\xi}|} = \frac{1}{\sqrt{(x-\xi)^2 + (y-\eta)^2 + (z-\zeta)^2}} \tag{2.20}$$

which has the following properties,

$$\begin{gathered} \nabla^2 G = \delta(\vec{x} - \vec{\xi}) \\ \nabla G \to 0 \quad \text{as} \quad \vec{x} \to \infty \end{gathered} \tag{2.21}$$

where $\delta(\vec{x} - \vec{\xi})$ is the Dirac delta function. Since G satisfies none of the boundary conditions except infinite water depth ($\nabla G \to 0$ as $z \to -\infty$) the strength σ must be solved so that (2.19) satisfies all of the boundary conditions. Applying the boundary conditions outlined in (2.11), the integral equations for the unknown strength σ become,

$$\iint_{\Omega} \sigma G d\Omega = \phi_o \qquad \vec{x} \in S_f \tag{2.22}$$

$$\iint_{\Omega} \sigma \vec{n} \cdot \nabla_{\vec{x}} G d\Omega = \vec{n} \cdot \vec{V}_h \qquad \vec{x} \in S_h \tag{2.23}$$

$$\iint_{\Omega} \sigma \vec{n} \cdot \nabla_{\vec{x}} G d\Omega = 0 \qquad \vec{x} \in S_b \tag{2.24}$$

plus an appropriate integral expression for the truncation boundary. The boundary conditions are satisfied at points $\vec{x}$ located on the fluid boundary or *control surface.*

The integrals are evaluated by integrating over Ω, the *integration surface*, for each point on the control surface. Typically the integration and control surfaces coincide resulting in singular kernels when $\vec{x} = \vec{\xi}$. The singularities can be avoided by computing only the principal part of the integrals. This leads to labor intensive integrations involving transcendental functions. In the desingularized method, the integration surface is moved slightly off the control surface so that $\vec{x}$ never equals $\vec{\xi}$ eliminating singular points. Specifically, the integration surface is moved slightly above the free surface, inside the body surface and below the bottom. In general one would desingularize by moving the integration surface slightly outside of the fluid domain. Desingularization greatly simplifies the evaluation of the integral equations. By using isolated Rankine sources, the integral evaluations reduce to simple summations,

$$\begin{aligned} \sum_{j=1}^{N} \frac{\sigma_j}{|\vec{x}_i - \vec{\xi}_j|} &= \phi_{o_i} & \vec{x}_i \in S_f \\ \sum_{j=1}^{N} \sigma_j \vec{n}_i \cdot \nabla_{\vec{x}_i} \frac{1}{|\vec{x}_i - \vec{\xi}_j|} &= \vec{n}_i \cdot \vec{V}_h & \vec{x}_i \in S_h \\ \sum_{j=1}^{N} \sigma_j \vec{n}_i \cdot \nabla_{\vec{x}_i} \frac{1}{|\vec{x}_i - \vec{\xi}_j|} &= 0 & \vec{x}_i \in S_b \end{aligned} \tag{2.25}$$

where $\vec{x}_i = (x_i, y_i, z_i)$, $\vec{n}_i = (nx_i, ny_i, nz_i)$ is the unit normal pointing out of the fluid, N is the total number of unknown source strengths σ_j. When the above summations are applied at N collocation points $(\vec{x}_i)$ an $N \times N$ linear system results,

$$A_{ij}\sigma_j = b_i \tag{2.26}$$

where the influence matrix $A_{ij} = G_{ij} = 1/(|\vec{x}_i - \vec{\xi}_j|)$ for collocation points on the free surface and $A_{ij} = \vec{n}_i \cdot \nabla_{\vec{x}_i} G_{ij}$ for collocation points on solid boundaries. σ_j is the vector of unknown source strengths. b_i is the vector of boundary conditions, $b_i = \phi_{o_i}$ on the free surface, $b_i = \vec{n}_i \cdot \vec{V}_h$ on the body surface and $b_i = 0$ on the bottom. Details on the accuracy and convergence of solving the desingularized problem are given in Cao *et al.* [11]. Solving (2.26) using LU decomposition requires $O(N^2)$ storage and $O(N^3)$ work. An iterative solution requires $O(N^2)$ work and storage but convergence may be a problem if the condition number of A_{ij} is too large. As N becomes large, work and storage requirements quickly become excessive. The following sections introduce some efficient techniques for finding the solution to (2.26).

2.3.2 Domain decomposition

For two-dimensional problems (2.26) is solved using LU decomposition while for three-dimensional problems the iterative solver GMRES (see [39]) is used. When varying grid spacings are used on different parts of the domain boundary, the influence matrix A can be ill conditioned. This can cause convergence problems for the iterative solver. If the system becomes too ill conditioned, GMRES may not be able to converge to an acceptable tolerance. This problem can be avoided by decomposing the problem boundary into separate domains. Six domains can be identified that have relatively even grid spacing: 1) The free surface, 2) the body surface, 3) the bottom surface, 4) the upstream truncation boundary, 5) the downstream truncation boundary, and 6) the parallel truncation boundary. For simplicity in illustrating the domain decomposition, suppose there are only two domains (1 and 2) in the problem, then (2.26) can be written as,

$$\begin{pmatrix} A^{(11)} & A^{(12)} \\ A^{(21)} & A^{(22)} \end{pmatrix} \begin{pmatrix} \sigma^{(1)} \\ \sigma^{(2)} \end{pmatrix} = \begin{pmatrix} b^{(1)} \\ b^{(2)} \end{pmatrix} \tag{2.27}$$

The linear system is decomposed so that $\sigma^{(1)}$ and $\sigma^{(2)}$ are solved separately using an iterative procedure. The decomposed linear systems are,

$$A^{(11)}\sigma^{(1)} = b^{(1)} - A^{(12)}\sigma^{(2)} \tag{2.28}$$

and

$$A^{(22)}\sigma^{(2)} = b^{(2)} - A^{(21)}\sigma^{(1)}. \tag{2.29}$$

(2.28) is solved for $\sigma^{(1)}$ with $\sigma^{(2)}$ known (or guessed). Then $\sigma^{(1)}$ is substituted into (2.29) to determine $\sigma^{(2)}$. The procedure is repeated until both (2.28) and (2.29) are satisfied to within a prescribed tolerance. This solution method may be faster than solving (2.26) directly as long as the number iterations is not too large.

2.3.3 Multipole acceleration

Writing the Laplace equation in spherical coordinates yields,

$$\frac{1}{r^2}\frac{\partial}{\partial r}\left(r^2\frac{\partial\Phi}{\partial r}\right) + \frac{1}{r^2\sin\theta}\frac{\partial}{\partial\theta}\left(\sin\theta\frac{\partial\Phi}{\partial\theta}\right) + \frac{1}{r^2\sin^2\theta}\frac{\partial^2\Phi}{\partial\phi^2} = 0. \tag{2.30}$$

The spherical coordinates relative to the Cartesian system are shown in figure 2.2.

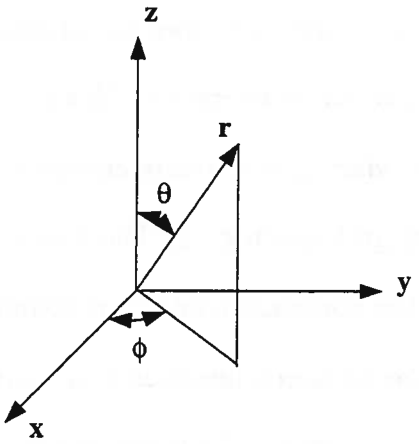

Figure 2.2: Spherical coordinate system

The solution of this equation by separation of variables results in a series of spherical harmonic terms,

$$\Phi = \sum_{n=0}^{\infty}\sum_{m=-n}^{n}\left(L_n^m r^n + \frac{M_n^m}{r^{n+1}}\right)Y_n^m(\theta,\phi). \tag{2.31}$$

M_n^m and L_n^m are the moments of the expansion and $Y_n^m(\theta,\phi)$ are the spherical harmonics of order m and degree n. The functions $Y_n^m(\theta,\phi)$ are related to the Legendre polynomials by the following relation,

$$Y_n^m(\theta, \phi) = \sqrt{\frac{(n-|m|)!}{(n+|m|)!}} \cdot P_n^{|m|}(\cos\theta) e^{im\phi} \tag{2.32}$$

where $P_n^{|m|}(cos\theta)$ are the Legendre polynomials. Using the series solution to the Laplace equation, the far-field potential due to a collection of near-field sources can be expressed in a multipole expansion. Suppose there are k sources with coordinates $(\rho_i, \alpha_i, \beta_i)$ $i = 1, \cdots, k$ and strengths σ_i. Consider a sphere of radius a containing the k sources as shown in figure 2.3. Let the center of a multipole expansion be defined as the center of this sphere. We can then express the potential due to the k near-field sources at any far-field point, $P(r, \theta, \phi)$, outside of the sphere,

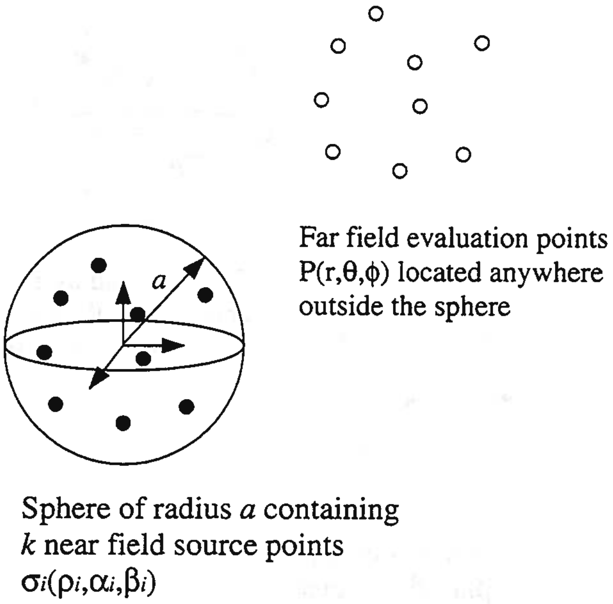

Figure 2.3: Multipole expansion

$$\Phi(P) = \sum_{n=0}^{\infty} \sum_{m=-n}^{n} \frac{M_n^m}{r^{n+1}} Y_n^m(\theta, \phi) \tag{2.33}$$

where the coefficients of the expansion are given by,

$$M_n^m = \sum_{i=1}^{k} \sigma_i \rho_i^n Y_n^{-m}(\alpha_i, \beta_i). \tag{2.34}$$

Truncating the series at p terms produces the following error bound,

$$\left|\Phi(P) - \sum_{n=0}^{p}\sum_{m=-n}^{n} \frac{M_n^m}{r^{n+1}} \cdot Y_n^m(\theta,\phi)\right| \le \frac{\sum_{i=1}^{k} |\sigma_i|}{r-a}\left(\frac{a}{r}\right)^{p+1} \tag{2.35}$$

Likewise, the near-field potential due to a collection of far-field sources can be expressed in a local expansion. Suppose the k sources are outside of the sphere of radius a centered at the origin. The center of a local expansion is defined by the center of the sphere that contains all of the evaluation points (P) as shown in figure 2.4. The potential due to the far-field sources at any near field point, $P(r,\theta,\phi)$, inside of the sphere is given by,

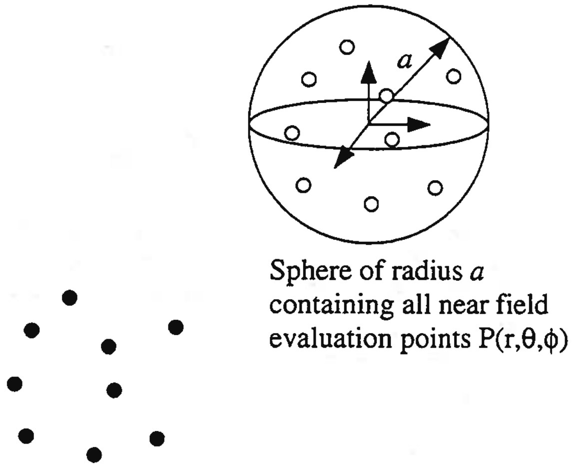

Sphere of radius *a* containing all near field evaluation points P(r,θ,ϕ)

Far field source points σ*i*(ρ*i*,α*i*,β*i*) located anywhere outside the sphere

Figure 2.4: Local expansion

$$\Phi(P) = \sum_{n=0}^{\infty}\sum_{m=-n}^{n} r^n L_n^m Y_n^m(\theta,\phi) \tag{2.36}$$

where the coefficients are given by,

$$L_n^m = \sum_{i=1}^{k} \frac{\sigma_i}{\rho_i^{n+1}} Y_n^{-m}(\alpha_i,\beta_i). \tag{2.37}$$

Truncating at p terms yields,

$$\left| \Phi(P) - \sum_{n=0}^{p} \sum_{m=-n}^{n} r^n L_n^m Y_n^m(\theta, \phi) \right| \leq \frac{\sum_{i=1}^{k} |\sigma_i|}{a-r} \left(\frac{r}{a} \right)^{p+1} \tag{2.38}$$

Several theorems are used in the multipole algorithm involving shifting the origins of multipole and local expansions and the conversion of multipole expansions into local expansions. See Greengard [17] for the development of these theorems and their truncation error bounds as well as proofs for the error bounds mentioned above. For completeness, the shifting and conversion theorems are reproduced in Appendix A.

There are a wide variety of $N \log N$ algorithms for accelerating the evaluation of N potentials due to N sources, typically these are based on some form of hierarchical clustering. The underlying idea is that the potential due to a cluster of source points may be evaluated at some distant point P by first accumulating the source influences into a multipole expansion, and then evaluating the single expansion. It is the careful arrangement of the clusters of source points that leads to the $N \log N$ efficiency. The fast-multipole algorithm reduces the cost yet further, to order N, by a complementary arrangement of the evaluation points so that accumulated multipole expansions may be transformed to local expansions centered in the clusters of evaluation points, and these expansions are evaluated instead. More specifically, the use of multipole and local expansions is orchestrated by a tree-structured hierarchy of source clusters and evaluation point clusters. Multipole expansions for clusters of sources are accumulated from the *leaves* of the tree to the *root*, and local expansions are distributed from the root to the leaves for evaluation at collocation points. This is accomplished in essentially order N operations while maintaining uniform precision as shown in Greengard [17].

Local and multipole expansions must be carefully applied to insure that the potential is accurately approximated everywhere in the problem domain. The structure that makes this possible is the hierarchical partitioning of the domain. For the computations herein, the multipole algorithm is applied only to the free surface domain. Since the free surface lies more or less in a plane with the elevations representing small deviations, the three-dimensional hierarchical tree structure can be collapsed into a two-dimensional "pancake". This simplifies some of the logic required in partitioning the domain. A description of the multipole algorithm for the free surface domain follows.

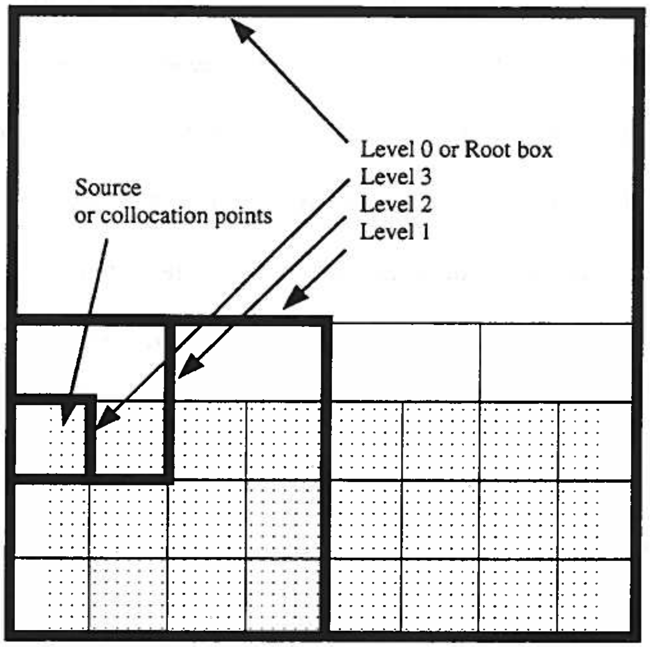

Figure 2.5: Typical hierarchical tree structure

1. Define a square region in the $z = 0$ plane containing all of the $x - y$ collocation and desingularized source point coordinates associated with the free surface. Call this the level 0 or root box.

2. Create a hierarchical tree structure by recursively dividing the region into four

subregions. The level 0 box is divided into four *child* boxes at level 1. The four level 1 boxes are divided into sixteen level 2 boxes and so on up to the finest tree level. When a box is divided, it is referred to as the *parent* of it's four *children.* Figure 2.5 shows a typical two-dimensional hierarchy. In the desingularized method, the source points are directly above (in the +z direction) the collocation points. This guarantees that a source point and its corresponding collocation point will be in the same box. Therefore, the source and collocation point clusters will have the same hierarchy. The "pancake" hierarchy is oriented in the $x - y$ plane and positioned at the calm water level ($z = 0$).

3. For each box at the finest tree level, form a multipole expansion for the source points in the box. The potential at any point outside a circle circumscribing this box can be evaluated using this expansion.

4. Starting at the finest tree level, shift the centers of the four *child* multipole expansions to the center of their *parent* box and add them together. Continue this procedure up to level 2. This will produce multipole expansions for every box in the tree up to level 2.

5. Define a *nearest neighbor* of box$_i$ as a box that shares a side or corner with box$_i$ and is on the same level. Each box has at most eight nearest neighbors. A box is *well separated* from box$_i$ if it has at least one nearest neighbor between it and box$_i$. Define box$_i$'s *interaction list* as the set of boxes that are the children of the nearest neighbors of box$_i$'s parent and that are well separated from box$_i$. The boxes on levels 0 and 1 will have empty interaction lists. Therefore, starting at level 2, use the multipole to local expansion conversion formula

to convert the multipole expansions in each box in the interaction list to a local expansion in box$_i$. Add the local expansions created from the multipole expansions in the interaction list together. While remaining at level 2, use the local expansion shift formula to shift the center of the local expansion in each box to its children. Proceed to the next level and repeat the procedure until the finest level is reached. There now exists, for each box at the finest tree level, a local expansion representing the influence of all sources that are not in the box itself or its nearest neighbors. Figure 2.6 shows the multipole and local expansion manipulation.

6. Compute the potential at all the collocation points in each box in the finest tree level. The potential due to far-field sources is computed by evaluating the local expansion at each collocation point. The potential due to sources in the box and it's nearest neighbors is computed directly. The two potentials are added together to yield the potential due to all the source points in the free surface domain.

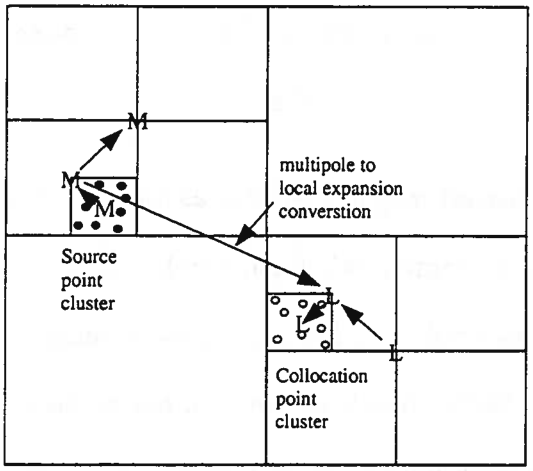

Figure 2.6: Multipole and local expansion manipulation

The gradient of the potential can be computed in a similar fashion. The velocities induced by the n near-field source points are computed directly.

$$\nabla\Phi(\vec{x}_i)_{near-field} = \sum_{j=1}^{n} \sigma_j \nabla_{\vec{x}_i}(G_{ij}) \tag{2.39}$$

Velocities induced by far-field source points are computed by taking the gradient of the local expansions in spherical coordinates and then transforming the spherical gradient into a Cartesian gradient. The derivatives with respect to the spherical coordinates are,

$$\frac{\partial\Phi}{\partial r}_{far-field} = \sum_{n=0}^{p} \sum_{m=-n}^{n} n r^{n-1} L_n^m Y_n^m(\theta,\phi) \tag{2.40}$$

$$\frac{\partial\Phi}{\partial \theta}_{far-field} = \sum_{n=0}^{p} \sum_{m=-n}^{n} r^{n} L_n^m \frac{\partial}{\partial\theta} Y_n^m(\theta,\phi) \tag{2.41}$$

$$\frac{\partial\Phi}{\partial \phi}_{far-field} = \sum_{n=0}^{p} \sum_{m=-n}^{n} r^{n} L_n^m \frac{\partial}{\partial\phi} Y_n^m(\theta,\phi) \tag{2.42}$$

The θ-derivative of the Legendre polynomials is computed using

$$\sin\theta \frac{d}{d\theta}\left(P_n^{|m|}(\cos\theta)\right) = (n-m+1)P_{n+1}^{|m|}(\cos\theta) - (n-1)\cos\theta P_n^{|m|}(\cos\theta) \tag{2.43}$$

Near-field and far-field velocities can then be summed to yield the total perturbation velocity induced by sources above the free surface on collocation points on the free surface. The θ-derivative of the far-field expansion is undefined when $\sin\theta = 0$. This special case occurs when a collocation point is directly above or below the center of an expansion. No simplification was found to enable the computation of the θ-derivative at this point. Therefore, for this case, the gradient of the potential is computed by summing the influence of all the source points above the free surface.

2.3.4 Preconditioning

As previously mentioned, the influence matrix, A_{ij}, may suffer from poor conditioning with large changes in grid spacing and increasing desingularized distance.

The convergence of the iterative solver can be greatly improved if a good approximation for the inverse of A_{ij} is readily available and not too expensive to compute. If the approximation to A_{ij}^{-1} is $\tilde{A}_{jk}$ then the iterative solver can be preconditioned by solving the following problem,

$$A_{ij}\tilde{A}_{jk}s_k = b_i \tag{2.44}$$

for s_k where s_k is related to the source strength by $\sigma_j = \tilde{A}_{jk}s_k$.

For preconditioning the multipole algorithm, an overlapping block preconditioner is used [31]. The approximate inverse $\tilde{A}_{jk}$ is computed by solving overlapping subproblems in the multipole algorithm. Specifically, the nearest neighbors in the hierarchical tree structure are used. For each box in the finest tree level, an influence matrix is formed consisting of source and collocation points in the box itself and it's nearest neighbors. These sub-influence matrices are inverted. Only the inverted coefficients which represent the influence of source points on collocation points in the box are saved and loaded into appropriate locations in the $\tilde{A}_{jk}$ matrix. Inverted coefficients in the nearest neighbor boxes are discarded. The $\tilde{A}_{jk}$ matrix is now sparsely populated and contains information about the local inverse problems. The work and storage requirements for the preconditioner are consistent with the multipole algorithm [31]. Thus, the preconditioned multipole solution procedure remains an $O(N)$ process.

CHAPTER III

MULTIPOLE ALGORITHM ACCURACY AND EFFICIENCY

In this chapter, a series of simple problems are solved to demonstrate the accuracy and efficiency of the multipole algorithm. The problem is that of a source-sink pair below an equipotential surface at $z = 0$. The number of unknowns in the problem is then varied. Solution time and memory allocation for several solution methods is studied as a measure of efficiency. Accuracy is demonstrated by increasing the order (p) of the multipole expansions and computing the solution error relative to an exact solution.

3.1 Problem Formulation

The fluid is infinitely deep and the truncation boundary conditions are unspecified. A $\Phi = 0$ boundary condition is prescribed on the $z = 0$ plane. The potential due to the source and sink is defined as $\Phi = \sigma/r$. The source has strength $\sigma = 1$ and location $\vec{x} = (-1, 0, -1)$. The sink has strength $\sigma = -1$ and location $\vec{x} = (1, 0, -1)$. The computational domain is defined by,

$$-20 \leq x \leq 20,$$
$$0 \leq y \leq 10,$$
$$z = 0$$

and $y = 0$ is a symmetry plane.

N desingularized source points are distributed above the $z = 0$ plane. The potential can then be found by summing the influence of the sources above the $z = 0$ plane and the isolated source-sink pair. Enforcing the $\Phi = 0$ boundary condition at N collocation points on $z = 0$ results in a linear system of the form $A\sigma = \Phi$.

The iterative solver GMRES is used to solve for the desingularized source strengths. The convergence criterion for GMRES is defined as follows,

$$RES = \sqrt{\sum_{i=1}^{N}\left(\sum_{j=1}^{N}(A_{ij}\sigma_j) - b_i\right)^2} < \sqrt{N} \times 10^{-6} \tag{3.1}$$

where RES is the residual error. Several solution options are investigated for comparative purposes. They are,

1. A *direct* application of GMRES. No multipole acceleration or preconditioning is employed.
2. Multipole accelerated solution with no preconditioning.
3. Direct solution with preconditioning.
4. Multipole accelerated solution with preconditioning.

For the multipole accelerated solutions the number of levels (L) in the hierarchical tree structure is also varied. The computations were carried out using single precision arithmetic on a Silicon Graphics Power Challenge GR parallel computer with 16 R10000 processors and 2GB RAM. Although this computer has some auto-parallelization tools, the code was run in serial mode so as not to confuse the effects of parallelization with those due to multipole acceleration.

3.2 Results and Discussion

For each solution, the solution time and memory allocation were recorded. Figure 3.1 shows the solution time (t_{solve}) in seconds versus the number of nodes (N) for solutions with no preconditioning (solutions 1 and 2). As expected, the direct solution time increases like N^2. As N becomes large, the solution time becomes excessive. The multipole accelerated solution times increase approximately linearly with N. As the number of levels in the tree hierarchy is increased the slope of curves becomes flatter. This is due to the n^2 cost of evaluating near-field influence coefficients. n is the number of unknowns in the local problem (a box and it's nearest neighbors). The selection of an appropriate number of levels for the tree hierarchy is problem dependent but in general the number of levels needs to be increased with increasing N. When N becomes large, a significant savings in solution time relative to the direct solution is realized.

Figure 3.2 shows the memory allocation versus number of nodes for solutions with no preconditioning. Similar to solution time, the memory allocation for the direct solution increases like N^2. As N becomes large the memory allocation rapidly becomes excessive. The allocation for the multipole solution increases approximately linearly with N. This allows problems with large numbers of unknowns to be run efficiently on high end workstations. Similar to the trend with solution time, the slope of the curves becomes flatter with increasing L suggesting that L should be increased with increasing N.

The number of iterations needed for GMRES to converge for the above cases was about 40 (±3). For a real ship flow problem the number of iterations to convergence can be significantly larger. To improve the iterative convergence, the overlapping block preconditioner is employed for solutions 3. and 4.

Figure 3.3 shows the solution time versus the number of nodes (N) for solutions with preconditioning (3. and 4.). Once again the direct solution time is increasing like N^2 but is significantly less than the solution time for case 1. The multipole solution times are also lower when preconditioning is used. The overlapping block preconditioner allows GMRES to converge in 4 (±1) iterations rather than the 40 required when no preconditioning is employed. The cost of generating the preconditioning matrix is not included in the solution times shown in figure 3.3. In a time domain problem, the preconditioning matrix need only be computed once at the beginning of the simulation while the boundary value problem for the potential must be solved at each time step. Therefore, the cost of generating the preconditioner can be amortized over the number of time steps in the simulation. The curves for $L = 3$ and $L = 4$ are not continued out to $N = 5000$ because of the excessive cost of computing the preconditioning matrix.

The memory requirement for solutions with preconditioning is shown in figure 3.4. The allocations are higher than solutions with no preconditioning but the trends are the same. The increase in memory allocation is due to the storage requirements for the preconditioning matrix.

The cost of computing the preconditioning matrix is shown in figure 3.5 where the time to set up the preconditioning matrix ($t_{preconditioner}$) is plotted versus the number unknowns (N) for various levels in the tree structure (L). The cost rapidly becomes excessive when the number of levels in the hierarchical tree structure is small. This happens because the direct inversion of the overlapping subproblems is an $O(n^3)$ process, where n is the number of unknowns in each subproblem. As L increases, n decreases because the subproblems get smaller, thus reducing the cost of the preconditioner. For the direct solution with preconditioning, an $L = 5$ tree structure was used to generate the preconditioning matrix. Choosing an appropriate L is problem specific and depends on the number of unknowns, the number of time steps and the spatial distribution of the unknowns.

The above multipole calculations were computed using an expansion order (p) of 3. In order to investigate the multipole algorithm accuracy, the source strength above the $z = 0$ plane is assumed known and the potential on $z = 0$ is computed. The error for the multipole algorithm relative the direct calculation is,

$$E = \sqrt{\sum_{i=1}^{N}(\phi_{direct} - \phi_{multipole})^2} \tag{3.2}$$

where ϕ_{direct} is the potential computed directly from the given source strengths and locations and $\phi_{multipole}$ is the potential computed using the multipole algorithm. The number of unknowns (N) and tree levels (L) are held constant at 2000 and 4 respectively while the expansion order (p) is varied. Figure 3.6 indicates the accuracy of the multipole algorithm with increasing expansion order. The error (E) is plotted on a log scale. The constant slope of the line on the semi-log plot indicates exponential decay in the error with increasing p.

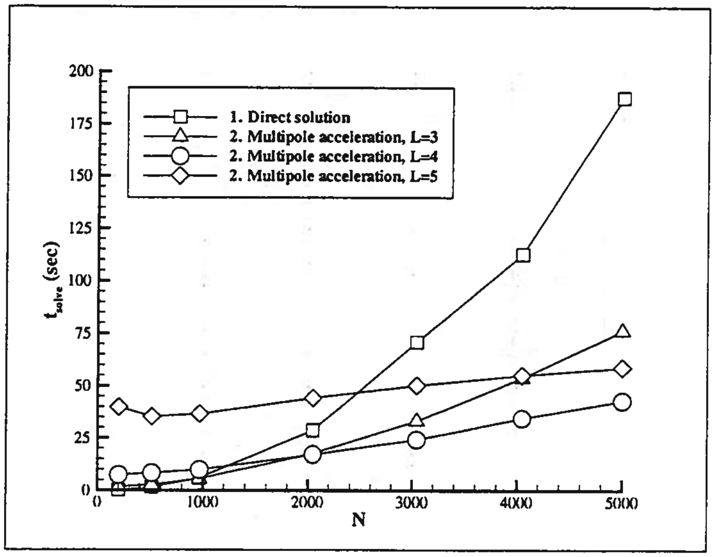

Figure 3.1: Solution time with no preconditioning

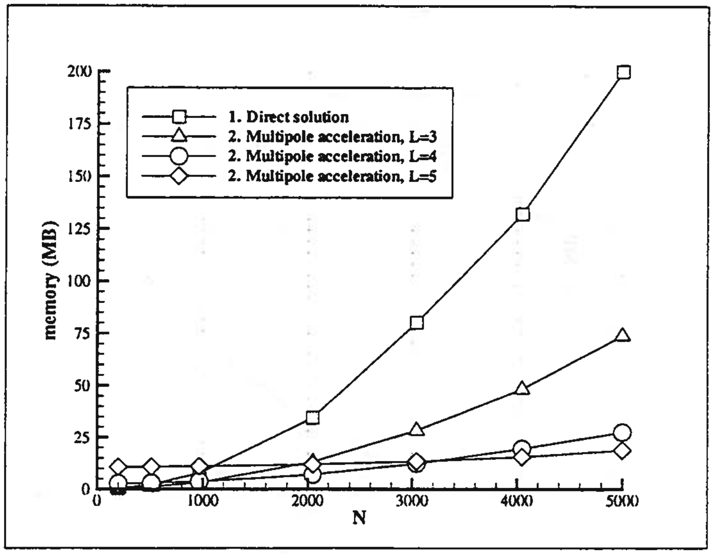

Figure 3.2: Memory allocation with no preconditioning

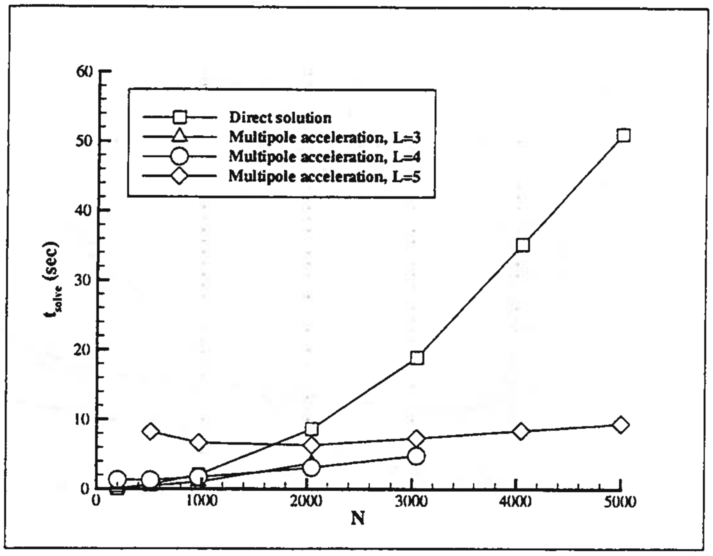

Figure 3.3: Solution time with preconditioning

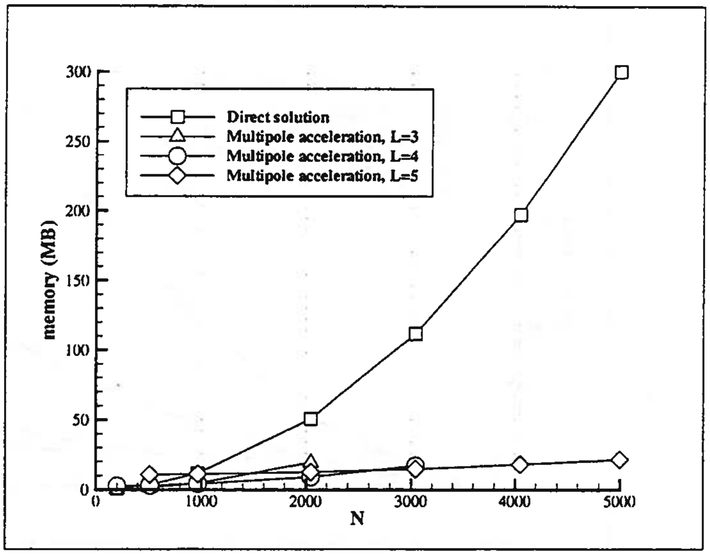

Figure 3.4: Memory allocation with preconditioning

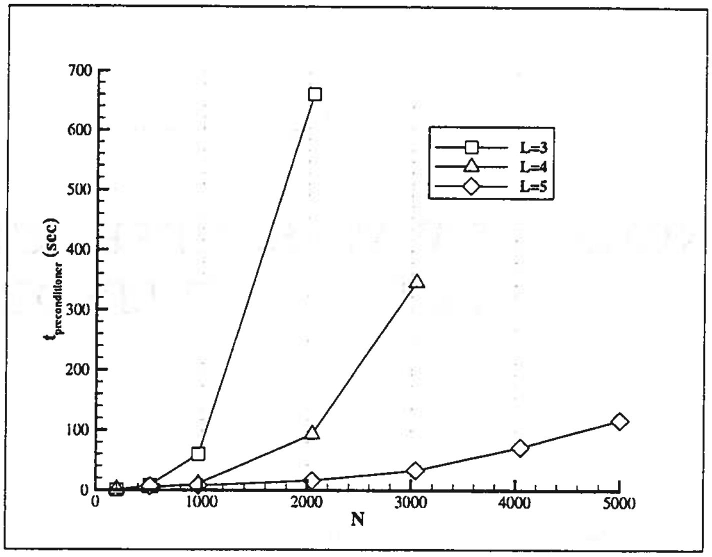

Figure 3.5: Cost of preconditioning

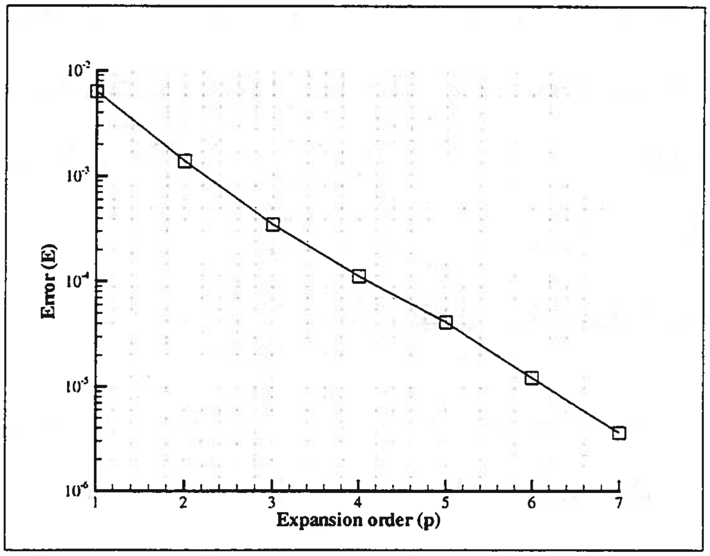

Figure 3.6: Accuracy of the multipole algorithm

CHAPTER IV

INCIDENT WAVES DIFFRACTED BY A VERTICAL CYLINDER

One of the benchmark problems in the offshore industry is that of wave diffraction by cylindrical bodies. Nestegård [34] administered a Det Norske Veritas (DNV) survey in which the problem of wave diffraction by a vertical cylinder founded on the bottom of a finite depth basin was studied. In this chapter, the DELTA method is applied to this problem. This problem presents some important physical and numerical issues. Since this is a zero speed problem, the treatment of the truncation boundary conditions has a significant effect on long time simulations. Also, for highly nonlinear incident waves, spray around the cylinder and wave breaking become important issues.

4.1 Problem Formulation

Figure 4.1 shows the problem set up, where k is the wave number, R is the cylinder radius, H is the tank depth, and A is the incident wave amplitude defined as wave height divided by two. The incident waves are generated by a piston wave maker on the upstream boundary and allowed to propagate downstream obeying the fully nonlinear free surface boundary conditions. The form of the free surface boundary

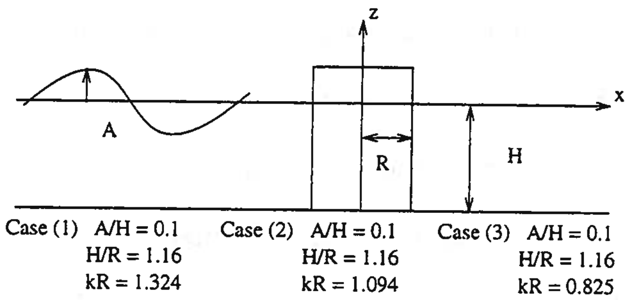

Figure 4.1: Problem set up

conditions used here is,

$$\frac{\delta \eta}{\delta t} = \frac{\partial \phi}{\partial z} - (\nabla \phi - \vec{v}) \cdot \nabla \eta \tag{4.1}$$

and

$$\frac{\delta \phi}{\delta t} = -g\eta - \frac{1}{2} \nabla \phi \cdot \nabla \phi + \vec{v} \cdot \nabla \phi - \frac{P_a}{\rho}. \tag{4.2}$$

Where $\frac{\delta}{\delta t} = \frac{\partial}{\partial t} + \vec{v} \cdot \nabla$ and $\vec{v} = (u, v, \frac{\delta \eta}{\delta t})$. u and v are the prescribed velocities for the horizontal plane motion of the free surface collocation points. u is allowed to move with the fluid velocity, $u = \frac{\partial \phi}{\partial x}$, and v is prescribed so that collocation points move on prescribed paths around the body. The resulting free surface boundary conditions are,

$$\frac{\delta \eta}{\delta t} = \frac{\partial \phi}{\partial z} - \left(\frac{\partial \phi}{\partial y} - v \right) \frac{\partial \eta}{\partial y} \tag{4.3}$$

and

$$\frac{\delta \phi}{\delta t} = -\frac{p_a}{\rho} - g\eta - \frac{1}{2} \nabla \phi \cdot \nabla \phi + \frac{\partial \phi^2}{\partial x} + v \frac{\partial \phi}{\partial y} + \frac{\partial \phi}{\partial z} \frac{\delta \eta}{\delta t}. \tag{4.4}$$

The kinematic condition must be computed first to allow inclusion of the $\frac{\partial \phi}{\partial z} \frac{\delta \eta}{\delta t}$ term in the dynamic condition. This formulation has the desired effect of restricting collocation points from passing through the body boundary. An alternative free surface boundary condition would be to set $\vec{v} = \left(0, 0, \frac{\delta \eta}{\delta t}\right)$. In this case $\frac{\delta \eta}{\delta t} = \frac{\partial \eta}{\partial t}$ and the collocation points move vertically up and down, tracking the free surface elevations at points in the $x - y$ plane like wave probes. The advantage of this scheme is that no regriding of the free surface after each time step is required. The disadvantage is that the free surface slope, $\nabla\eta$, must be computed numerically. $\nabla\eta$ may be difficult to compute accurately in a three-dimensional problem, especially at the boundaries of the free surface domain where one sided differencing must be used. The free surface/body intersection line is where this problem would be most detrimental.

The truncation boundary conditions are treated like vertical walls. All of the wave energy that reaches the truncation boundaries is reflected back into the basin. By using wall truncation boundaries, the simulation is limited by the time is takes the incident and diffracted waves to reflect off the walls and reach the body. The bottom boundary and center plane ($y = 0$) are included by symmetry.

Three incident wave cases are studied as shown in figure 4.1. The incident wave amplitude and tank depth are held constant while the wave number varies. For each case the non-dimensional horizontal force, defined as $F_x^* = F_x/\rho g R^2 A$, is calculated by integrating the hydrodynamic pressure over the body. Results are compared with experiments by Chakrabarti [12] and calculations by Yang and Ertekin [48].

4.2 Results and Discussion

Figure 4.2 shows the free surface at the point of maximum wave run-up for case(1). The piston wave maker and truncation boundaries are not shown. Contours of the free surface elevations are shown at the base of the cylinder. The waves are generated on the right side of the domain and propagate downstream in the positive x direction past the cylinder. 2136 collocation points discretize the free surface, 55 on the cylinder, 140 on the piston wave maker, 140 on the downstream truncation boundary and 380 on the outer truncation boundary for a total of 2851 collocation points. The symmetry of the bottom and centerline are included using image sources in the appropriate locations. The figure shows the significance of the run-up relative to the amplitude of the incident wave. Wave run-up was computed to be as large as two times the incident wave amplitude.

Figure 4.3 shows the horizontal exciting force time histories indicating the convergence of the method for case(1). Here $t^* = t/T$, where T is the incident wave period. The fine grid has 2851 collocation points as mentioned above. The coarse grid has 900 points on the free surface, 55 on the cylinder, 75 on the piston wave maker, 75 on the downstream truncation boundary and 200 on the outer truncation boundary for a total of 1305 collocation points. The difference in horizontal force amplitude has converged to less than 2% relative error.

Figure 4.4 shows the time histories of the non-dimensional force. The forces reach steady state after the initial incident wave passes. Simulations were terminated due to the presence of reflected waves from the outer boundaries. The case(3) simulation was terminated earlier because of the higher wave speed. The purpose of the DNV study was to compare results obtained by various nonlinear inviscid water wave codes. These results are shown in Beck and Scorpio [5] for case(1), the maximum horizontal force and wave run-up compare favorably with results published in the DNV study. However, there is enough scatter to indicate that more research is required to improve the consistency of three-dimensional calculations. The three cases studied here correspond to experiments by Chakrabarti [12] and calculations by Yang and Ertekin [48].

Table 4.1 shows the comparison of maximum non-dimensional horizontal force experienced by the cylinder. Yang and Ertekin used a boundary element method with source panels distributed on the free surface to solve the field equation at each time step. Stokes 2^{nd} order waves were used to create the incident waves on the upstream boundary and an extended Sommerfeld radiation condition was applied on the outer boundaries. The computational methods and boundary conditions of Yang and Ertekin are quite different from the desingularized method used herein, yet the results show reasonable agreement with each other and with the experiments.

There are some computational issues that warrant discussion. One is the treatment of the far-field boundaries. For the present calculations, the far-field is simply truncated with vertical walls. This method is physically accurate but it limits the temporal length of the simulation because of wave reflection off the walls. Another issue that arises with the use of walls is the sensitivity of the tank to slosh modes. The extended Sommerfeld condition used by Yang and Ertekin apparently worked well for this problem. An accurate determination of phase speed for the outgoing waves, which is critical when using the Sommerfeld condition, may be difficult to obtain for more complicated problems such as body motions and forward speed. Further research is required to produce a radiation boundary condition acceptable for fully nonlinear wave problems in general.

Another issue is that of spray and breaking waves. Nonlinear computational methods are most useful for studying extreme cases where linear theories are invalid. Highly nonlinear behavior is often accompanied by spray and wave breaking. Numerically, these phenomena cannot be modeled using the present Euler-Lagrange method. One method to avoid these problems is to include an artificial energy absorber in the local vicinity of the spray or breaking wave. This has the effect of suppressing the spray root or the overturning wave crest. An argument can be made that this method has some physical basis in that spray formation and wave breaking are dissipative processes. Whether the numerical post- spray or breaking wave field is at all similar to the physical one may be the subject of future research. See Beck *et al.* [3] for some computational results on two-dimensional spray absorption.

Case	Experiments Chakrabarti	Calculations		% difference	
		Yang & Ertekin	Present	from Yang & Ertekin	from experiment
1	3.07	3.14	2.98	5.1	2.9
2	3.45	3.41	3.42	0.3	0.9
3	4.14	4.09	4.00	2.2	3.4

Table 4.1: Comparison of maximum horizontal force

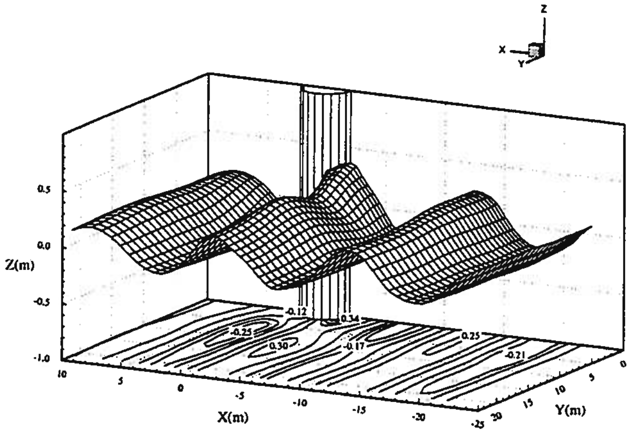

Figure 4.2: Isometric view and contour plot of the free surface elevation for case (1)

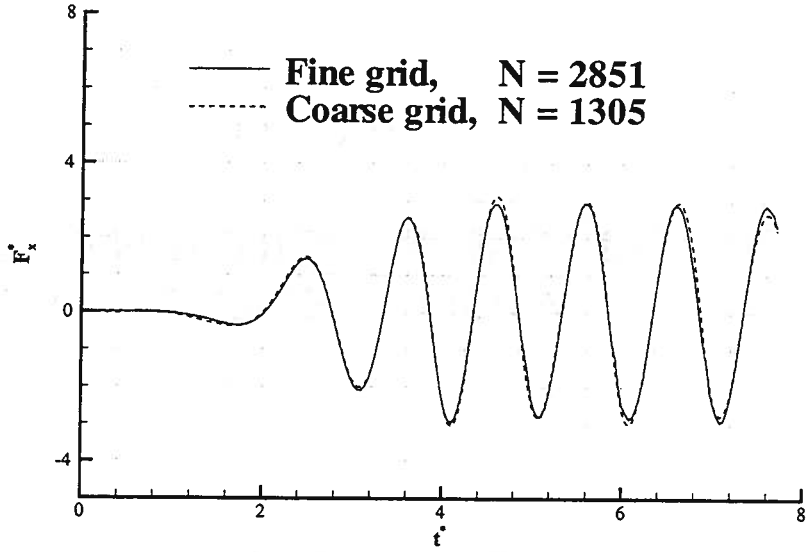

Figure 4.3: Convergence of the horizontal force time histories for case(1). Coarse grid, N = 1305; Fine grid, N = 2851.

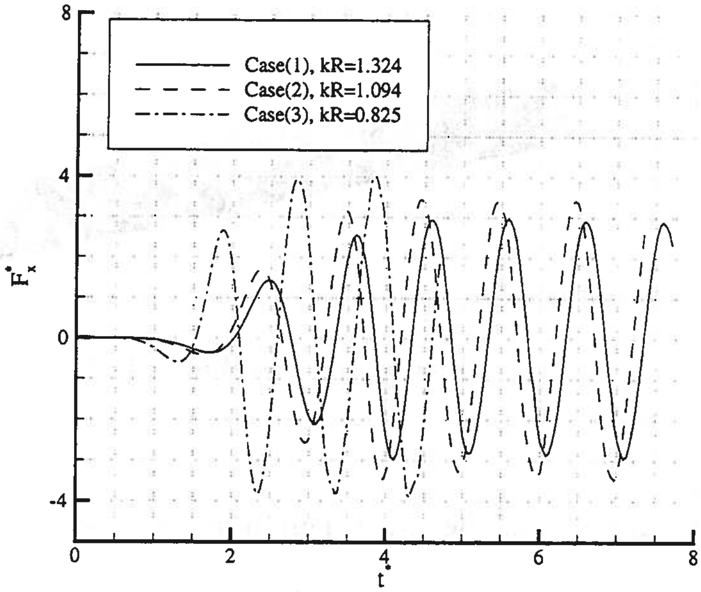

Figure 4.4: Horizontal force time histories

CHAPTER V

NUMERICAL EXPERIMENTS ON THE WIGLEY HULL FORM

In this chapter, the DELTA method is applied to the problem of a mathematical hull form, the Wigley hull, advancing at steady forward speed through both calm water and head seas. Results are compared with experiments and several important numerical issues relative to this problem are discussed.

5.1 Problem Formulation

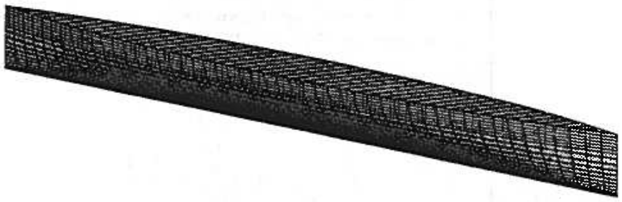

Figure 5.1: The Wigley hull

The Wigley hull is a mathematical hull form who's offsets are defined by,

$$y(x,z) = \frac{B}{2}\left(1-\left(\frac{2x}{L}\right)^2\right)\left(1-\left(\frac{z}{T}\right)^2\right)\left(1+a_2\left(\frac{2x}{L}\right)^2\right)$$

$$\begin{aligned} \text{where} \quad L &= \text{length} \\ B &= \text{beam} \\ T &= \text{draft} \\ a_2 &= 0.0 \text{ for the standard hull} \\ &= 0.2 \text{ for the modified Wigley hull III.} \end{aligned} \tag{5.1}$$

$\frac{L}{B} = 10$ and $\frac{B}{T} = 1.6$ for both the standard hull and modified hull III. Computed calm water resistances of the standard hull are compared with experiments in Noblesse and McCarthy [36]. Exciting force calculations for the modified Wigley hull III running through head seas are compared with experiments in Journée [21].

Laplace's equation governs in the fluid domain and the boundary conditions are as follows. The condition of infinite fluid depth is automatically satisfied by the Rankine source Green's function ($\nabla G \to 0 \quad \text{as} \quad z \to -\infty$). The boundary condition on the body surface is,

$$\vec{n} \cdot \nabla\phi = -\vec{n} \cdot \vec{U} + \vec{n} \cdot \vec{V_h} \qquad \vec{x} \in S_h. \tag{5.2}$$

On the upstream truncation surface,

$$\nabla\phi = 0 \qquad \vec{x} \in S_t. \tag{5.3}$$

This implies steady streaming flow on the upstream boundary. This means we are restricted to speeds where $\tau > \frac{1}{4}$. On the outer truncation surface,

$$\vec{n} \cdot \nabla\phi = -\vec{n} \cdot \vec{U} \qquad \vec{x} \in S_t. \tag{5.4}$$

The outer truncation surface is a vertical wall, reflecting wave energy back into the problem domain similar to an experimental towing tank. The downstream truncation boundary is unspecified. There is, however, an implied radiation condition on the downstream boundary. The natural downstream convection of free surface nodes tends to carry information out of the problem domain. Numerical experiments suggest that this convection works reasonably well as a radiation boundary condition for forward speed problems. No proof as to the mathematical validity of this boundary condition is supplied in this thesis.

As free surface nodes drift downstream with the fluid velocity, there is a danger of nodes drifting through the discretized body surface during intermediate time steps of the simulation. This problem can be eliminated by using a special form of the free surface boundary conditions allowing the horizontal plane motions of the free surface nodes to be prescribed as mentioned in chapter II. In this case, the nodes are allowed to convect downstream with the fluid velocity in the x-direction while the y-velocity component is prescribed to allow nodes to move around the body instead of through it. More specifically, the velocity of the free surface nodes is $\vec{v} = \left(U_1 + \frac{\partial\phi}{\partial x}, v, \frac{\delta\eta}{\delta t}\right)$ and the free surface boundary conditions take the form,

$$\frac{\delta\eta}{\delta t} = \frac{\partial\phi}{\partial z} - \left(\frac{\partial\phi}{\partial y} - v\right)\frac{\partial\eta}{\partial y} \tag{5.5}$$

$$\frac{\delta\phi}{\delta t} = -\frac{p_a}{\rho} - g\eta - \frac{1}{2}|\nabla\phi|^2 + v\frac{\partial\phi}{\partial y} + \frac{\partial\phi}{\partial z}\frac{\delta\eta}{\delta t} + \left(\frac{\partial\phi}{\partial x}\right)^2 \tag{5.6}$$

where $\frac{\delta}{\delta t} = \frac{\partial}{\partial t} + \vec{v}\cdot\nabla$ is the Lagrangian derivative moving with the free surface nodes. U_1 is the x-component of the free stream velocity (or, the forward speed of the hull). The y-velocity (v) is specified by forcing the free surface nodes to move along prescribed paths around the body. Therefore, if the path has slope $\frac{dy}{dx}$, then the prescribed velocity would be $v = \left(U_1 + \frac{\partial\phi}{\partial x}\right)\frac{dy}{dx}$.

There are some important numerical issues hidden behind this choice of free surface boundary condition that are worth mentioning. Since we are prescribing horizontal velocities, why not fix the x-y plane motions of the nodes, $\vec{v} = \left(0, 0, \frac{\partial \eta}{\partial t}\right)$? The free surface nodes would simply move up and down in the z-direction, eliminating the need to regrid the free surface. The reason this choice is avoided for forward speed problems is because the term $\left(U_1 + \frac{\partial \phi}{\partial x}\right) \frac{\partial \eta}{\partial x}$ appears in the kinematic free surface boundary condition. The free surface slope $\left(\frac{\partial \eta}{\partial x}\right)$ must be computed numerically, usually by a simple differencing scheme. The magnitude of the perturbation velocity is much less than the free stream velocity for much of the fluid domain making this term relatively large for high speed problems. Any errors introduced from computing free surface slopes would then be amplified in the kinematic boundary condition. On the other hand, by allowing the free surface nodes to convect downstream with the fluid velocity, the term involving $\frac{\partial \eta}{\partial x}$ is eliminated. The $\left(\frac{\partial \phi}{\partial y} - v\right) \frac{\partial \eta}{\partial y}$ term remains, but since the quantity $\left(\frac{\partial \phi}{\partial y} - v\right)$ is small, the effect of errors in the $\frac{\partial \eta}{\partial y}$ calculation are minimized.

5.1.1 Treatment of the bow and stern stagnation points

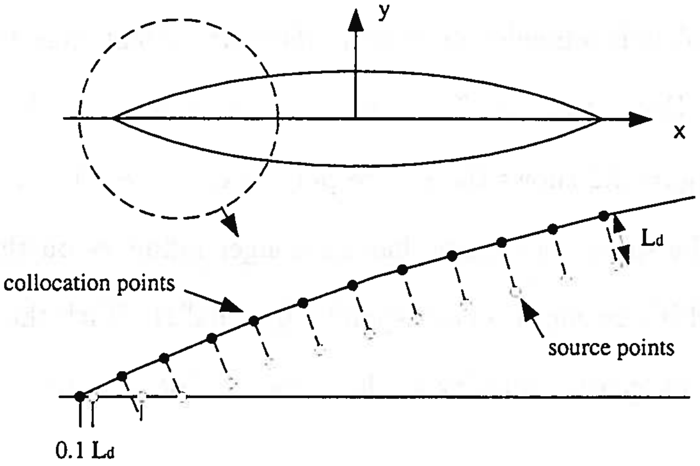

Figure 5.2: Discretization on the Karman-Trefftz airfoil

Another issue that arises in the DELTA method involves the discretization near stagnation points. Stagnation points occur at the leading and trailing edges of any body moving through a fluid. Similar flow regions exist near the bow and stern of a ship hull. In order to investigate the flow details in these areas, the steady flow around a two-dimensional Karman-Trefftz airfoil in an infinite fluid is studied. The exact solution to this problem is known. Figure 5.2 shows the discretization near the leading edge of the airfoil. Source points are desingularized by submerging them inside the body by a distance L_d. If a source point crosses the centerline, the point is moved onto the centerline without changing it's x-coordinate. Difficulties occur in the desingularized method when the airfoil entrance angle is small. The collocation point at the leading edge has a corresponding source point placed a distance L_d away on the centerline, inside the body. At zero angle of attack, this collocation point is a stagnation point and the source strength must be large to cancel the free stream velocity. If the entrance angle is too small, this large source strength can induce a large tangential velocity on the next collocation point away from the stagnation point. This problem is remedied by moving the source point close to the stagnation point as shown in Beck *et al.* [3]. The same arguments apply to the trailing edge stagnation point. Figure 5.2 shows the source point a distance $0.1L_d$ away from the collocation point. The source point now has a stronger influence on the stagnation collocation point and it's strength is correspondingly smaller. With the smaller source strength, the large tangential velocity at the second collocation point is eliminated.

Figures 5.4 and 5.5 show the tangential velocity (V_t) on the Karman-Trefftz airfoil for an entrance angle of 45°. The points indicate the exact solution and the solid line is the desingularized solution using 60 nodes with cosine spacing in the x-direction.

The solutions agree to within 0.1% and are insensitive to desingularized distance at the stagnation points. When the entrance angle is reduced to 13.5°, the choice of desingularized distance becomes more important. Figures 5.6 and 5.7 show the tangential velocity for the 13.5° entrance angle. While the $0.1L_d$ case shows good agreement, there is a large spike in velocity for the $0.5L_d$ case because the source point is inducing a large tangential velocity at the second node.

The same type of behavior can be seen in three-dimensional problems. To illustrate this the Wigley hull double body problem is solved using various desingularization strategies and the resulting pressure coefficient on the forward half of the body is plotted. Figure 5.8 shows solutions with desingularized distances of $0.1L_d$ and $0.5L_d$ at the stagnation points. Since the Wigley hull has a fine entrance, the large desingularized distance results in a spike in the pressure near the bow. This pressure spike is eliminated simply by moving the source closer to the stagnation point. Prior to the resolution of this numerical detail the pressure spike near the bow was avoided by not placing collocation points on the bow. This discretization strategy, used in Beck et al. [2] resulted in an under-prediction of the pressure near the bow as shown in figure 5.9. The bow wave produced in the calm water resistance calculation was correspondingly low relative to experimental measurements. Subsequent calculations (see Beck [3]), where the stagnation regions were properly modeled by moving source points close to the stagnation points, produced bow waves that were much closer to the experiments.

5.1.2 Nonlinear incident waves with forward speed

For the modified Wigley hull III in head seas, a method must be contrived to introduce fully nonlinear incident waves in the ship fixed coordinate system moving in the $-x$ direction. In a numerical wave tank, only a small portion of the free surface can be modeled. Therefore, disturbances coming in from outside the computational window must enter through the boundary conditions. The incident waves are propagating down a long tank and must enter the computational window through the upstream boundary (for head seas). This is accomplished by preprocessing the incident waves in a long two-dimensional wave tank. The appropriate data is then stored for use as the upstream boundary condition in the three-dimensional computational window.

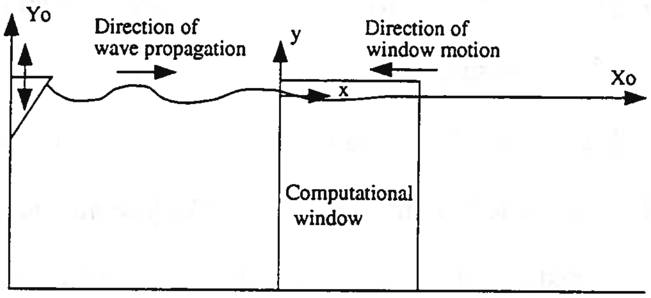

Figure 5.3: A two-dimensional wave making tank with a moving computational window

Figure 5.3 shows the two-dimensional wave making tank with a moving computational window. The wave maker is producing waves in the $X_o - Y_o$ reference frame. The waves are transferred into the computational window by prescribing appropriate boundary conditions where the window interfaces with the fluid in the tank. On the submerged edges of the window, $\frac{\partial \phi}{\partial n}$ is prescribed. Where the window intersects the free surface, the potential and elevation are prescribed. The flow computed inside the window, including free surface deformations, will match the flow in the two-dimensional tank. For the head seas problem the incident waves are diffracted by the body, making the recorded downstream boundary condition invalid. Therefore, the waves must enter the window by prescribing the upstream boundary condition only. The quality of the waves produced by this method is shown in figure 5.10 for various window velocities. The window velocity (U_o) is nondimensionalized using the Froude number based on incident wavelength, $Fr = U_o/\sqrt{g\lambda}$. Free surface elevations (η) and wave tank location (X_o) are scaled by the wavelength. The results indicate that this method produces reasonable nonlinear waves in a two-dimensional moving window with no body present. The validity of this method in a three-dimensional window with a body present will be investigated in the modified Wigley hull III head seas calculation.

5.2 Standard Wigley Hull, Calm Water Resistance

In this section, calm water resistance calculations on the standard Wigley hull are compared with experimental results published in Noblesse and McCarthy [36]. The problem is started from rest and the Wigley hull is slowly accelerated up to steady forward speed while sinkage and trim motions are restrained. The instantaneous body velocity is defined by

$$U_b(t) = U_o\left(1 - e^{-(\alpha g L)t^2}\right), \tag{5.7}$$

where g and L are the gravitational constant and hull length respectively, α is an acceleration parameter, and U_o is the steady body velocity. Wave resistance, sinkage force and trimming moment are computed at each time step by integrating pressure over the body surface. Since the body motion is prescribed in this problem, the hydrodynamic forces on the body can be post processed. If the simulation is at the n^{th} time step, then the pressure on the discretized body surface is computed at the

$(n-1)^{th}$ time step,

$$\begin{aligned} P^{n-1} &= -\rho\left(\frac{\delta\phi}{\delta t}\right)^{n-1} - \rho g z^{n-1} - \rho\left(U_b\frac{\partial\phi}{\partial x}\right)^{n-1} \\ &\quad -\frac{1}{2}\rho(\nabla\phi\cdot\nabla\phi)^{n-1} - \rho\left(\frac{\delta\vec{x}}{\delta t}\right)^{n-1}\cdot\nabla\phi^{n-1}. \end{aligned} \tag{5.8}$$

The pressure is computed at the $(n-1)^{th}$ time step specifically so that central differencing can be used for the time derivatives of the potential and node positions on the body,

$$\begin{aligned} \left(\frac{\delta\phi}{\delta t}\right)^{n-1} &= \frac{\phi^n - \phi^{n-2}}{2\Delta t} \\ \left(\frac{\delta\vec{x}}{\delta t}\right)^{n-1} &= \frac{\vec{x}^n - \vec{x}^{n-2}}{2\Delta t} \end{aligned} \tag{5.9}$$

where Δt is the time step size. The forces and moments are then computed using equations 2.17 and 2.18. This post processing produces sufficiently accurate forces and moments for problems where the body motion is prescribed. However, for free body motions, the hydrodynamic forces are needed at the current (or n^{th}) time step to solve the equations of rigid body dynamics. This means that a backwards difference scheme is needed to compute time derivatives on the body surface. Beck *et al.* [3] implemented an alternate method of finding $\frac{\delta\phi}{\delta t}$ on the body. They use the fact that $\frac{\delta\phi}{\delta t}$ is harmonic to set up a boundary value problem where $\frac{\delta\phi}{\delta t}$ is known on the free surface and $\frac{\partial}{\partial n}\left(\frac{\delta\phi}{\delta t}\right)$ is known on the body surface. The boundary integral formulation of this problem is of the same form as the one for the ϕ problem. Hence, the resulting linear system has the same influence coefficients as the linear system for ϕ. The end result is that the linear system must be solved twice, once where ϕ is known on the free surface and $\frac{\partial\phi}{\partial n}$ is known on the body surface and a second time where $\frac{\delta\phi}{\delta t}$ is known on the free surface and $\frac{\partial}{\partial n}\left(\frac{\delta\phi}{\delta t}\right)$ is known on the body surface. For an $O(N^2)$ solver this additional solution constitutes a significant additional cost when N becomes large and may be impractical. With a multipole accelerated $O(N)$ solver, the time required for the additional solution may be acceptable, even for large N.

Figure 5.11 shows a comparison of wave profiles along the hull. The experimental data was measured at the University of Tokyo on a 2.5 meter model fixed in sinkage and trim (cf. Noblesse and McCarthy [36]). Also shown are the results obtained by Beck et al. [2] with no collocation points directly on the bow and Beck *et al.* [3] with collocation points on the bow and source points moved in close ($0.01L_d$). The proper numerical treatment in the bow and stern regions produces a wave profile which is smoother and a bow wave which agrees quite well with experimental measurements. It is obvious from these results that correctly modeling the stagnation region is important for computing accurate free surface elevations in the bow and stern regions.

The following results report standard Wigley hull forward speed calculations for Froude numbers of 0.25, 0.27, 0.30, and 0.32. The model is fixed to sink and trim. Figures 5.12 through 5.15 show contours and isometric views of the free surface elevation. Solid contour lines indicate $z > 0$ while dashed lines are for $z < 0$. The computational grid is also overlayed on the plot. The grid is extended 1.2 ship lengths aft of the stern to resolve the far-field waves, half a ship length upstream, and 0.85 ship lengths in the y-direction. Collocation points are concentrated near the bow and stern regions to resolve high flow gradients. Only half of the grid is used for the computations ($y > 0$), the other half is simply a mirror image included for illustrative purposes. 3267 nodes are distributed on half the free surface and 663 on half the body wetted surface making a total of 3930 nodes. This grid was used for all cases. The reader is referred to Beck *et al.* [2] to review the convergence properties of the

DELTA method for this problem.

Figures 5.16 through 5.19 show wave cuts of the free surface elevation on the centerline and along the body and at distances of y/L = 0.1, 0.2, 0.3, and 0.4 away from the centerline. The free surface elevations are consistently smooth except for the bow wave at Fr = 0.32.

Figures 5.20 through 5.23 show nondimensional surge and heave forces and pitch moment. The nondimensional forces are defined by $F^* = F/(\frac{1}{2}\rho U_o^2 S)$ where S is the wetted surface of the hull in calm water. The pitch moment is taken about the origin with the positive moment corresponding to bow up trim. Notice the low frequency oscillation in the forces. These oscillations correspond to the $\tau = \frac{\omega U_o}{g} = \frac{1}{4}$ frequency and decay slowly with time. The corresponding period of the oscillations is, $T^*_{\frac{1}{4}} = T_{\frac{1}{4}}\sqrt{\frac{g}{L}} = \frac{2\pi}{\omega}\sqrt{\frac{g}{L}} = \frac{2\pi U_o}{1/4\sqrt{gL}} = 8\pi Fr$. By modifying the acceleration parameter, α, the amplitude of these oscillations can be reduced but not eliminated.

Figure 5.24 shows a comparison between computations and experimental measurements for the wave elevation along the body for a range of Froude numbers. The experiments are taken from Noblesse and McCarthy [36] page 22. Experiments were conducted at the University of Tokyo on a 2.5m model with fixed sink and trim. Experimental results are reported for Froude numbers of 0.250, 0.267, 0.289, 0.316, 0.354, and 0.408. The Fr = 0.25 computed results are compared directly with the experiments. For Fr = 0.267, 0.289, and 0.316, the computational wave elevations are linearly interpolated for comparison with elevations at the experimental Froude numbers. No comparison is made with Fr = 0.354 and 0.408. The results show excellent agreement with experiments over the range of Froude numbers, especially for the prediction of the bow wave height which is typically underpredicted by linear theories.

Figure 5.25 shows a comparison of the wave resistance coefficient versus Froude number. C_{pr}, C_w, and C_{wp} are the experimental coefficients from pressure integration, the residual resistance from the resistance test and wave pattern analysis respectively. C_{F1} is the computed resistance coefficient and is defined as the mean surge force once the hull reaches steady forward speed. The computed values are generally higher than the experimental values. The reason for the higher wave resistance is unknown. Significant integration errors in hydrostatic pressure integration that can occur for fore and aft asymmetric bodies do not apply to the fore and aft symmetric Wigley hull. A possible explanation is that the wave resistance is sensitive to the height and location of the bow and stern waves. The bow wave is typically under-predicted by panel methods. The DELTA method produces a larger bow wave that would increase the wave resistance. The real flow along the Wigley hull has a thin boundary layer and a separated region near the stern. The separated flow near the stern affects the size and location of the stern wave. Another possible explanation is that the displacement thickness of the separated boundary layer increases the apparent length of the body resulting in a lower wave resistance relative to the inviscid resistance.

5.3 Modified Wigley Hull III, Head Seas

In this section, exciting forces on the modified Wigley hull III are compared with experimental results published in Journée [21]. The problem is slowly accelerated up to steady forward speed in calm water and is restrained from sinkage and trim. Incident waves are generated in a two-dimensional tank. The moving window technique discussed in section 5.1.2 is used to introduce incident waves in the three-dimensional tank by prescribing appropriate upstream boundary conditions. Forces and moments are computed as in the calm water cases.

The following results report modified Wigley hull III calculations for Fr = 0.3 in head seas. The incident wave length for the computations is $\lambda/L = 0.5$. The wave steepness is $H/\lambda = 1/111$ and $1/20$. H is the wave height defined as half the distance from crest to trough.

Figure 5.26 shows contours of the free surface elevation and an isometric view of the free surface. As before, solid contour lines indicate $z > 0$ while dashed lines are for $z < 0$. The computational grid is also overlayed on the plot. The grid is extended one ship length aft of the stern to resolve the far-field waves, half a ship length upstream, and 0.6 ship lengths in the y-direction. Collocation points are concentrated near the bow and stern regions to resolve high flow gradients. Only half of the grid is used for the computations ($y > 0$), the other half is simply a mirror image included for illustrative purposes. 2486 nodes are distributed on half the free surface and 510 on half the body surface making a total of 2996 nodes. As in the calm water cases, this grid was used for all cases and the reader is again referred to Beck *et al.* [2] for the convergence study.

Figures 5.27 through 5.29 show nondimensional surge and heave exciting forces and pitch exciting moments on the Wigley hull III running through incident waves of steepness $H/\lambda = 1/111$. The problem is slowly accelerated from rest in calm water, reaching steady forward speed at $t^* = t\sqrt{g/L} = 14$. The calm water run is continued up to $t^* = 40$ when most of the start up transient has been left behind.

At this point the upstream incident wave boundary conditions are turned on and the wave front moves into the computational window. The Wigley hull (with fixed sinkage and trim) runs through the incident waves up to $t^* = 65$.

Figure 5.27 shows the nondimensional surge force ($F_1/(ka\rho g\nabla)$) and its components. k is the incident wave number, a is the incident wave amplitude, and $\rho g \nabla$ is the calm water displacement. The component forces are computed by integrating each term in the pressure equation (5.8) over the body wetted surface. F^*_{TOTAL} is the sum of the components. The two linear terms, $-\rho\delta\phi/\delta t$ and $-\rho U(t)\partial\phi/\partial x$ make the largest contribution to the surge force. The nonlinear terms, $-\rho g z$, $-0.5\rho\nabla\phi\cdot\nabla\phi$ and $\rho v\cdot\nabla\phi$ (here $v = \frac{\delta\vec{x}}{\delta t}$) are all an order of magnitude smaller as expected for these small amplitude linear waves. One of the advantages of the fully nonlinear calculation is that higher-order quantities such as added resistance in waves are automatically included. In this case, the added resistance is computed by comparing the calm water surge force with the mean exciting surge force in incident waves. The added resistance for this case is 13.2%, ie. the mean surge force in incident waves is 13.2% higher than the calm water surge force.

Figure 5.28 shows the nondimensional heave force ($F_3/(aC_{33})$) and its components. The heave force is similar to the surge force in that the linear terms dominate. The mean shift in the heave force is negligible at 0.2%.

Figure 5.29 shows the nondimensional pitch moment ($F_5/(kaC_{55})$) and its components. There is a noticeable low frequency oscillation with a period corresponding to the $\tau = 1/4$ frequency. Apparently, the pitch moment is more sensitive to unsteadiness left over from the start up transient. The mean shift in the pitch moment is

	Calculation DELTA	Experiment Journée
F_1^a	0.047	0.066
F_3^a	0.093	0.118
F_5^a	0.021	0.026

Table 5.1: Comparison of exciting force amplitudes.

also small at 1.75%

Table 5.1 compares the computed exciting force amplitudes (F_1^a, F_3^a, F_5^a) with experimental measurements conducted at DELFT University of Technology (Journée [21]). The computed values are in reasonable agreement with the experiments. Computational results including varying incident wave lengths are needed to accurately assess the comparison with experiments. This is ongoing work.

Figure 5.30 shows an isometric view of the free surface for the same incident wave length and Froude number where the incident wave amplitude has been increased so that $H/\lambda = 1/20$. An instability on the free surface occurred near the bow as the hull plunged into the wave front. The simulation broke down at this point. This figure is indicative of the complicated physics that are included in the nonlinear formulation requiring very careful numerical treatment. The spray event occurs at faster temporal and smaller spatial scales than are resolved in this simulation. The result is the unbounded growth of the free surface instability and subsequent breakdown of the numerical simulation. Further research is required to learn how to deal with the spray jet problem.

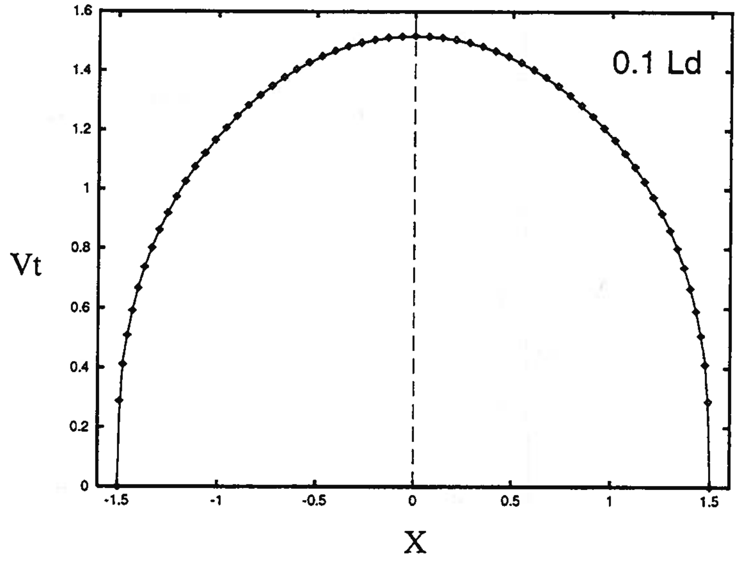

Figure 5.4: Tangential velocity on the surface of the Karman-Trefftz airfoil (entrance angle = 45°; desingularized distance at the leading and trailing edges = $0.1L_d$; points → exact solution; solid line → desingularized solution)

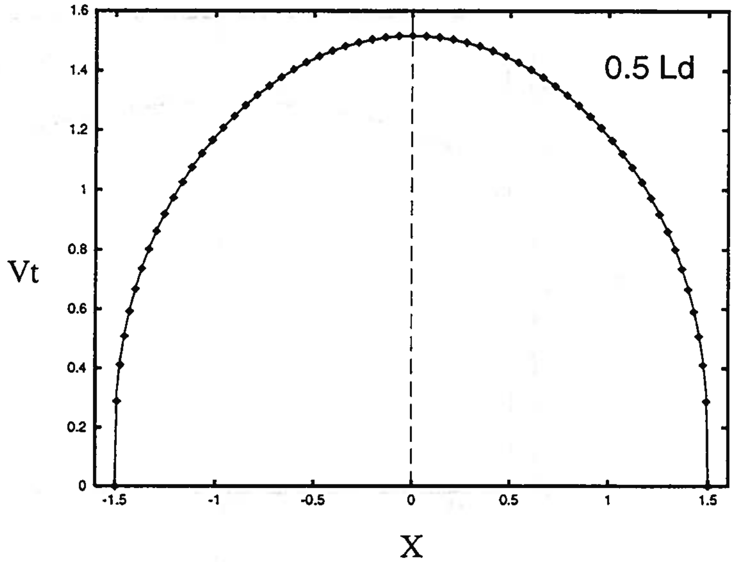

Figure 5.5: Tangential velocity on the surface of the Karman-Trefftz airfoil (entrance angle = 45°; desingularized distance at the leading and trailing edges = $0.5L_d$; points → exact solution; solid line → desingularized solution)

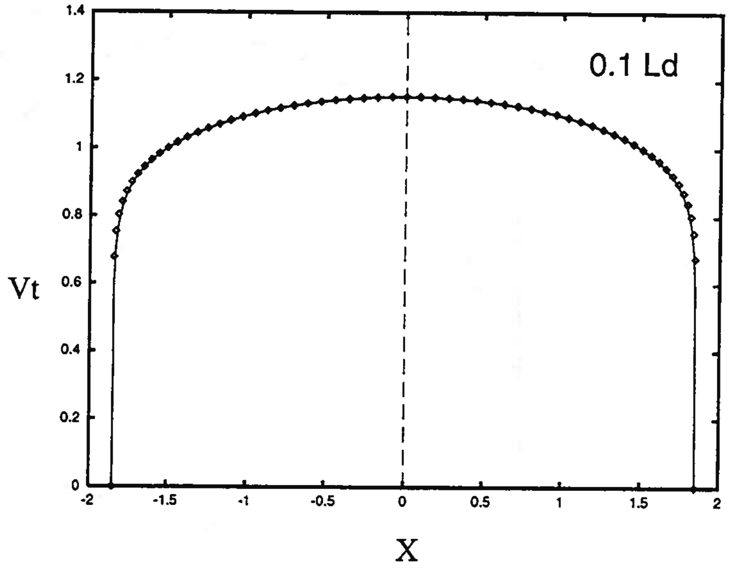

Figure 5.6: Tangential velocity on the surface of the Karman-Trefftz airfoil (entrance angle = 13.5°; desingularized distance at the leading and trailing edges = $0.1L_d$; points → exact solution; solid line → desingularized solution)

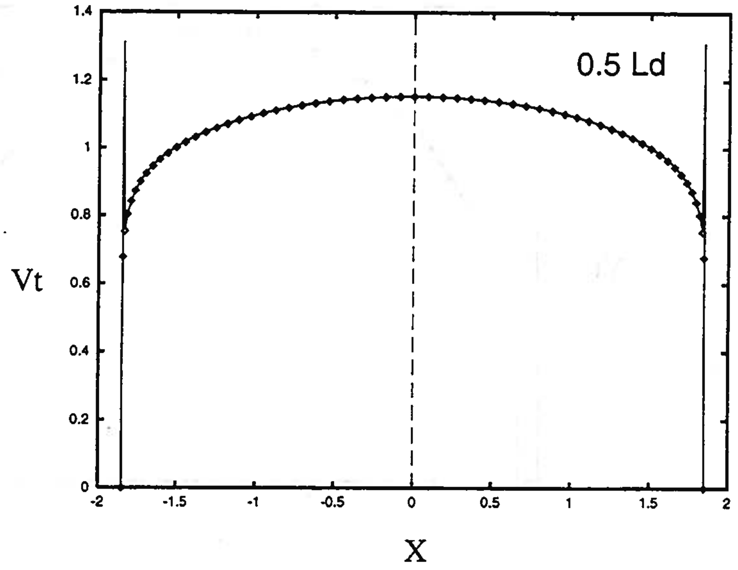

Figure 5.7: Tangential velocity on the surface of the Karman-Trefftz airfoil (entrance angle = 13.5°; desingularized distance at the leading and trailing edges = $0.5L_d$; points → exact solution; solid line → desingularized solution)

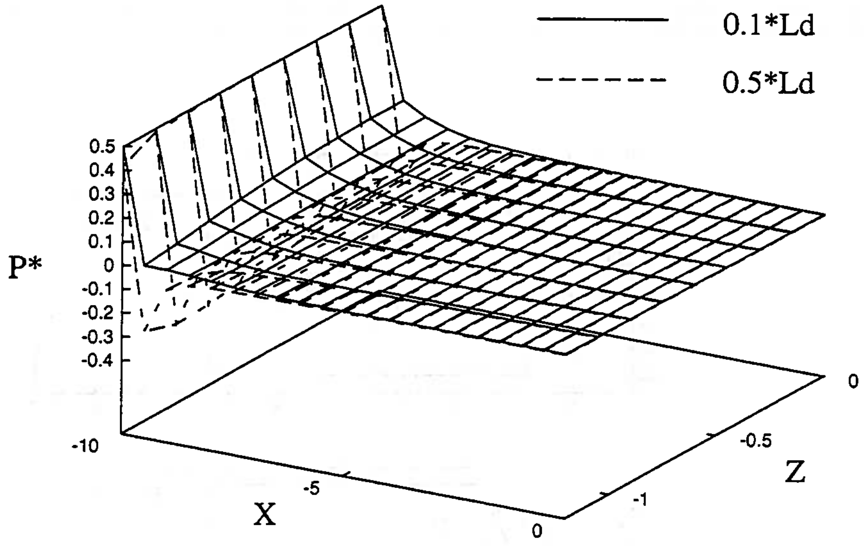

Figure 5.8: Wigley hull double body pressure coefficient on the forward half of the body (solid line → $0.1L_d$ desingularized distance at the stagnation points; dashed line → $0.5L_d$ desingularized distance at the stagnation points)

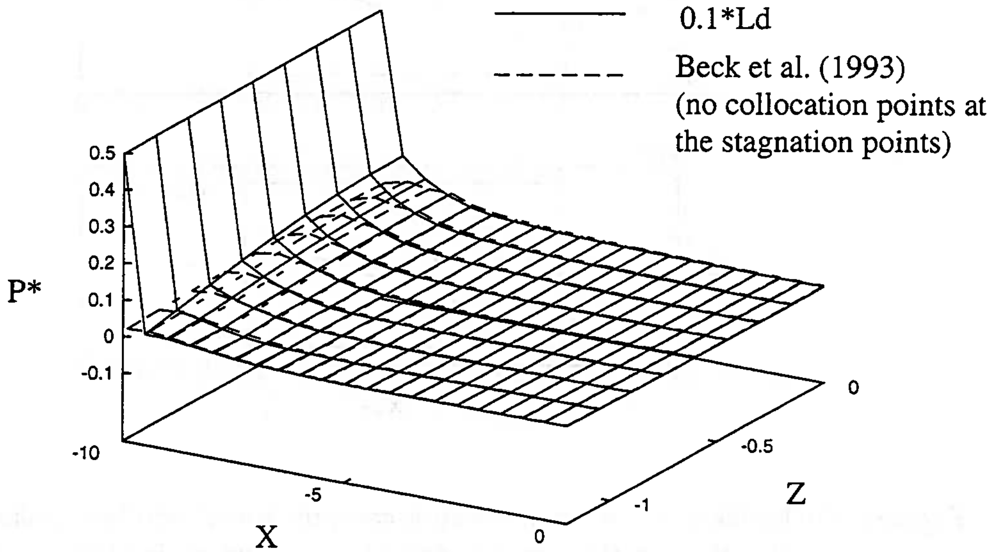

Figure 5.9: Wigley hull double body pressure coefficient on the forward half of the body (solid line → $0.1L_d$ desingularized distance at the stagnation points; dashed line → solution obtained using the discretization scheme of Beck *et al.* [2])

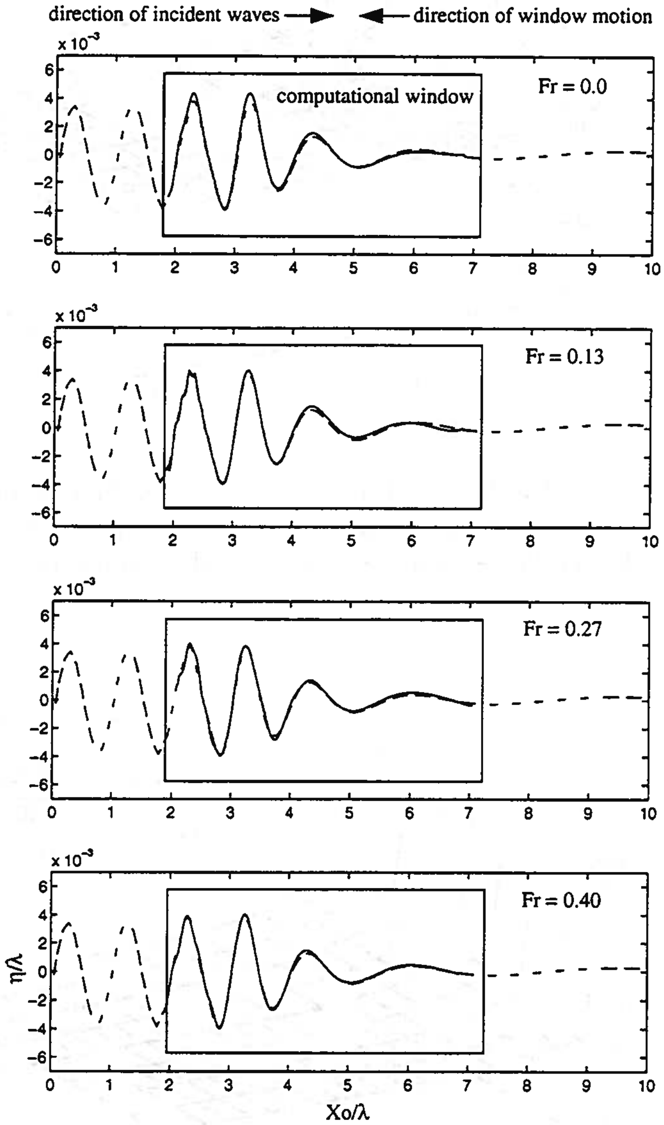

Figure 5.10: Incident waves in a moving computational window (solid line → wave elevations in the window; dashed line → wave elevations in the stationary tank)

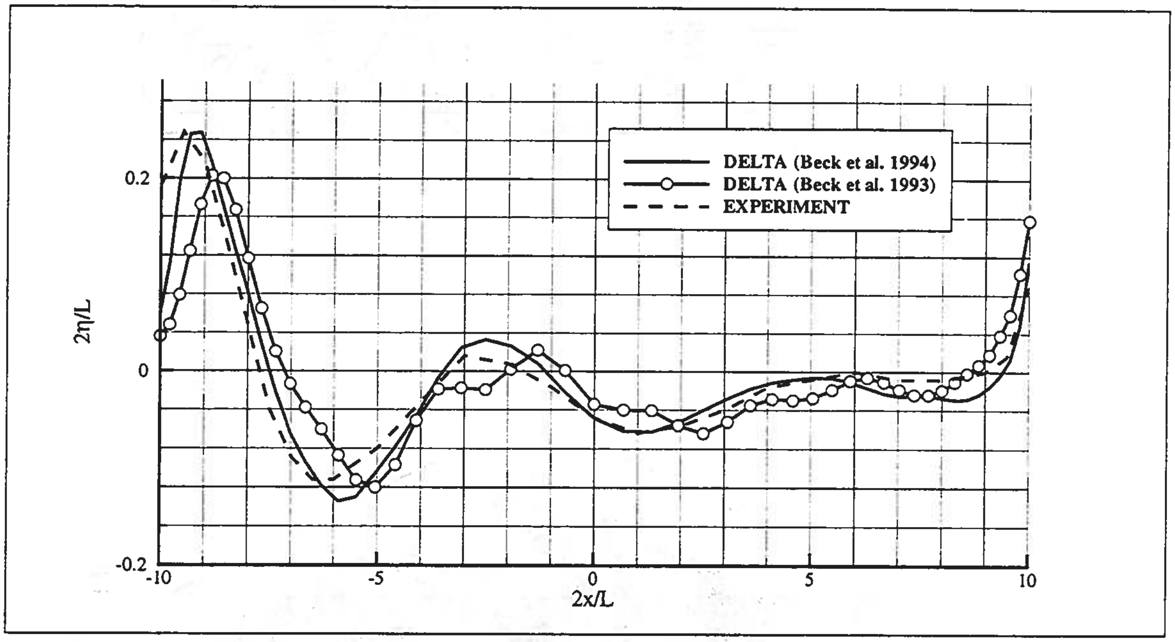

Figure 5.11: Wave profile along the standard Wigley hull at Fr=0.25, fixed to sinkage and trim. Experiments were conducted at the University of Tokyo on a 2.5m model fixed to sink and trim (cf. Noblesse and McCarthy [36])

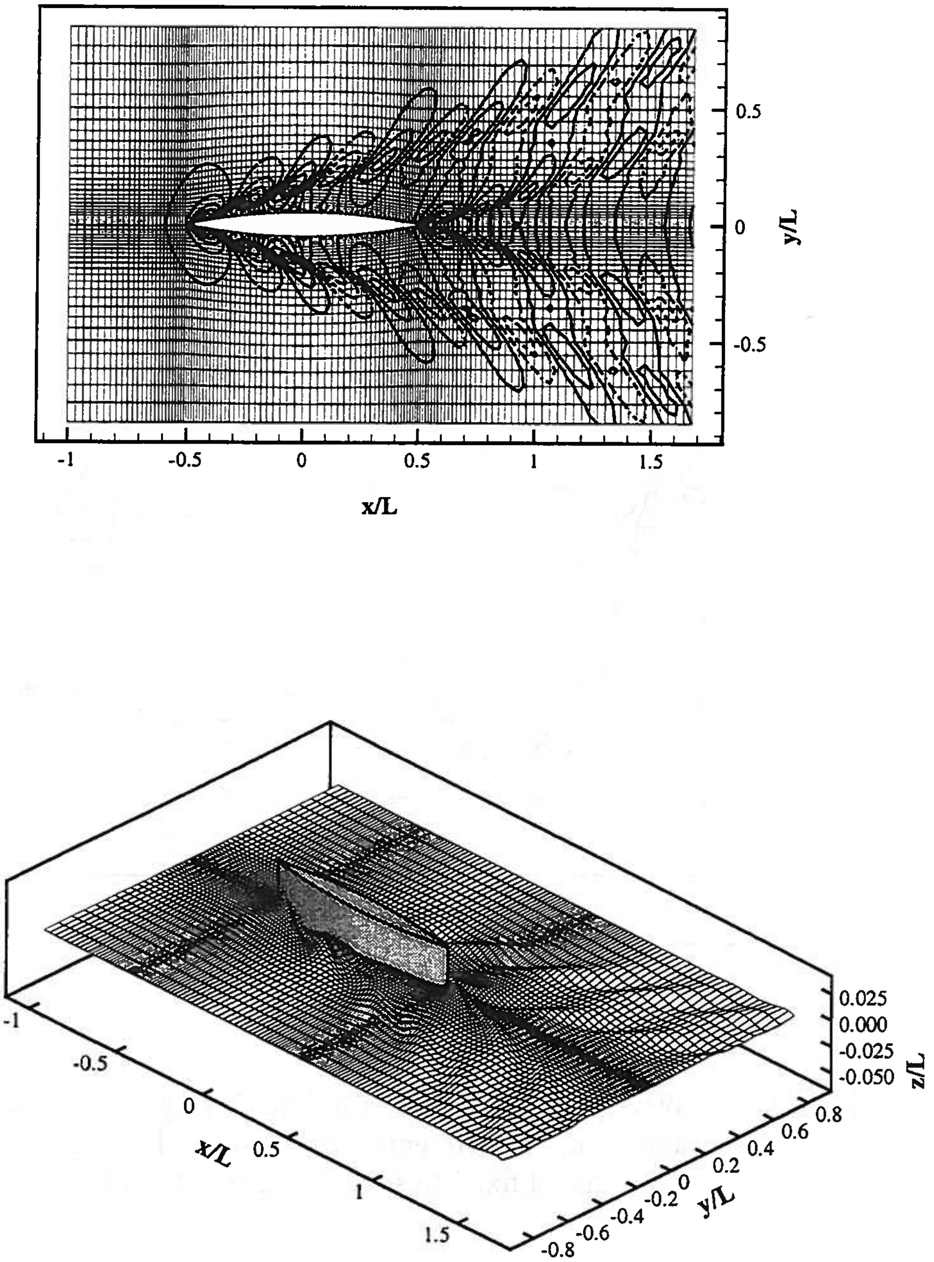

Figure 5.12: Free surface contours and isometric view of the standard Wigley hull advancing at Fr=0.25 through calm water. In the isometric view the z-axis is scaled by a factor of five. 3267 nodes are distributed on the free surface and 663 nodes on the body wetted surface.

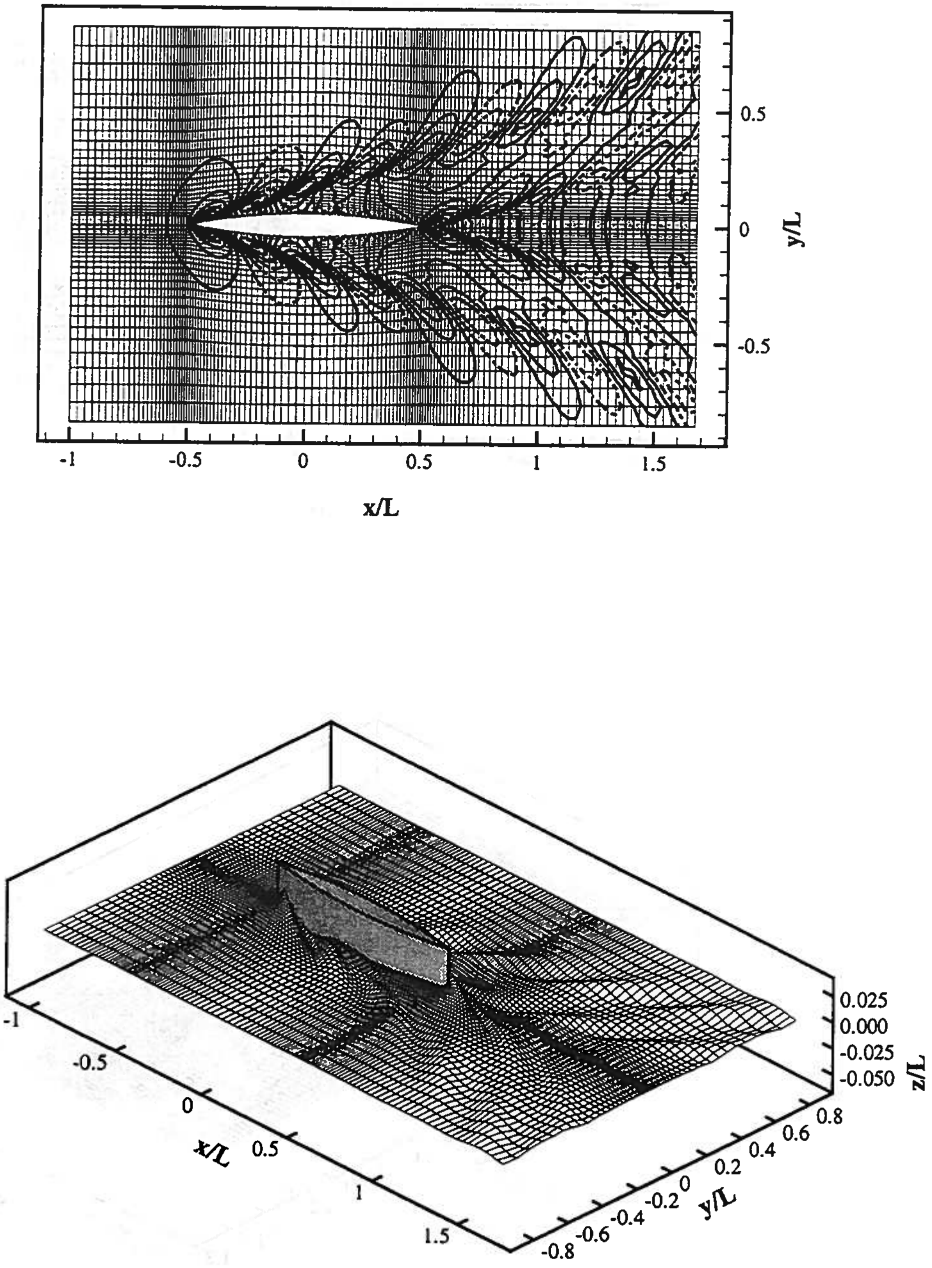

Figure 5.13: Free surface contours and isometric view of the standard Wigley hull advancing at Fr=0.27 through calm water. In the isometric view the z-axis is scaled by a factor of five. 3267 nodes are distributed on the free surface and 663 nodes on the body wetted surface.

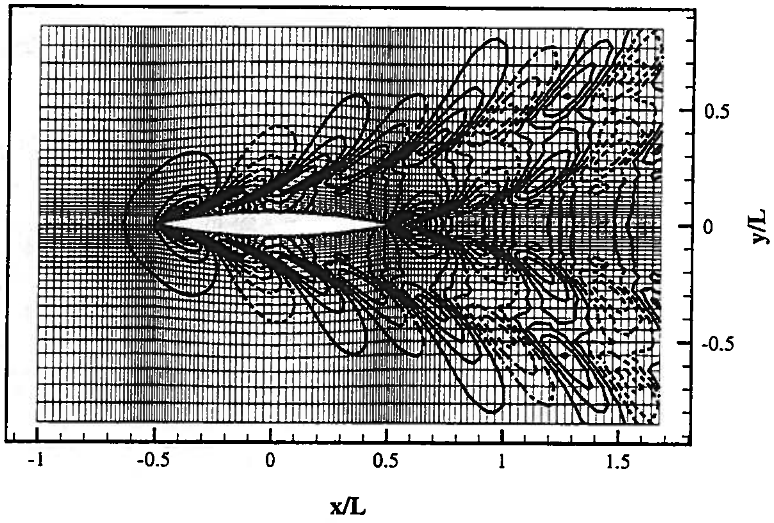

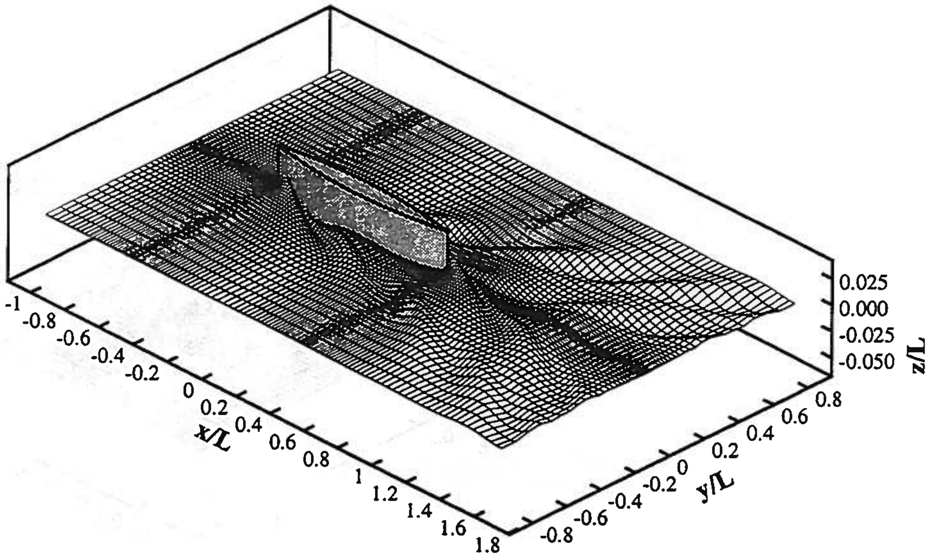

Figure 5.14: Free surface contours and isometric view of the standard Wigley hull advancing at Fr=0.30 through calm water. In the isometric view the z-axis is scaled by a factor of five. 3267 nodes are distributed on the free surface and 663 nodes on the body wetted surface.

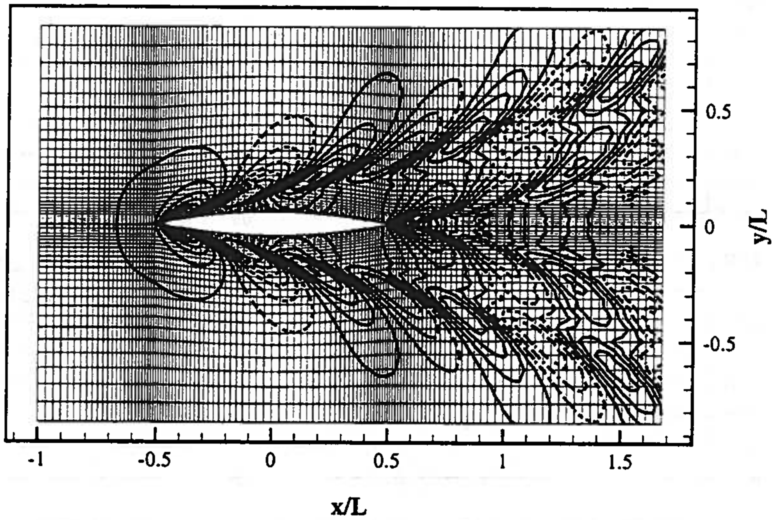

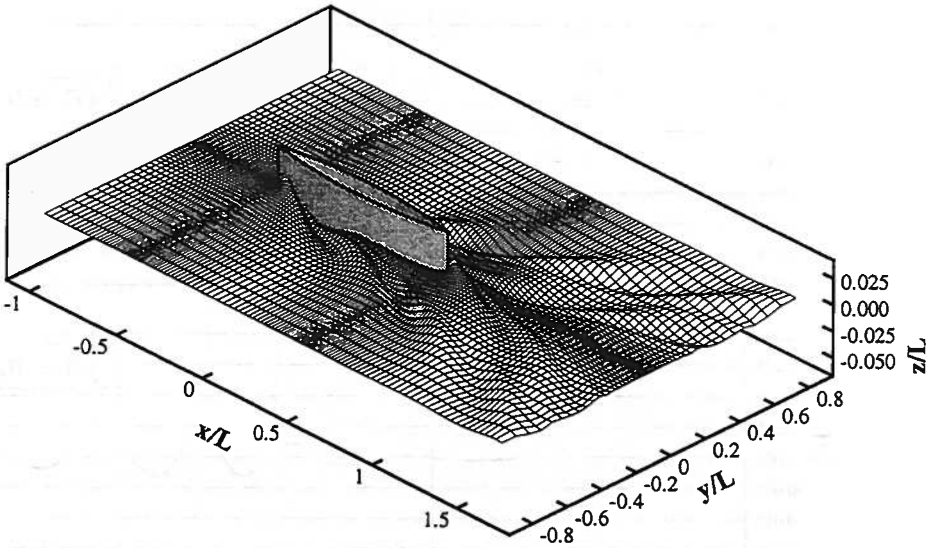

Figure 5.15: Free surface contours and isometric view of the standard Wigley hull advancing at Fr=0.32 through calm water. In the isometric view the z-axis is scaled by a factor of five. 3267 nodes are distributed on the free surface and 663 nodes on the body wetted surface.

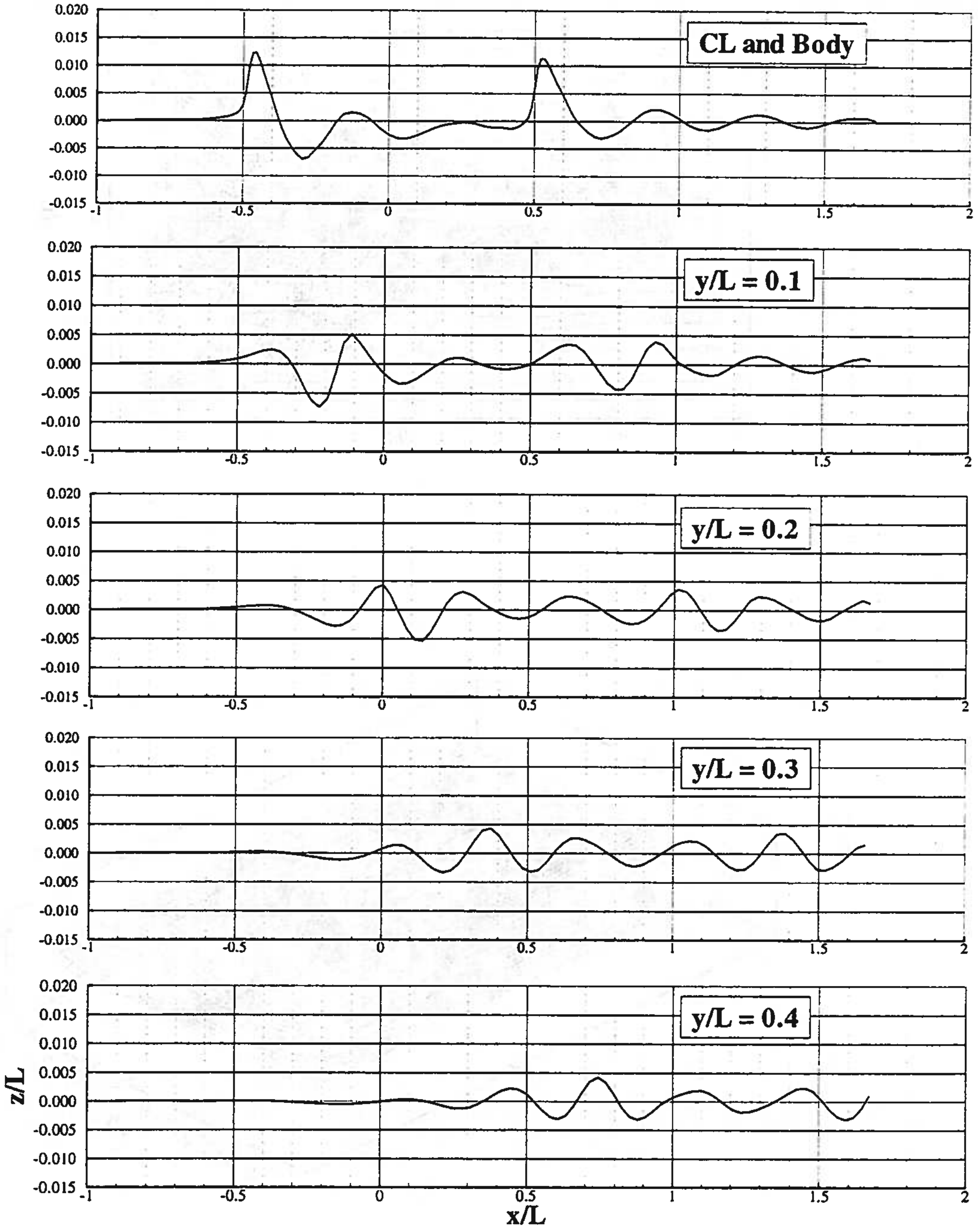

Figure 5.16: Free surface wave cuts for the standard Wigley hull advancing at Fr=0.25 through calm water. CL and Body → elevations are plotted for nodes on the centerline ($y/L = 0.0$) when $|x/L| > 0.5$ and for nodes next to the body when $|x/L| < 0.5$.

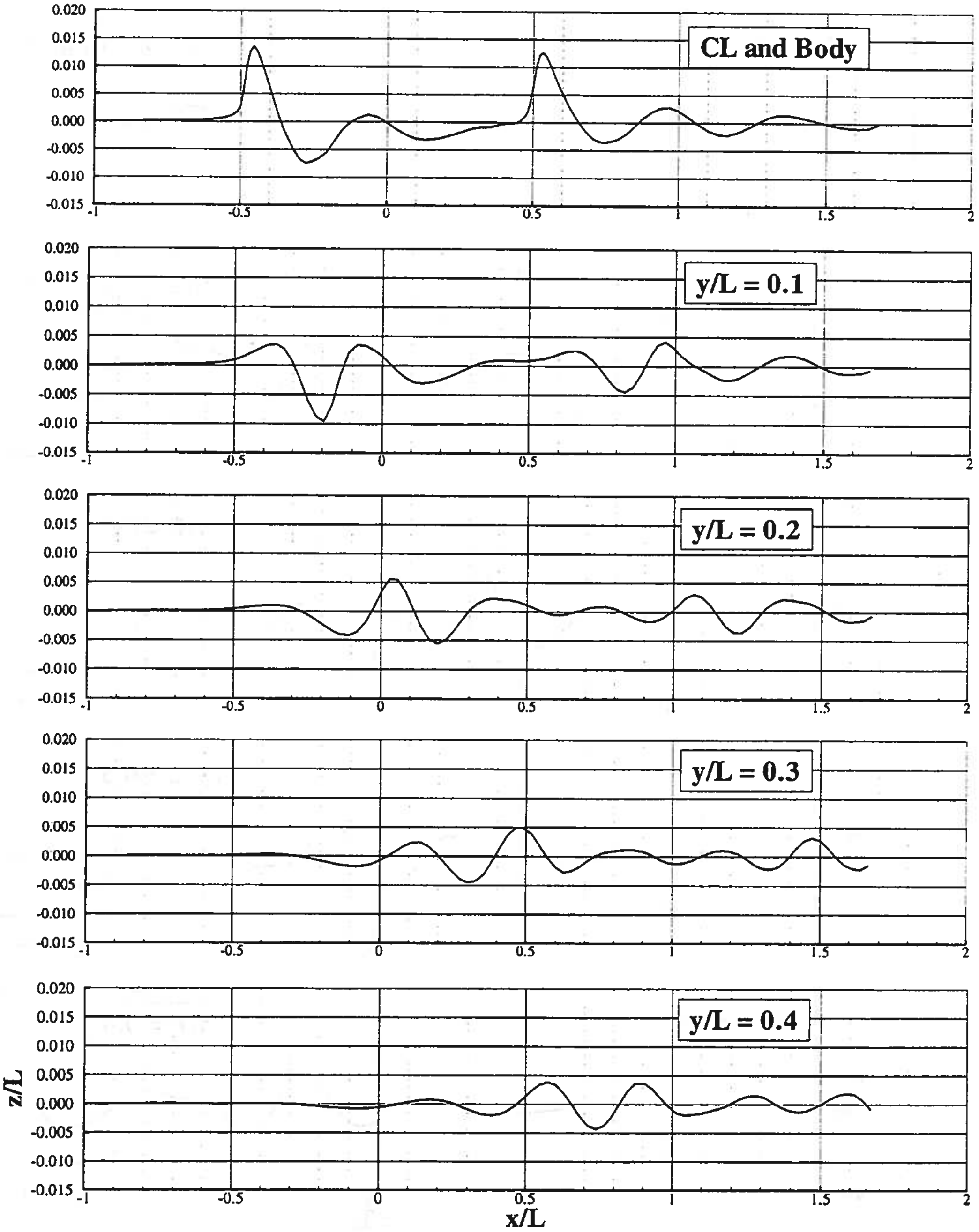

Figure 5.17: Free surface wave cuts for the standard Wigley hull advancing at Fr=0.27 through calm water. CL and Body → elevations are plotted for nodes on the centerline ($y/L = 0.0$) when $|x/L| > 0.5$ and for nodes next to the body when $|x/L| < 0.5$.

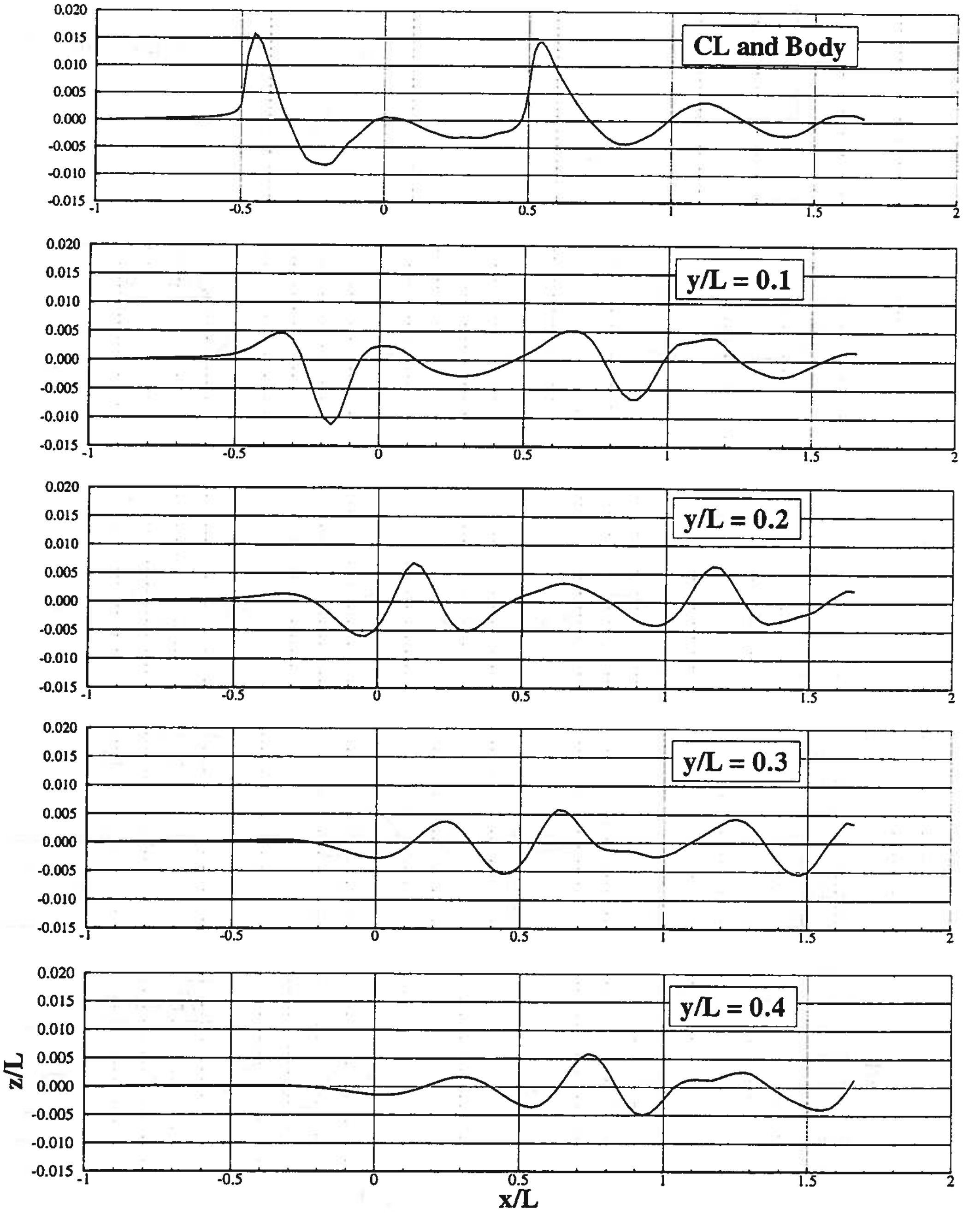

Figure 5.18: Free surface wave cuts for the standard Wigley hull advancing at Fr=0.30 through calm water. CL and Body → elevations are plotted for nodes on the centerline ($y/L = 0.0$) when $|x/L| > 0.5$ and for nodes next to the body when $|x/L| < 0.5$.

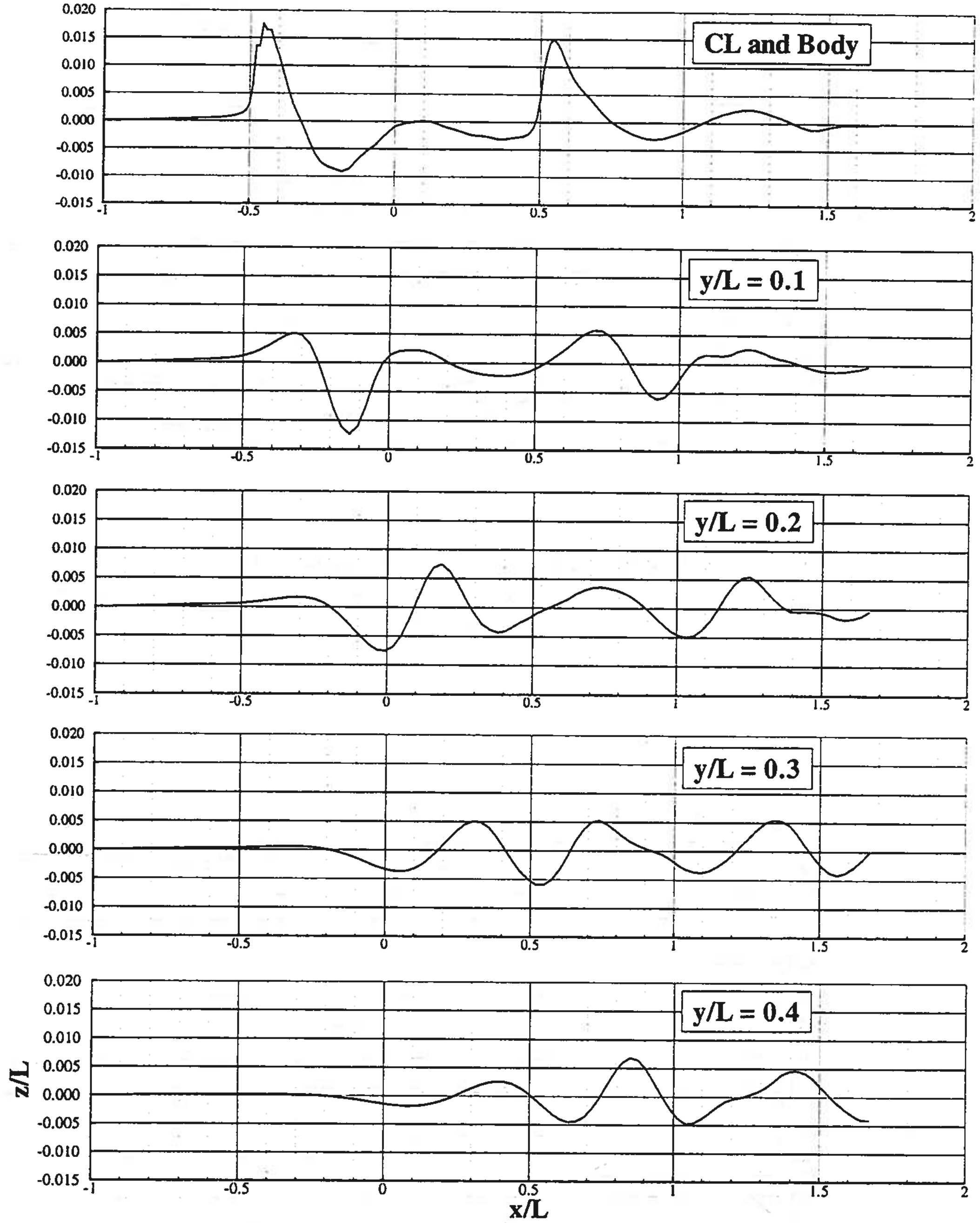

Figure 5.19: Free surface wave cuts for the standard Wigley hull advancing at Fr=0.32 through calm water. CL and Body → elevations are plotted for nodes on the centerline ($y/L = 0.0$) when $|x/L| > 0.5$ and for nodes next to the body when $|x/L| < 0.5$.

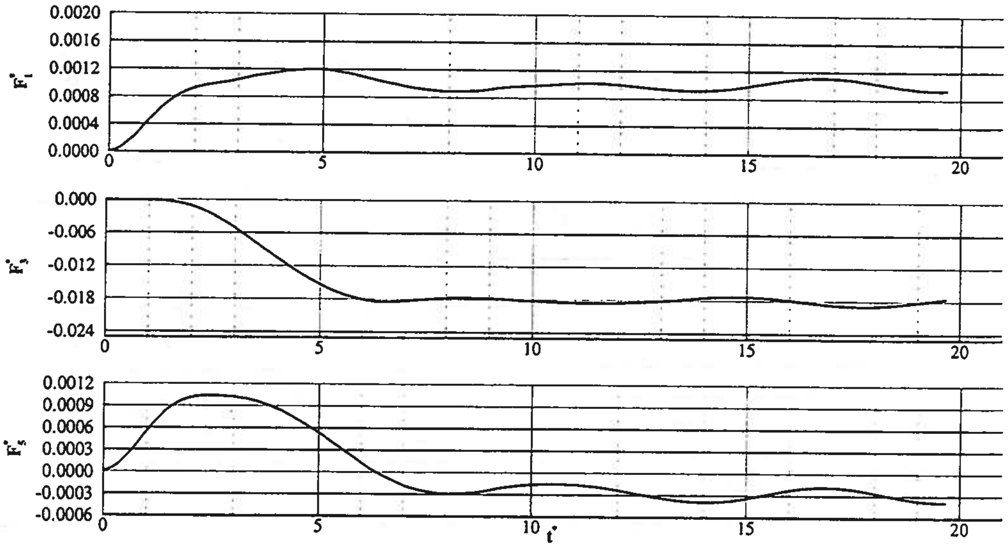

Figure 5.20: Nondimensional surge (F_1^*) and heave (F_3^*) forces and pitch (F_m^*) moment for the standard Wigley hull advancing at Fr=0.25 through calm water. $F^* = F/(\frac{1}{2}\rho U_o^2 S)$, $t^* = t\sqrt{\frac{g}{L}}$.

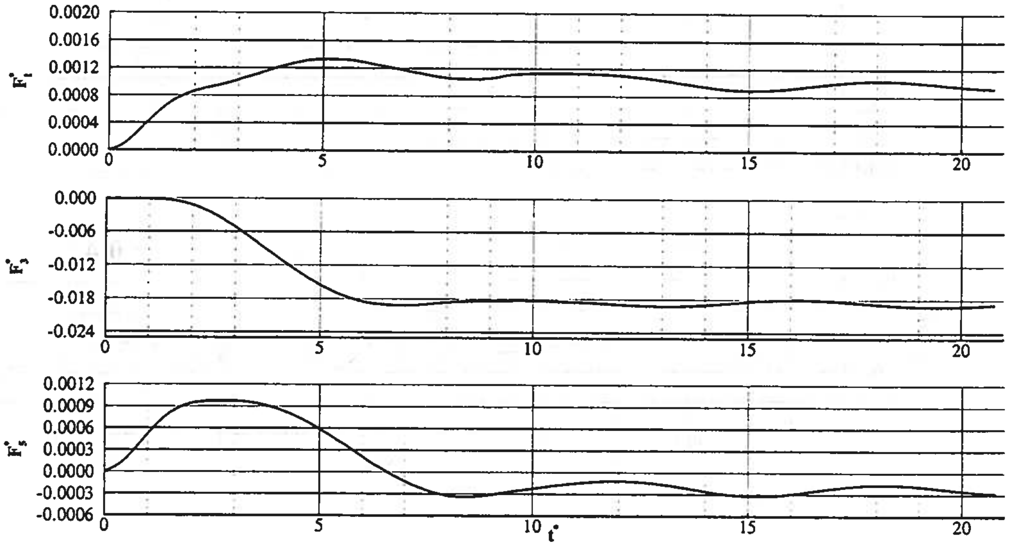

Figure 5.21: Nondimensional surge (F_1^*) and heave (F_3^*) forces and pitch (F_m^*) moment for the standard Wigley hull advancing at Fr=0.27 through calm water. $F^* = F/(\frac{1}{2}\rho U_o^2 S)$, $t^* = t\sqrt{\frac{g}{L}}$.

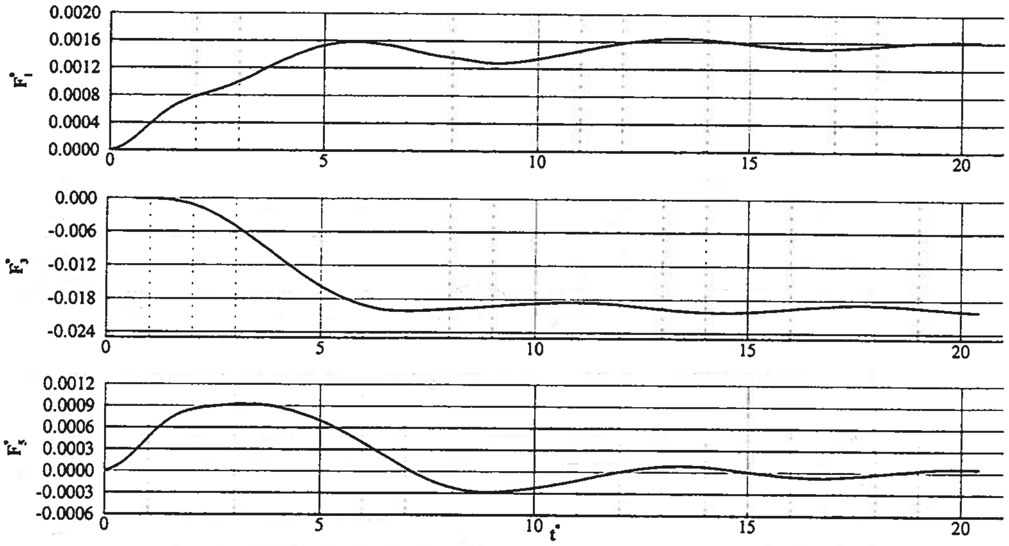

Figure 5.22: Nondimensional surge (F_1^*) and heave (F_3^*) forces and pitch (F_m^*) moment for the standard Wigley hull advancing at Fr=0.30 through calm water. $F^* = F/(\frac{1}{2}\rho U_o^2 S)$, $t^* = t\sqrt{\frac{g}{L}}$.

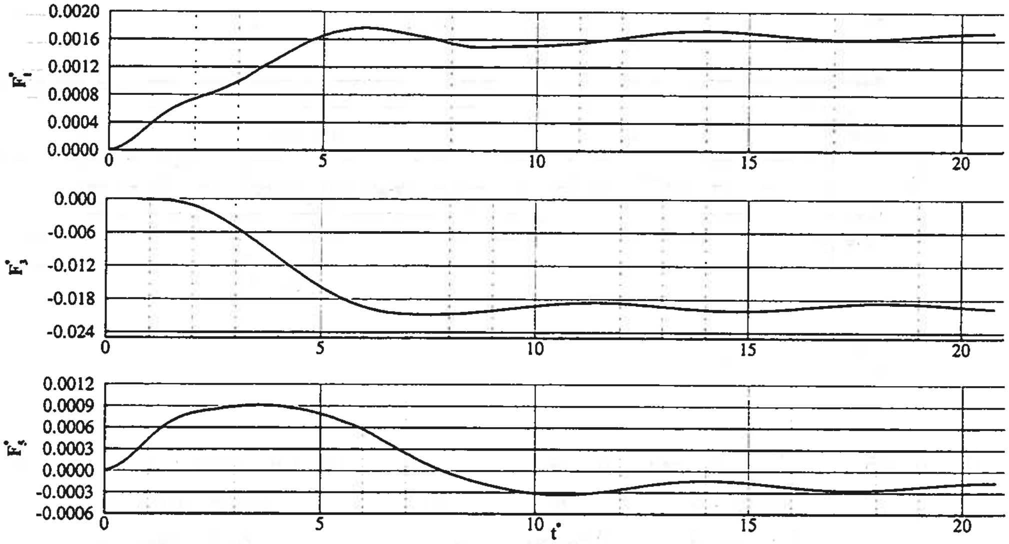

Figure 5.23: Nondimensional surge (F_1^*) and heave (F_3^*) forces and pitch (F_m^*) moment for the standard Wigley hull advancing at Fr=0.32 through calm water. $F^* = F/(\frac{1}{2}\rho U_o^2 S)$, $t^* = t\sqrt{\frac{g}{L}}$.

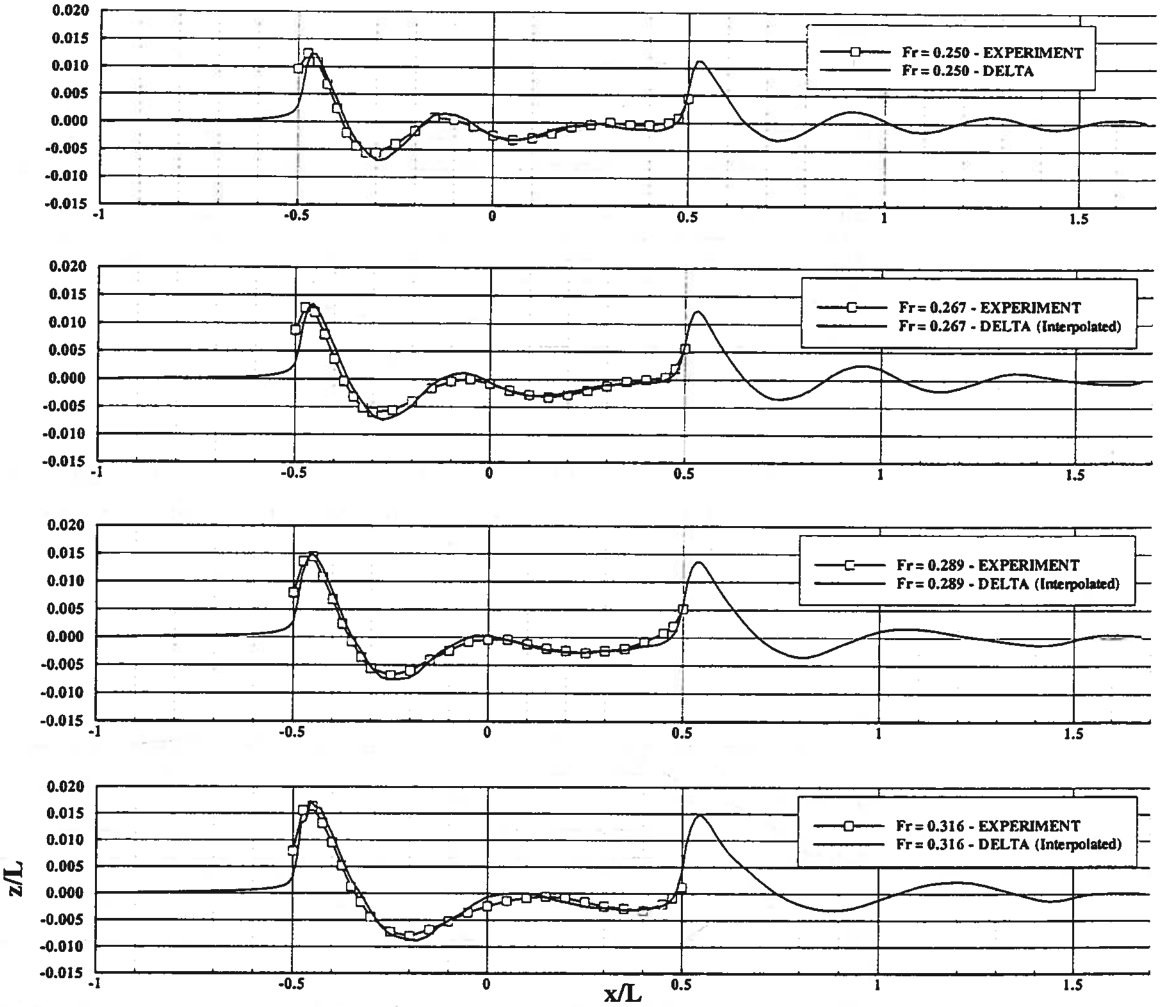

Figure 5.24: Comparison between computations and experimental measurements for the wave elevation along the body. Experiments were conducted at the University of Tokyo on a 2.5 meter model fixed to sink and trim (cf. Noblesse and McCarthy [36]

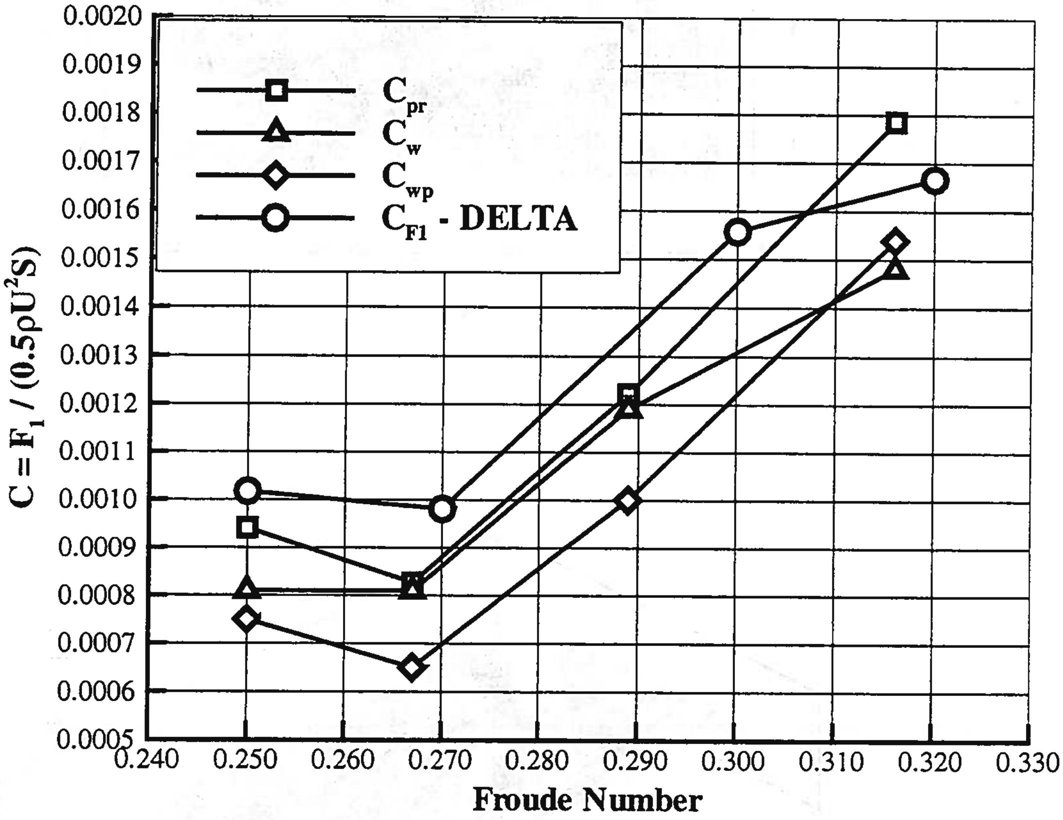

Figure 5.25: Comparison of the wave resistance coefficient versus Froude number. Experiments were conducted at the University of Tokyo on a 2.5 meter model fixed to sink and trim (cf. Noblesse and McCarthy [36]). C_{pr}, C_w, and C_{wp} are the experimental results obtained by pressure integration over the hull wetted surface (C_{pr}), residual resistance from the resistance test (C_w), and wave pattern analysis (C_{wp}). C_{F1} is the computed force using the DELTA method.

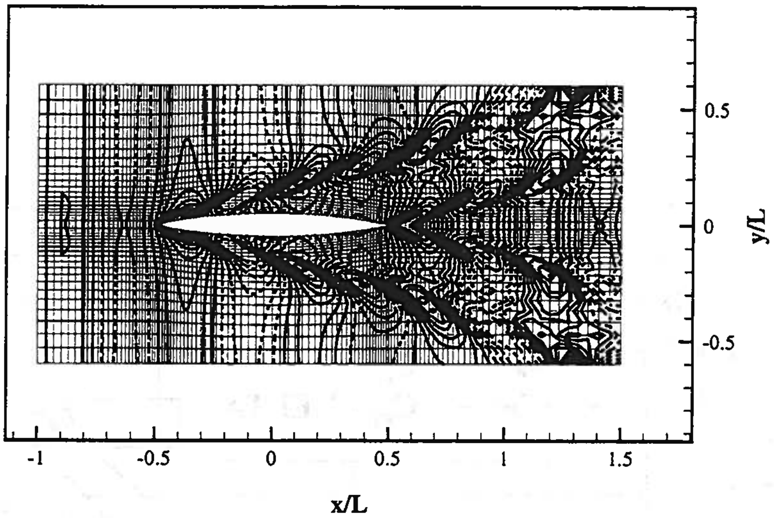

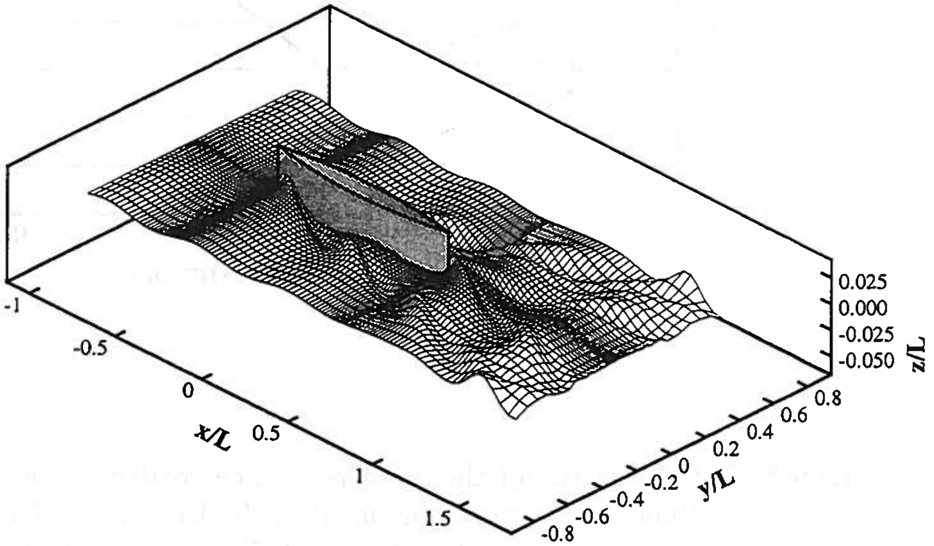

Figure 5.26: Free surface contours and isometric view of the modified Wigley hull III advancing at Fr=0.30 through incident waves. In the isometric view the z-axis is scaled by a factor of five. The incident waves have length, $\lambda/L = 0.5$ and steepness, $H/\lambda = 1/111$.

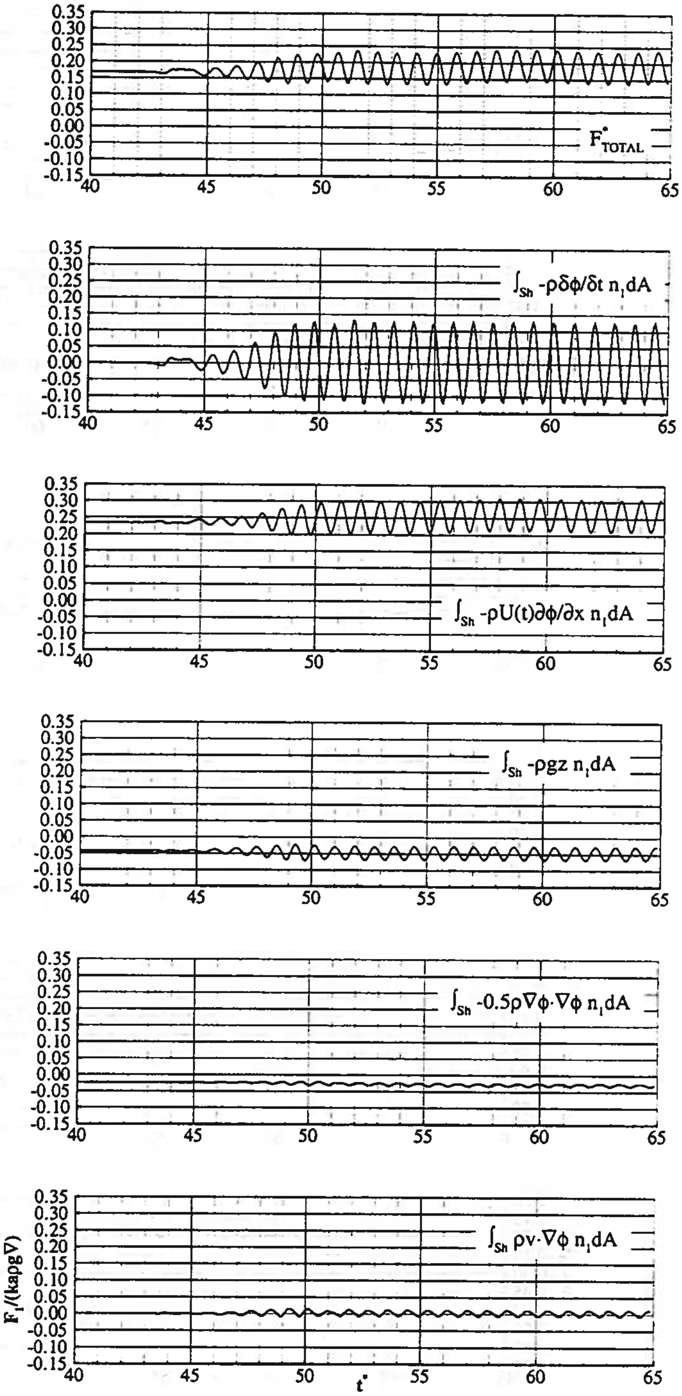

Figure 5.27: Surge exciting force components on the modified Wigley hull III. The component forces are computed by integrating each term in the pressure equation over the body wetted surface. F^*_{TOTAL} is the sum of the components. Fr=0.30, $\lambda/L = 0.5$, $H/\lambda = 1/111$.

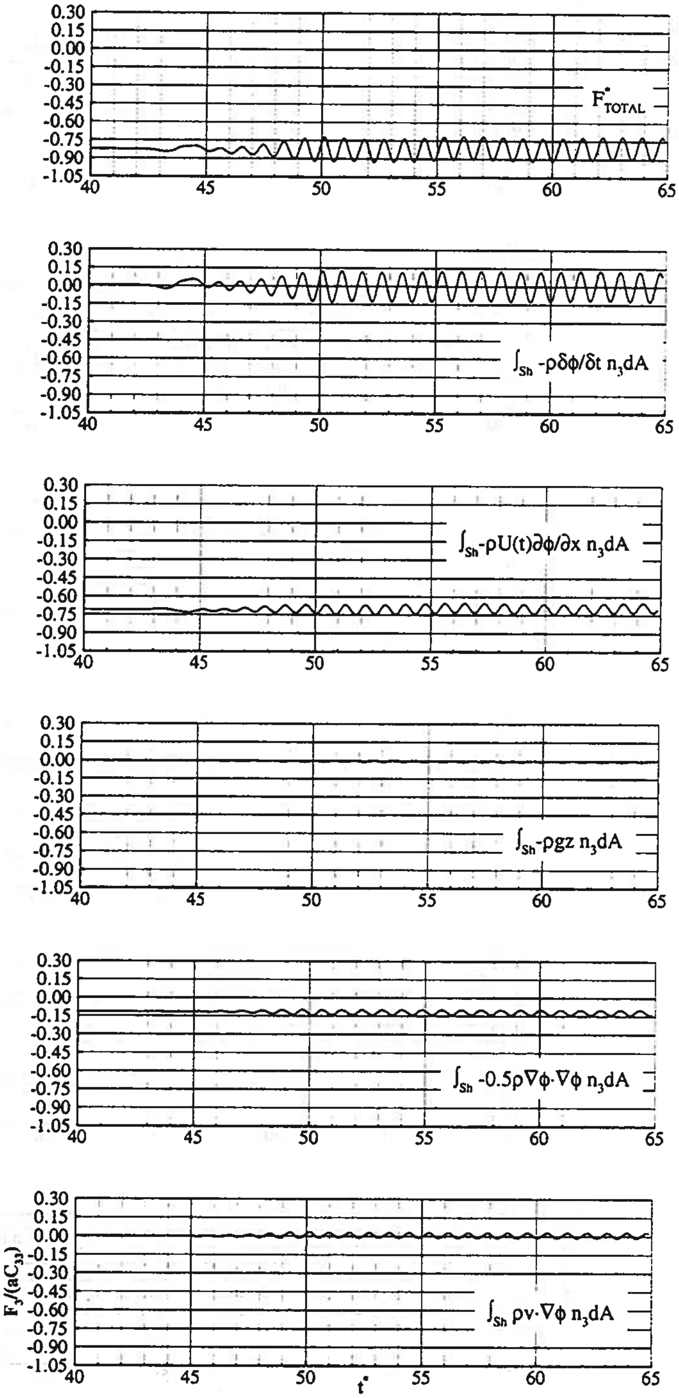

Figure 5.28: Heave exciting force components on the modified Wigley hull III. The component forces are computed by integrating each term in the pressure equation over the body wetted surface. F^*_{TOTAL} is the sum of the components. Fr=0.30, $\lambda/L = 0.5$, $H/\lambda = 1/111$.

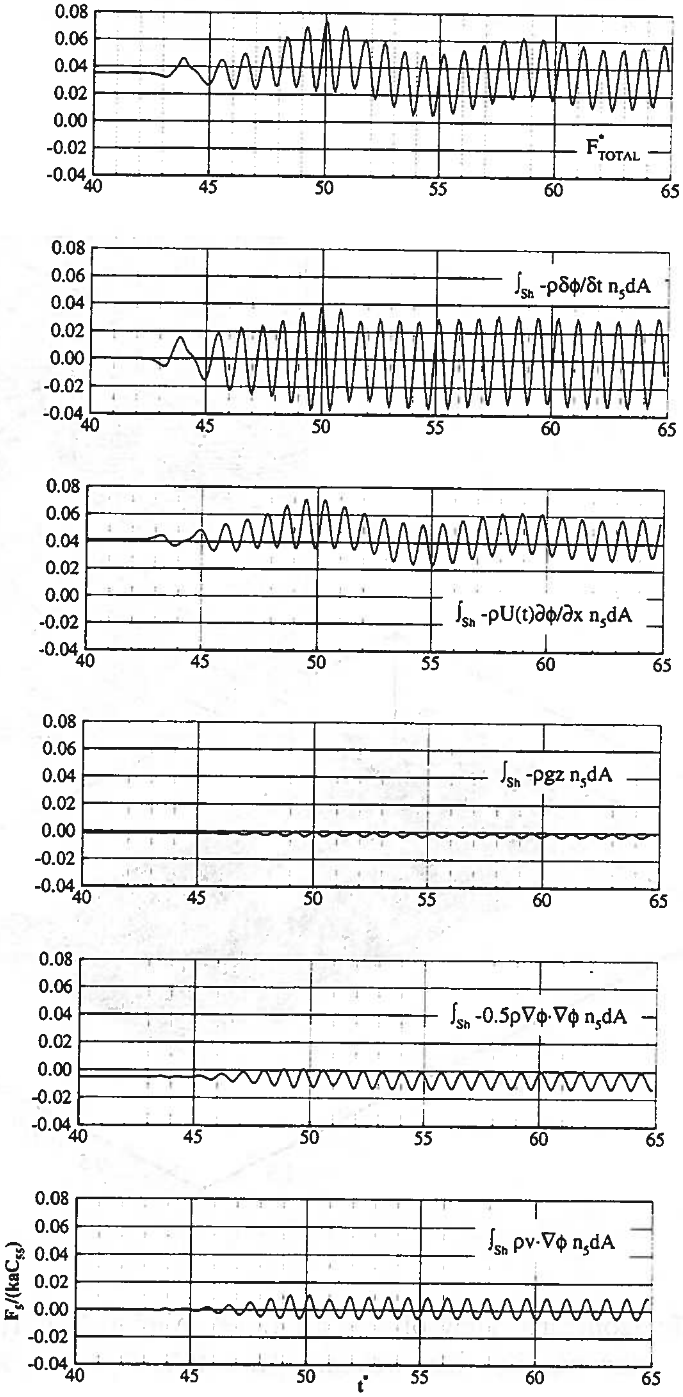

Figure 5.29: Pitch exciting moment components on the modified Wigley hull III. The component forces are computed by integrating each term in the pressure equation over the body wetted surface. F^*_{TOTAL} is the sum of the components. Fr=0.30, $\lambda/L = 0.5$, $H/\lambda = 1/111$.

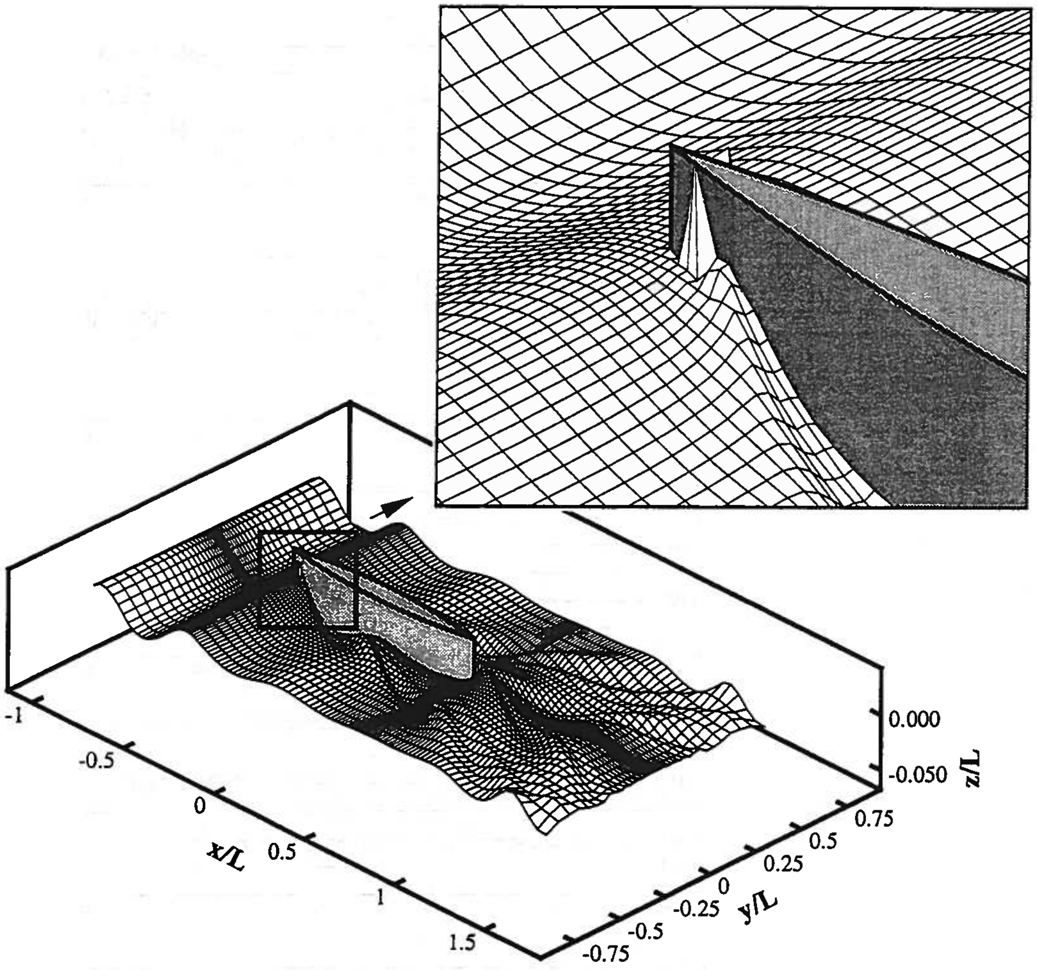

Figure 5.30: Isometric view of the modified Wigley hull III advancing at Fr=0.30 through incident waves. $\lambda/L = 0.5$, $H/\lambda = 1/20$.

CHAPTER VI

TWO-DIMENSIONAL INVISCID TRANSOM STERN FLOW

6.1 Introduction

Two-dimensional fully nonlinear transom stern flow is investigated using the DELTA method. The flow is unsteady in that the problem is started from rest and accelerated to steady forward speed. The purpose of this study is to compare the unsteady results with previous steady calculations and to provide a starting point for extending to unsteady fully nonlinear three-dimensional transom stern flows.

The cases studied herein correspond to those in Vanden-Broeck and Tuck [44] and Vanden-Broeck [43]. They compute nonlinear waves behind a transom stern using a series expansion in the Froude number. The problem is solved in an inverse manner using the x and y coordinates as the dependent variables and the velocity potential and stream function ϕ and ψ as the independent variables. The series expansions in x and y are everywhere divergent but can be summed by standard methods. Integro-differential equations with nonlinear boundary conditions are solved in the inverse space to obtain the expansion coefficients.

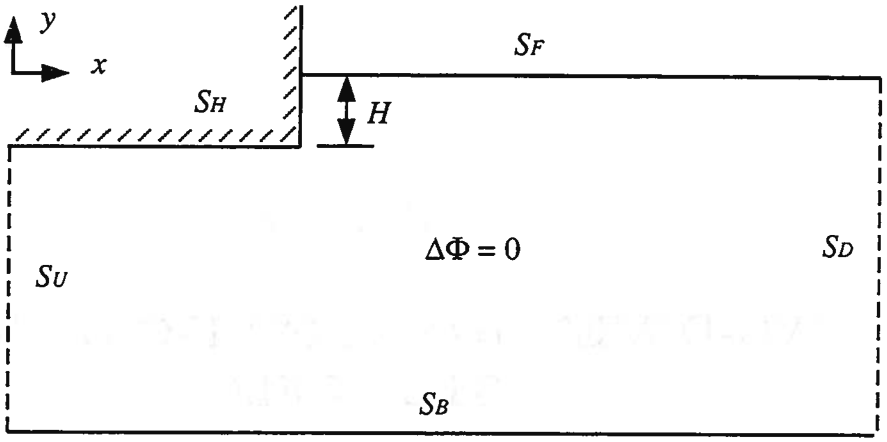

Figure 6.1: Problem configuration

Problem Formulation

Figure 6.1 shows the problem configuration. The $x - y$ coordinate system is translating with speed U_b in the negative x direction. Laplace's equation governs in the fluid domain and the velocity potential is $\Phi = U_b x + \phi$. The surfaces bounding the fluid are:

S_F = Free Surface

S_H = Body Surface

S_U = Upstream Truncation Surface

S_D = Downstream Truncation Surface

S_B = Bottom Surface.

The boundary conditions are

$$\left.\begin{aligned} \frac{D\eta}{Dt} &= \frac{\partial\phi}{\partial z} \\ \frac{D\phi}{Dt} &= -g\eta + \frac{1}{2}|\nabla\phi|^2 \end{aligned}\right\} \qquad \vec{x} \in S_F \tag{6.1}$$

$$\frac{\partial\phi}{\partial n} = -U_b n_1 \qquad \vec{x} \in S_H \tag{6.2}$$

$$\nabla\phi \to 0 \quad \text{as} \quad y \to -\infty \qquad \vec{x} \in S_B. \tag{6.3}$$

Here, $\frac{D}{Dt} = \frac{\partial}{\partial t} + \nabla\Phi \cdot \nabla$ is the material or Lagrangian derivative, $\vec{n} = (n_1, n_2, n_3)$ is the unit normal on the body pointing out of the fluid, g is the acceleration of gravity, η is the free surface elevation, and ϕ is the perturbation potential. The boundaries S_U and S_D are unspecified. We have run cases with S_U and S_D prescribed to satisfy continuity and saw very little difference in the results as long as S_U and S_D are far enough up and downstream respectively. We placed the truncation boundaries about twelve wavelengths away from the transom for these calculations.

6.2 Results

Vanden-Broeck [43] suggested that two realistic solutions exist for the steady flow behind a transom stern. For small values of the Froude number, the flow rises up the transom to a stagnation point. The free surface separates from the transom at the stagnation point creating waves downstream that increase in steepness with increasing Froude number. Call this solution A. This solution is physically unreasonable for large values of Froude number because the ratio of stagnation height to transom depth goes to infinity as the Froude number goes to infinity. For large Froude numbers a second, more physically realizable solution exists where the flow separates cleanly from the bottom of the transom. Call this solution B. This solution reduces to the uniform stream as Froude number tends to infinity and the downstream waves steepen as Froude number becomes small. In fact, Vanden-Broeck found a minimum Froude number ($= 2.26$) below which the downstream waves exceed the theoretical breaking wave steepness limit ($2A/\lambda = 0.141$).

The problem is started from rest and the hull is accelerated up to steady forward speed. Using the DELTA method, the inviscid solution *always tends towards config-*

uration A as the hull reaches steady forward speed, regardless of the Froude number. In a viscous fluid, we know that the flow behaves like solution B for high Froude numbers. As the hull speed increases from rest, the flow separating from the bottom of the transom becomes turbulent, resulting in the "dead water" region commonly observed behind transom sterns. Consequently the pressure behind the transom is lowered. Eventually the falling pressure causes the free surface to drop to the bottom of the transom resulting in the solution B flow. Once the free surface separates cleanly from the transom, the turbulence is confined to the thin boundary layer (for high speeds) and the viscous wake. Using an inviscid flow model, it appears to be impossible to proceed from transom wetted to transom dry. However, we did find two techniques resulting in solution B.

The first method started the problem at steady forward speed with the transom out of the water. The hull is then lowered slowly into the water. As the hull is lowered, the free surface remains separated from the bottom of the transom and solution B results. This technique will not work for a problem starting from rest with the transom immersed. To obtain solution B for the problem starting from rest we tried a second technique attempting to mimic the effect of the dead water region by artificially lowering the stagnation pressure on the transom. This pressure drop can be modeled in the inviscid flow code by modifying the boundary condition on the transom. The condition,

$$\frac{\partial \phi}{\partial n} = -U_b n_1 \tag{6.4}$$

causes the stagnation pressure. We reduce the stagnation pressure by modifying the transom boundary condition to:

$$\frac{\partial \phi}{\partial n} = -U_b n_1 \left(2e^{-\beta t^2} - 1\right) \tag{6.5}$$

As the hull accelerates up to speed, the pressure on the transom drops until the free surface drops to the bottom of the transom. When the hull reaches steady speed, solution B is recovered.

The general numerical details are similar to those outlined in chapter II. There is a double node where the free surface meets the transom in the solution A flow. One node satisfies the body boundary condition while the other satisfies the free surface boundary condition. Treating the intersection in this manner has consistently worked well in the desingularized method. There is one additional constraint (or Kutta condition) at the bottom of the transom in the solution B flow. The free surface nodes move downstream with the fluid velocity during the intermediate time steps (fourth order Runge-Kutta). At the end of a major time step the free surface nodes are regridded to their original positions by interpolating elevations and potentials. The Kutta condition is imposed by regridding the first free surface node back to the bottom of the transom. The potential at this point is computed from the source strengths.

Figure 6.2 indicates the convergence of the method for solutions A and B at Froude number based on transom depth of $F_H = U_b/\sqrt{gH} = 6.3$. 200 nodes were distributed on the body surface. Free surface profiles were computed for 20, 30, and 40 nodes per wavelength (λ) of the downstream waves. The figure shows that the wave profiles have converged to graphical accuracy.

Figure 6.3 indicates the convergence as the number of nodes on the body is increased while the number of nodes on the free surface remains fixed at 30 nodes per wavelength. The results for 300 and 500 nodes on the body agree to graphical ac-

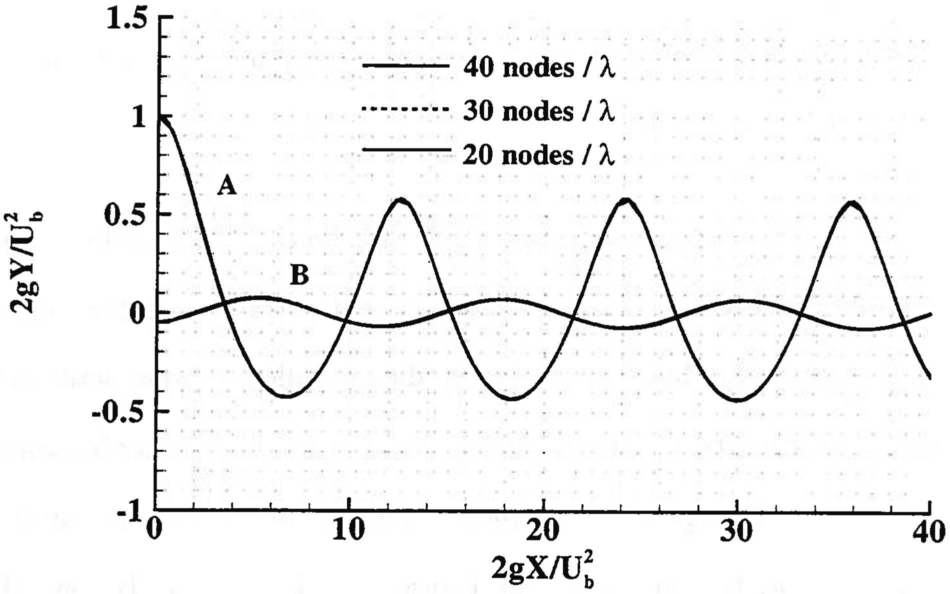

Figure 6.2: Convergence of solutions A and B for $F_H = 6.3$. Results are shown for 20, 30, and 40 nodes per wavelength (λ) of the downstream waves.

curacy for solution A. Solution B was computed for 200 and 300 nodes only and the results agree to graphical accuracy. More nodes are required on the body in solution A probably to resolve the corner flow at the bottom of the transom.

Figure 6.4 shows the waves generated by the transom stern at $F_H = 6.3$. The fully nonlinear solution starting from rest is compared with Vanden-Broeck's 1980 fully nonlinear steady results. Both steady state solutions A and B are compared. The solutions agree quite well except there is a noticeable difference in wavelength for solution A.

Table 6.1 shows downstream wave characteristics for the Vanden-Broeck [43] and DELTA solution A. Here, $a^* = a2g/U_b^2$ is the nondimensional wave amplitude found by subtracting the minimum wave elevation from the maximum and dividing by

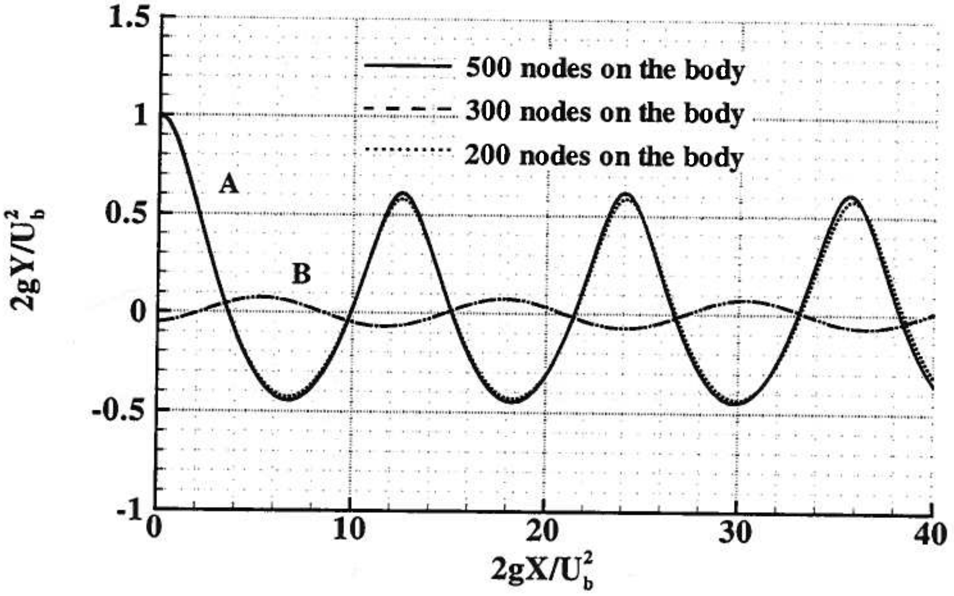

Figure 6.3: Convergence of solutions A and B for $F_H = 6.3$. Results are shown for 200, 300, and 500 nodes on the body for solution A and 200 and 300 nodes on the body for solution B.

	a^*	λ^*	$2a^*/\lambda^*$	λ_0^*	λ_4^*
Vanden-Broeck	0.51	12.1	0.084	12.6	11.6
DELTA	0.53	11.6	0.091	12.6	11.5

Table 6.1: Comparison of downstream wave characteristics for solution A.

two for the downstream waves. $\lambda^* = \lambda 2g/U_b^2$ is the nondimensional wavelength found by measuring the distance between zero crossings for the downstream waves. Since the phase speed of the waves equals U_b, we can use the deep water dispersion relation to estimate the wavelength. The linear wavelength is $\lambda_0^* = \lambda_0 2g/U_b^2 = 4\pi = 12.6$. Using the 5th order dispersion relation for deep water Stokes waves ($U_b^2 = \frac{g}{k}(1 + (ka)^2 + 5/4(ka)^4)$) and the computed wave amplitude (a) we can solve for the wave number (k) and get an estimate for the nonlinear wavelength ($\lambda_4^* = \lambda_4 2g/U_b^2$). The wavelength, $\lambda^* = 11.6$, measured from the DELTA solution agrees

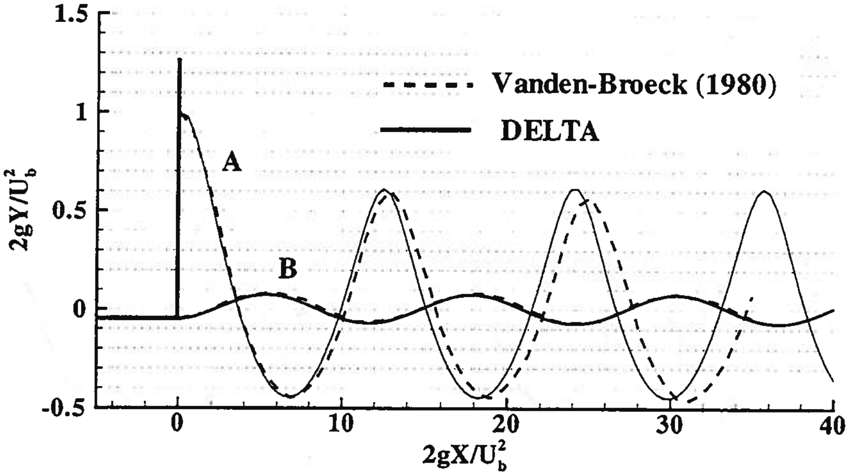

Figure 6.4: Solutions A and B at $F_H = 6.3$

with the wavelength, $\lambda_4^* = 11.5$, predicted by the 5th order dispersion relation while the wavelength, $\lambda^* = 12.1$, measured from Vanden-Broeck's solution is greater than the wavelength, $\lambda_4^* = 11.6$, predicted by the 5th order dispersion relation.

Figure 6.5 shows wave steepness versus Froude number for the waves downstream of the transom. The lines on the graph represent the relationship between wave steepness and Froude number derived by Vanden-Broeck [43]. The Froude number can be related to the mean potential and mean kinetic energy in the wave train by integrating the momentum equation. The mean potential and kinetic energy are in turn functions of the wave steepness. The points represent results from the DELTA method for various Froude numbers. Excellent agreement with the theoretical wave steepness is shown over a broad range of Froude numbers.

For solution B, the lowest Froude number successfully run was $F_H = 2.3$. In this case, the waves became very steep and the DELTA solution broke down due to instabilities near the wave crest. The result was only attainable with artificial

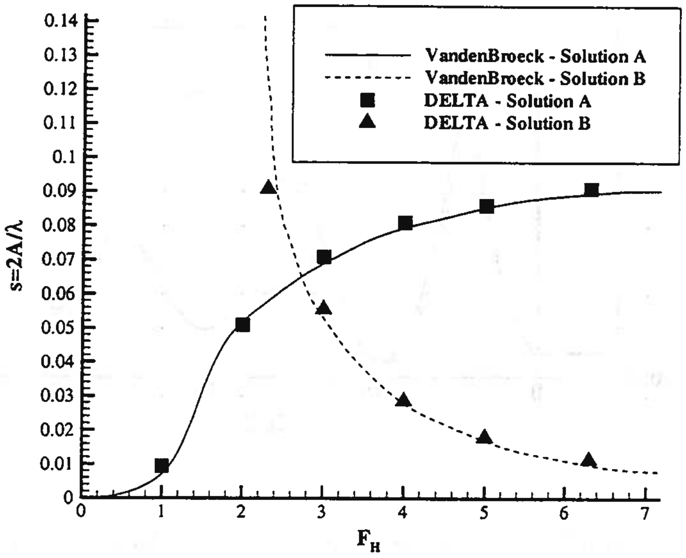

Figure 6.5: Wave steepness versus Froude number.

damping applied to the free surface. The damping is applied by adding a term in the dynamic free surface boundary condition proportional to $\frac{\partial\phi}{\partial n}^3$. Figure 6.6 shows the solution B wave train for the $F_H = 2.3$ case with and without damping. The damping successfully suppressed the breaking wave and allowed the computation to continue to steady state. The free surface damping is probably the reason the wave steepness for this case is below the theoretical value shown in figure 6.5.

6.3 Conclusions

For two-dimensional transom stern flow, the transition from transom wetted to transom dry at high Froude number is accomplished in the inviscid flow model by modifying the transom boundary condition. Perhaps a more appropriate transom boundary condition could be contrived which allows solution A for low Froude numbers and transitions appropriately to solution B as the Froude number increases through the critical value ($F_H = 2.26$). Presumably this technique may be applied to

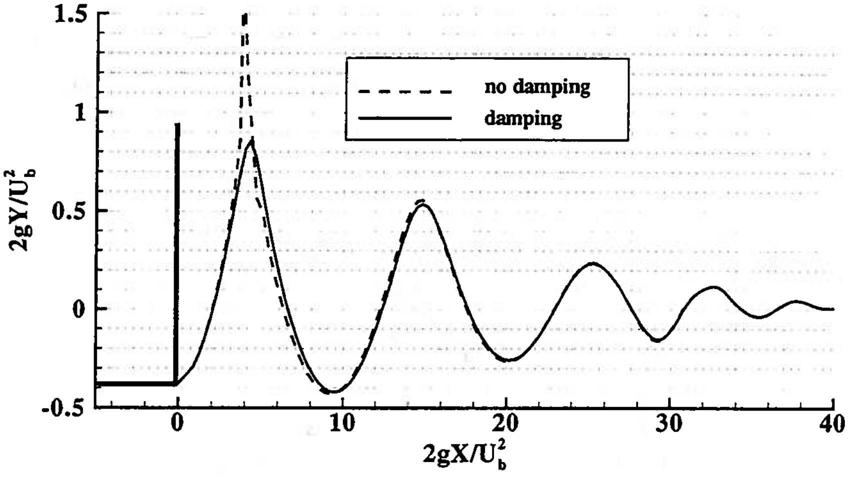

Figure 6.6: Solution B flow with and without free surface damping ($F_H = 2.3$).

the unsteady three-dimensional problem. Of course flow behind a three-dimensional transom is more complex and requires further study.

CHAPTER VII

CONCLUSIONS AND RECOMMENDATIONS FOR FURTHER RESEARCH

7.1 Conclusions

The multipole accelerated DELTA method has been applied to several body-wave interaction problems. Multipole acceleration reduces the work and storage requirements from $O(N^2)$ to $O(N)$. This significant reduction allows the analysis of large problems ($N \approx 10^4$) to be analyzed on high end workstations rather than supercomputers. The efficiency of the solution method has been increased yet further with the incorporation of a matrix preconditioner which improves the convergence of the iterative solver. The resulting method provides an analysis tool, which includes the fully nonlinear free surface hydrodynamics, to those without access to high powered computational resources. Even with the improvements in computational efficiency, the DELTA method is still a long way from maturity. The example body-wave interaction problems studied herein illustrate some important issues relative to the mathematical model and it's numerical implementation. Some of these issues have been addressed here, others require further research.

The zero speed problem of incident waves diffracted by a vertical cylinder was studied in chapter IV. Results indicate fair agreement with experiments and other computations. The problem presents some important physical and numerical issues. Since this is a zero speed problem, the application of boundary conditions on the far-field truncation boundaries is key to the success of long-time simulations. For the computations herein, the truncation boundaries were modeled as vertical walls so that all wave energy was reflected back into the basin. These boundary conditions are not satisfying because they limit the temporal length of the simulation. Approximate radiation boundary conditions are applicable to linear free surface problems and fully nonlinear problems where some information is known about the outgoing waves. A satisfactory radiation boundary condition for the general fully nonlinear problem has yet to be found.

Numerical experiments on the Wigley hull form were reported in chapter V. The standard Wigley hull was run through calm water for various Froude numbers. The wave resistance and free surface elevations were compared with experiments showing excellent agreement over the range of Froude numbers. The modified Wigley hull III was run through head seas and exciting forces were compared to experiments showing reasonable agreement for the one encounter frequency studied. Numerical treatment of the bow and stern stagnation points and a method to introduce fully nonlinear incident waves in a forward speed problem was proposed. Both resolutions produced satisfactory results. In the head seas problem, a spray jet formed near the bow for the strongly nonlinear incident waves case causing the simulation to breakdown. This is another numerical issue requiring resolution. Beck *et al.* [3] proposed a spray absorbing zone to suppress a spray jet near a two-dimensional wedge. A method for three-dimensional problems is under development.

Two-dimensional inviscid transom stern flow was studied in chapter VI. Results were compared with computations in Vanden-Broeck [43] showing excellent agreement for the comparison of wave steepness versus Froude number. An unexplained difference in wavelength between the DELTA method and Vanden-Broeck's results was observed for the downstream waves. In the inviscid solution starting from rest, the free surface always tended to rise up the stern to the stagnation height implying that flow separating from the bottom of the transom, as commonly observed behind real ships, is impossible to obtain using this inviscid solution method. The separated flow case was obtained by artificially modifying the transom boundary condition to force the free surface down to the bottom of the transom. Once separation occurred at the bottom of the transom, the flow configuration remained stable. For low Froude numbers, the downstream waves for the separated flow case became increasingly steep and computations eventually broke down at Froude number based on transom depth of $F_H = 2.3$ due to wave breaking. The wave breaking was suppressed by including a dissipative term in the free surface boundary conditions.

7.2 Recommendations for Further Research

Massively parallel computer architectures hold enormous potential for speeding up numerical computations of all kinds. The multipole accelerated DELTA method is particularly amenable to parallel implementation. Unfortunately, the implementation on a massively parallel platform would require extensive modification to the existing code in terms of incorporating message passing subroutines, unrolling loops, etc. Producing a code with a solution time which scales with the number of parallel CPUs is no trivial task at this time. Presumably, as parallel algorithms increase in sophistication, the implementation will become much simpler.

Thus far, only simple, mathematical bodies have been analyzed. A robust and efficient geometry processing package is required to study arbitrary body geometry. There are many methods for modeling body geometry. These need to be studied in order to find methods which can model the geometry with acceptable levels of accuracy and efficiency.

There are shortcomings of the inviscid model that leave important hydrodynamic issues unresolved. The physics of spray and breaking waves are included in the model up to the occurrence of the event. The accurate simulation of the event itself and the aftermath is impossible due to the presence of processes such as turbulence and air entrainment. There are simplified models for "steady" spray events. The possibility of coupling one of these models with the fully nonlinear simulation should be investigated. Breaking waves may be suppressed by artificially taking energy out of the fluid near a steep wave crest. This is accomplished by applying a local pressure patch on the free surface. Special attention is required to maintain free surface stability and the quality of the post breaking wave must be verified through physical experiments. The lack of appropriate radiation conditions at the truncation boundary can impose serious limitations on the application of this model, especially for zero speed problems. Several radiation boundary conditions have been proposed, such as absorbing beaches and matching to linear far-field waves. These methods work well for some specific problems but not necessarily for the general nonlinear problem. More research is needed in this area.

The six degree of freedom body motion integrator needs to be incorporated into the simulations. Thus far, only prescribed body motions have been investigated in three dimensions. The incorporation of body motions is a straightforward task. The only major issue is the computation of $\frac{\delta\phi}{\delta t}$ on the body. Beck et al. [3] proposed solving a boundary value problem for $\frac{\delta\phi}{\delta t}$ having the same kernel as the boundary value problem for ϕ. The solution of an additional boundary value problem at each time step may be acceptable using the $O(N)$ multipole accelerated solver.

Overall, the DELTA method produces adequate results for the two- and three-dimensional problems studied here. Improvements in the efficiency of the solution method, along with advances in computing technology, have allowed implementation on high end workstations. The previously mentioned issues require resolution before this method can become a useful tool for the prediction extreme motions and loads.

APPENDICES

APPENDIX A

MULTIPOLE AND LOCAL EXPANSION SHIFTING AND CONVERSION THEOREMS

The following are the shifting and translation theorems for multipole and local expansions. Proofs can be found in Greengard [17].

Multipole expansion shift

Consider a multipole expansion whose center is at (ρ, α, β), has coefficients O_n^m and is convergent outside the sphere of radius, a. The coefficients N_j^k of a shifted multipole expansion centered at the origin are given by,

$$N_j^k = \sum_{n=0}^{j} \sum_{m=-n}^{n} \frac{\sqrt{(j+k)!(j-k)!}\, i^{|k|-|m|-|k-m|} Y_n^{-m}(\alpha, \beta) O_{j-n}^{k-m} \rho^n}{\sqrt{(j-n+k-m)!(j-n-k+m)!(n+m)!(n-m)!}} \tag{A.1}$$

The truncation error bound for the shifted expansion is,

$$\left| \phi(P) - \sum_{j=0}^{p} \sum_{k=-j}^{n} \frac{N_j^k}{r^{j+1}} \cdot Y_j^k(\theta, \phi) \right| \leq \frac{\sum_{i=1}^{l} |\sigma_i|}{r-(a+\rho)} \left(\frac{a+\rho}{r} \right)^{p+1} \tag{A.2}$$

The evaluation of the potential using the shifted expansion is now convergent outside the sphere with radius, $a + \rho$.

Multipole to local expansion conversion

Consider a multipole expansion whose center is at (ρ, α, β), has coefficients O_n^m

and is convergent outside the sphere of radius, a. The multipole expansion can be converted to a local expansion about the origin with coefficients N_j^k,

$$N_j^k = \sum_{n=0}^{\infty} \sum_{m=-n}^{n} \frac{\sqrt{(j+n+m-k)!(j+n-m+k)!}\, i^{|k-m|} Y_{j+n}^{m-k}(\alpha,\beta) O_n^m}{\sqrt{(n+m)!(n-m)!(j+k)!(j-k)!}\,(-1)^n i^{|k|+|m|} \rho^{j+n+1}} \tag{A.3}$$

The truncation error bound for the local expansion is,

$$\left| \phi(P) - \sum_{j=0}^{p} \sum_{k=-j}^{j} r^j N_j^k Y_j^k(\theta,\phi) \right| \leq \frac{\sum_{i=1}^{l} |\sigma_i|}{ca-a} \left(\frac{1}{c}\right)^{p+1} \tag{A.4}$$

The local expansion converges inside a sphere of radius, a, separated a distance, c, from the center of the multipole expansion.

Local expansion shift

Consider a local expansion whose center is at (ρ,α,β) and has coefficients O_n^m. The coefficients N_j^k of a shifted local expansion centered at the origin are given by,

$$N_j^k = \sum_{n=j}^{\infty} \sum_{m=-n}^{n} \frac{\sqrt{(n+m)!(n-m)!}\, i^{|m|-|k|-|m-k|} Y_{n-j}^{m-k}(\alpha,\beta) O_n^m \rho^{n-j}}{\sqrt{(n-j+m-k)!(n-j-m+k)!(j+k)!(j-k)!}\,(-1)^{n-j}} \tag{A.5}$$

The translation is exact and no error bound is required.

BIBLIOGRAPHY

BIBLIOGRAPHY

[1] G.R. Baker, D.I. Meiron, and S.A. Orszag. Generalized vortex methods for free surface flow problems. *Journal of Fluid Mechanics*, 123:477–501, 1982.

[2] R.F. Beck, Y. Cao, and T.-H. Lee. Fully nonlinear water wave computations using the desingularized method. In *Proceedings* 6th *International Conference on Naval Hydrodynamics*, University of Iowa, 1993.

[3] R.F. Beck, Y. Cao, S.M. Scorpio, and W.W. Schultz. Nonlinear ship motion computations using the desingularized method. In 20th *Symposium on Naval Hydrodynamics*, Santa Barbara, California, 1994.

[4] R.F. Beck and A.R. Magee. Time-domain analysis for predicting ship motions. In *Proceedings of the Symposium on the Dynamics of Marine Vehicles and Structures in Waves*, pages 49–65, Brunel University, Elsevier Publishers, Amsterdam, The Netherlands, 1990.

[5] R.F. Beck and S.M. Scorpio. A desingularized boundary integral method for fully nonlinear water wave problems. In 12th *Australasian Fluid Mechanics Conference*, Sydney, Australia, 1995.

[6] V. Bertram. Ship motions by rankine source method. *Ship Technology Research*, 37(4):143–152, 1990.

[7] Korvin-Kroukovsky B.V. Investigation of ship motions in regular waves. In *Transactions of the Society of Naval Architects and Marine Engineers*, pages 386–435, 1955.

[8] Y. Cao. *Computations of nonlinear gravity waves by a desingularized boundary integral method.* PhD thesis, Department of Naval Architecture and Marine Engineering, The University of Michigan, Ann Arbor, Michigan, 1991.

[9] Y. Cao, T. Lee, and R.F. Beck. Computation of nonlinear waves generated by floating bodies. In 7th *International Workshop on Water Waves and Floating Bodies*, pages 47–52, Val de Reuil, France, 1992.

[10] Y. Cao, W.W. Schultz, and R.F. Beck. Three-dimensional, unsteady computations of nonlinear waves caused by underwater disturbances. In 18th *Symposium on Naval Hydrodynamics*, pages 417–427, Ann Arbor, Michigan, 1990.

[11] Y. Cao, W.W. Schultz, and R.F. Beck. A three-dimensional desingularized boundary integral method for potential problems. *International Journal of Numerical Methods in Fluids*, 11:785–803, 1991.

[12] S.K. Chakrabarti. Second order wave forces on large vertical cylinders. *Journal of the Waterways, Harbors and Coastal Engineering Division*, 101:311–317, 1975.

[13] R. Cointe. Nonlinear simulations of transient free surface flows. In *Proceedings 5th International Symposium on Numerical Ship Hydrodynamics*, 1989.

[14] R. Cointe, P. Geyer, B. King, B. Motin, and M. Tramoni. Nonlinear and linear motions of a rectangular barge in a perfect fluid. In *Proceedings of the 18th Symposium on Naval Hydrodynamics*, pages 85–99, Ann Arbor, Michigan, 1990.

[15] D.G. Dommermuth and D.K.P. Yue. Numerical simulations of nonlinear axisymmetric flows with a free surface. *Journal Fluid Mechanics*, 178:195–219, 1987.

[16] O.M. Faltinsen. Numerical solution of transient nonlinear free-surface motion outside or inside moving bodies. In *Proceedings 2nd International Symposium on Numerical Ship Hydrodynamics*, pages 347–357, Berkely, California, 1977.

[17] L.F. Greengard. *The rapid evaluation of potential fields in particle systems.* The MIT Press, Cambridge, Massachusetts, 1987.

[18] M.A. Grosenbaugh and R.W. Yeung. Nonlinear bow flows – an experimental and theoretical investigation. In *Proceedings of the 17th Symposium on Naval Hydrodynamics*, pages 195–214, The Hague, The Netherlands, 1988.

[19] R.B. Inglis and W.G. Price. A three-dimensional ship motion theory – comparison between theoretical prediction and experimental data of the hydrodynamic coefficients with forward speed. *Transaction of the Royal Insitute of Naval Architects*, 124:141–157, 1981.

[20] Gerritsma J. and Beukelman W. Analysis of the modified strip theory for the calculation of ship motions and wave bending moments. *International Ship Building Progress*, 14(156), 1967.

[21] J.M. Journée. Experiments and calculations on four wigley hull forms. Technical Report 909, Delft University of Technology, Ship Hydromechanics Laboratory, Delft, The Netherlands, 1992.

[22] C.-G. Kang and I.Y. Gong. A numerical solution method for three-dimensional nonlinear free surface problems. In *Proceedings of the 18th Symposium on Naval Hydrodynamics*, pages 427–438, Ann Arbor, Michigan, 1990.

[23] B.K. King, R.F. Beck, and A.R. Magee. Seakeeping calculations with forward speed using time-domain analysis. In *Proceedings of the* 17^{th} *Symposium on Naval Hydrodynamics*, The Hague, The Netherlands, 1988.

[24] F.T. Korsmeyer, C.-H. Lee, J.N. Newman, and Sclavounos P.D. The analysis of wave effects on tension leg platforms. In *Proceedings of the Conference on Offshore Mechanics and Arctic Engineering*, pages 1–20, Houston, Texas, 1988.

[25] F.T. Korsmeyer, D.K.P. Yue, K. Nabors, and J. White. Multipole-accelerated preconditioned iterative methods for three-dimensional potential problems. In *Proceedings of BEM*, volume 15, pages 517–527, Worcester, Massachusetts, 1993.

[26] D. Kring and P.D. Sclavounos. A new method for analyzing the seakeeping of multi-hull ships. In *Proceedings of the* 1^{st} *International Conference on Fast Sea Transportation*, pages 429–444, Trondheim, Norway, 1991.

[27] T.-H. Lee. *Nonlinear radiation problems for a surface-piercing body.* PhD thesis, Department of Naval Architecture and Marine Engineering, The University of Michigan, Ann Arbor, Michigan, 1992.

[28] W.M. Lin, J.N. Newman, and D.K.P. Yue. Nonlinear forced motions of floating bodies. In *Proceedings of the* 15^{th} *Symposium on Naval Hydrodynamics*, pages 33–49, Hamburg, Germany, 1984.

[29] M.S. Longuet-Higgins and C.D. Cokelet. The deformation of steep surface waves on water: I. a numerical method of computation. In *Proceedings of the Royal Society of London*, volume A350, pages 1–26, 1976.

[30] J.H. Michell. The wave resistance of a ship. *Philosophical Magazine*, 1898.

[31] K.S. Nabors, F.T. Korsmeyer, F.T. Leighton, and J. White. Preconditioned, adaptive, multipole-accelerated iterative methods for three-dimensional first-kind integral equations of potential theory. *SIAM Journal of Scientific Computation*, 15(3):713–735, 1994.

[32] D. Nakos, A. Nestegård, T. Ulstein, and P.D. Sclavounos. Seakeeping analysis of surface effect ships. In *Proceedings of the* 1^{st} *International Conference on Fast Sea Transportation*, pages 413–428, Trondheim, Norway, 1991.

[33] D. Nakos and P.D. Sclavounos. Ship motions by a three-dimensional rankine panel method. In *Proceedings of the* 18^{th} *Symposium on Naval Hydrodynamics*, pages 21–41, Ann Arbor, Michigan, 1990.

[34] A. Nestegård. Comparative study of fully non-linear wave simulation programs. Technical Report 94-2401, Det Norske Veritas, Høvik, Norway, December 1994.

[35] J.N. Newman. Transient axisymmetric motion of a floating cylinder. *Journal of Fluid Mechanics*, 157:17–33, 1985.

[36] F. Noblesse and J.H. McCarthy. Ship wave-resistance computations. In *Proceedings of the* 2^{nd} *DTNSRDC Workshop*, 1983.

[37] T.F. Ogilvie and E.O. Tuck. A rational strip theory for ship motions. Technical Report 013, Department of Naval Architecture and Marine Engineering, University of Michigan, Ann Arbor, Michigan, 1969.

[38] J.-H. Park and Troesch A.W. Numerical modeling of short-time scale nonlinear water waves generated by large vertical motions of non-wallsided bodies. In *Proceedings of the* 19^{th} *Symposium on Naval Hydrodynamics*, page in press, Seoul, Korea, 1992.

[39] Y. Saad and H. Schultz. Gmres: A generalized minimal residual algorithm for solving nonsymmetric linear systems. *SIAM Journal of Scientific Computation*, 7(3):856–869, 1986.

[40] N. Salvesen, Tuck E.O., and Faltinsen O. Ship motions and sea loads. In *Transactions of the Society of Naval Architects and Marine Engineers*, 1970.

[41] S.M. Scorpio and R.F. Beck. A multipole accelerated desingularized method for computing nonlinear wave forces on bodies. In *Proceedings of the* 15^{th} *International Conference on Offshore Mechanics and Arctic Engineering*, Florence, Italy, 1996.

[42] S.M. Scorpio, R.F. Beck, and F.T. Korsmeyer. Nonlinear water wave computations using a multipole accelerated, desingularized method. In *Proceedings of the* 21^{st} *Symposium on Naval Hydrodynamics*, Trondheim, Norway, 1996.

[43] J.-M. Vanden-Broeck. Nonlinear stern waves. *Journal of Fluid Mechanics*, 96:603–611, 1980.

[44] J.-M. Vanden-Broeck and E.O. Tuck. Computation of near-bow or stern flows, using a series expansion in the froude number. In *Proceedings of the* 2^{nd} *International Conference on Numerical Ship Hydrodynamics*, pages 371–381, Berkely, California, 1977.

[45] T. Vinje and P. Brevig. Nonlinear ship motions. In *Proceedings* 3^{rd} *International Symposium on Numerical Ship Hydrodynamics*, pages 257–268, Paris, France, 1981.

[46] W.C. Webster. The flow about arbitrary, three-dimensional smooth bodies. *Journal of Ship Research*, 19:206–218, 1975.

[47] G.X. Wu and R.A. Eatock Taylor. A green's function form for ship motions at forward speed. *International Shipbuilding Progress*, 34:189–196, 1987.

[48] C. Yang and R.C. Ertekin. Numerical simulation of nonlinear wave diffraction by a vertical cylinder. *Journal of Offshore Mechanics and Arctic Engineering*, 114:36–44, 1992.

[49] Z. Zhou and M. Gu. A numerical research of nonlinear body-wave interactions. In *Proceedings of the* 18^{th} *Symposium on Naval Hydrodynamics*, pages 103–118, Ann Arbor, Michigan, 1990.